THERMOMECHANICAL ANALYSIS OF A DAMAGED THERMAL PROTECTION SYSTEM

by

Wei Heok Ng

A dissertation submitted in partial fulfillment
of the requirements for the degree of
Doctor of Philosophy
(Aerospace Engineering)
in The University of Michigan
2007

Doctoral Committee:

Professor Peretz P. Friedmann, Co-Chair
Professor Anthony M. Waas, Co-Chair
Associate Professor Carlos E. Cesnik
Associate Professor Bogdan I. Epureanu

For my family

ACKNOWLEDGEMENTS

Completing a doctoral dissertation is an arduous endeavor; one that cannot be achieved without the help of many people. I have been very fortunate to be able to work with numerous brilliant and capable individuals who have enriched my life greatly. For that, I am extremely grateful.

I would like to thank my advisors, Professors Peretz Friedmann and Anthony Waas, for their mentorship during my years as a graduate student. Completion of this dissertation would not have been possible without their guidance, insights and patience. I would also like to thank Professors Carlos Cesnik and Bogdan Epureanu for taking their time to serve as members of the dissertation committee.

The work that this dissertation is based on was supported by the Space Vehicle Technology Institute under grant NCC-989, jointly funded by NASA and DOD within the NASA Constellation University Institutes Project, with Claudia Meyer as the project manager. Assistance has also been provided by various members of NASA. Thanks to Joseph Sikora, Kamran Daryabeigi and Scott Splinter of Langley Research Center for providing their expertise on the development of the High Temperature Structures Laboratory, as well as Mark Dub, Sandra Tetley, Cooper Snap, and Stan Bouslog of Johnson Space Center for their help in securing materials for the experiments conducted.

I would like to extend my gratitude to Andrew Caird, Matthew Britt and Brock Palen of the Center for Advanced Computing at the University of Michigan for providing support on Nyx, the computing cluster system on which most of the numerical analysis were run. I am also very thankful for the assistance provided by Jack McNamara, a fellow student, in the CFD portion of the dissertation.

The assistance provided by machinist Terry Larrow and technicians Dave McLean, Tom Griffin, and Eric Kirk in setting up the laboratory as well as the experiments are greatly appreciated. I would also like to thank the logistic staff, Debbie Laird, Suzanne Smith, Sharon Bauerle, Denise Phelps, Cindy Collins, Cindy Enoch and Margaret Fillion.

The ever-friendly custodians, Diana and Jenna McVey, have constantly reminded me about the dangers of "all work and no play". While I am appreciative of their concern, I was never in any danger thanks to a, surprisingly, not-so-small group of people: fellow students Amit Salvi, Shu-Ching Quek, Yerramilli Chandrasekher (Chandu), Shiladitya Basu, De Xie, Shun-Jun Song, Joseph Rakow, Pete Gufstafson, Jack McNamara, Li Liu, Brian Glaz, Abhijit Gogulapati, Dan Patt and Ken Salas, and friends in Michigan, German Lorenzo, Eric Emanuel and Scott Spector, as well as in Chicago, Bryan Walker and Mike Demetria.

I would also like to extend my gratitude to Aikira sensei, Karen sensei, Pek sensei, Eric Schlichting, Kathie Wolney, and other members of the University of Michigan Aikido club and Genyokan, for providing me the opportunity to practice and train in the art of Aikido, of which the benefits are immeasurable.

Last, but definitely not the least, to my family and loved ones, without whom, none of this would have any meaning: Thank You!

TABLE OF CONTENTS

DEDICATION . . . . . **ii**

ACKNOWLEDGEMENTS . . . . . **iii**

LIST OF FIGURES . . . . . **viii**

LIST OF TABLES . . . . . **xii**

LIST OF SYMBOLS . . . . . **xv**

CHAPTER

I. INTRODUCTION, BACKGROUND AND OBJECTIVES 1

1.1 Thermal Protection Systems 2
1.1.1 NASA Space Shuttle Thermal Protection System 3
1.1.2 Other Thermal Protection Systems 8
1.2 Literature Review 8
1.3 Objectives of the Dissertation 10
1.4 Principal Contributions of the Dissertation 12
1.5 Outline of Dissertation 12

II. DAMAGE MODELING AND AXISYMMETRIC FINITE ELEMENT MODEL 21

2.1 TPS Damaged Model and Finite Element Mesh 22
2.2 Finite Element Analysis 24
2.2.1 Heat Transfer Analysis 24
2.2.2 Thermal Stress Analysis 26
2.2.3 Material Properties and Simplifying Assumptions 26

2.3 Results and Discussion 27
2.3.1 Axisymmetric Finite Element Results 27

III. THREE DIMENSIONAL FINITE ELEMENT MODEL 49

3.1 Finite Element Analysis and Meshing Considerations 50
3.2 Simplifying Assumptions 50
3.3 Results and Discussion 51
3.3.1 Results for 3D Model Using Assumptions From Previous Chapter 52
3.3.2 Validity of Assumptions Used in The Previous Chapter . . 56
3.3.3 Thermomechanical Behavior with Improved Assumptions Based on the 3D Model and Comparison with Previous Results 63
3.3.4 Effects of Damage Location 65

IV. DEVELOPMENT OF A THERMAL STRUCTURES TEST FACILITY AND ITS CALIBRATION 93

4.1 Design Requirements 93
4.2 Test Facility 94
4.3 Calibration Tests 95
4.4 Calibration Results 96

V. EXPERIMENTS ON UNDAMAGED AND DAMAGED SHUTTLE TILES AND CORRELATION WITH THE FINITE ELEMENT MODEL 104

5.1 Description of Experiments 104
5.1.1 Test Specimen and Load Fixture 105
5.1.2 Instrumentation 105
5.1.3 Specimen Assembly 106
5.1.4 Pressure and Temperature Profiles 106
5.2 Finite Element Model 107
5.3 Experimental Results 108
5.4 Validation of Finite Element Model 109

VI. THERMOMECHANICAL BEHAVIOR OF DAMAGED TPS SUBJECTED TO FLOW-DEPENDENT HEAT LOAD 124

6.1 Flow Dependent Thermal Loads 124
6.1.1 Hypersonic Cavity Flow 125
6.1.2 Thermal Loads from CFL3D 126
6.1.3 Thermal Loads from Published Data 127
6.1.4 Applied Thermal Loads for Finite Element Analysis 128
6.2 Finite Element Mesh and Method 129
6.3 Results and Discussion 131

VII. CONCLUSIONS AND RECOMMENDATIONS FOR FUTURE RESEARCH 148

7.1 Conclusions 149
7.2 Recommendations for Future Research 150

APPENDIX **152**

BIBLIOGRAPHY **157**

LIST OF FIGURES

Figure

1.1 Flight envelopes for hypersonic vehicles 14

1.2 Temperatures and exposure times for hypersonic vehicles(Ref. 48, Pg. 19) 15

1.3 Approximate maximum re-entry temperatures on outer surface of Space Shuttle Orbiter (Ref. 5, Pg. W-98) 16

1.4 Locations of various TPS 17

1.5 Initial materials used for Space Shuttle TPS) 18

1.6 Space Shuttle HRSI Tile and Airframe (Ref. 5, Pg. W-102) 19

1.7 Advanced Flexible Reusable Surface Insulation 20

2.1 Schematic view of square segment of the three-layered TPS configuration 37

2.2 Approximate circular axisymmetric configuration 38

2.3 Damage geometry associated with hypervelocity impact 39

2.4 FE meshes of axisymmetric model illustrating damage geometry and coordinate system 40

2.5 Boundary layer region for axisymmetric model 41

2.6 8-node biquadratic elements used for axisymmetric model 42

2.7 Re-entry heat flux loading profile for the ATS vehicle 43

2.8 Cross section of TPS showing the undamaged and damaged surfaces subjected to thermal loading 44

2.9 Schematic representation of radiation heat loss in the tile 45

2.10 Structural boundary conditions applied to underlying structure 46

2.11 Temperature contour plots for the undamaged and D = 1″ damaged axisymmetric models for the two different heat loads at times when the maximum von Mises stress in tile occurs. Legend indicates temperatures in °C 47

2.12 von Mises stress contour plots for the undamaged and D = 1″ damaged axisymmetric models for the two different heat loads at times when the maximum von Mises stress in tile occurs. Legends indicate stresses in Pascal 48

3.1 Schematic of 3D model illustrating the change in location of damage from center 79

3.2 Illustration the boundary layer region in 3D model 80

3.3 FE meshes for 3D models with $D = 1$" damage 81

3.4 10-node quadratic tetrahedron element used for 3D model 82

3.5 Structural boundary conditions applied to underlying structure 83

3.6 Temperature contour plots for the undamaged and damaged (D = 1″) 3D models for the two different heat loads at times when the maximum von Mises stress in tile occurs. Legends indicate temperatures in °C 84

3.7 von Mises stress contour plots for the undamaged and D = 1″ damaged 3D models for the two different heat loads at times when the maximum von Mises stress in tile occurs. Legends indicate stresses in Pascal 85

3.8 Comparison of maximum temperatures for axisymmetric and 3D models 86

3.9 Comparison of maximum von Mises stresses in the tile for axisymmetric and 3D models 87

3.10 Comparison of maximum von Mises stresses in the SIP for axisymmetric and 3D models 88

3.11 Comparison of maximum von Mises stresses in underlying structure for axisymmetric and 3D models 89

3.12 ATS vehicle operating pressure profile 90

3.13 Transient temperature results at the surface and middle of the tile and at underlying structure for analyses with and without pressure dependent conductivity 91

3.14 Previous and new values of CTE with respect to temperature 92

4.1 Re-entry temperature and pressure profiles of ATS vehicle 98

4.2 Overview of High Temperature Thermal Structures Testing Laboratory . . 99

4.3 Location of thermocouples on calibration specimen 100

4.4 Calibration test setup 101

4.5 Comparison of target and measured re-entry pressure 102

4.6 Comparison of target and measured surface temperature 103

5.1 TPS specimen and load fixture 113

5.2 Location of thermocouples and strain gages on instrumented specimen . . 114

5.3 Illustration and photographs of test setup 115

5.4 FE meshes for correlation studies 116

5.5 Unrestrained boundary condition applied to underlying structure 117

5.6 Comparison of temperatures obtained in experiment on surface and in damaged region of specimen 118

5.7 Comparison of temperatures at base of damaged region for various damage size 119

5.8 Comparison of predicted and measured temperatures 120

5.9 Comparison of predicted and measured strains 121

5.10 FEA temperature results in the SIP for $D = 1.5$" and 1.875" damaged configuration 122

5.11 Cross section of experimental specimen 123

6.1 Different types of supersonic/hypersonic cavity flows 138

6.2 Coarsened view of CFL3D computational domain for damaged tile 139

6.3 Heat load ratio along damaged surface from CFL3D analysis 140

6.4 Heat load ratio profile from Reference 34 141

6.5 Re-entry surface heat load and pressure of ATS vehicle 142

6.6 Heat load ratio profiles based on CFL3D and published data (EP) 143

6.7 FE mesh used in analysis 144

6.8 Half model of TPS showing the different sections required for application of flow dependent heat load 145

6.9 Schematic of subsections of damaged surface 146

6.10 Temperature($^\circ$C) contour plot of $D = 1.0$ configuration subjected to EP heat load when maximum temperature is reached 147

A.1 Conceptual illustration of apparent strain 155

A.2 Apparent strain results for undamaged specimen in experiments described in Chapter V 156

LIST OF TABLES

Table

2.1 Material properties of the underlying structure (Aluminum 2024) 31

2.2 Material properties of SIP 32

2.3 Material properties of LI-900 tiles 33

2.4 Maximum temperatures and times at which they occur in tile, SIP and underlying structure in axisymmetric models 34

2.5 Maximum von Mises stresses and times at which they occur in tile for the axisymmetric case at t_1 for the two different thermal loading conditions . 35

2.6 Maximum von Mises stress and times at which they occur in tile for the axisymmetric case at t_2 for the two different thermal loading conditions . 35

2.7 Maximum von Mises stress and times at which they occur in the SIP for the axisymmetric case for the two different thermal loading conditions . 36

2.8 Maximum von Mises stress and times at which they occur in underlying structure for the axisymmetric case for the two different thermal loading conditions 36

3.1 Maximum temperatures and times at which they occur in the tile, SIP and underlying structure in 3D models 67

3.2 Maximum von Mises stresses and times at which they occur in tile for the 3D models at t1 for the two different thermal loading conditions 68

3.3 Maximum von Mises stresses and times at which they occur in tile for the 3D models at t2 for the two different thermal loading conditions 68

3.4 Maximum von Mises stresses and times at which they occur in SIP for the 3D models for the two different thermal loading conditions 69

3.5 Maximum von Mises stresses and times at which they occur in underlying structure for the 3D models for the two different thermal loading conditions 69

3.6 Material properties of the underlying structure (Aluminum 2024) 70

3.7 Conductivity of SIP (W/m-°C) with respect to temperature and pressure 71

3.8 Material properties of SIP 71

3.9 Conductivity of LI-900 tile (W/m-°C) with respect to temperature and pressure 72

3.10 Material properties of LI-900 tile 72

3.11 Emissivity (ε) of uncoated tile with respect to temperature 73

3.12 Maximum temperature results for $D = 1$" axisymmetric model for analysis with or without temperature dependent emissivity 74

3.13 Maximum von Mises stresses attained for each TPS component with or without pressure dependency in conductivity 74

3.14 Maximum von Mises stresses attained for analysis using isotropic or transversely isotropic material properties 75

3.15 Maximum von Mises stresses attained for each TPS component with constant or temperature-dependent material properties 75

3.16 Maximum temperature results for 3D models using improved assumptions 76

3.17 Maximum von Mises stresses and times at which they occur in tile for the 3D models using improved assumptions 77

3.18 Maximum von Mises stresses and times at which they occur in SIP for the 3D models using improved assumptions 77

3.19 Maximum von Mises stresses and times at which they occur in underlying structure for the 3D models using improved assumptions 77

3.20 Maximum temperatures attained for each TPS component for different δ with q_2 thermal loading 78

3.21 Maximum vom Mises stresses attained for each TPS component for BC1 and BC2 boundary conditions 78

5.1 Material properties for Cerachem blankets 112

6.1 Maximum temperature results for all TPS components subjected to flow dependent heat loads 135

6.2 Maximum temperature results for all TPS components subjected to flow dependent heat loads 136

6.3 Maximum von Mises stress results for all TPS components subjected to flow dependent heat loads 137

LIST OF SYMBOLS

Symbols	Description
A_i	Coefficients of bilinear function $F(y, z)$
c	Specific heat
D	Depth and diameter of damage in TPS
E_T	Difference in maximum temperatures between axisymmetric and 3D FE models
E_σ	Difference in maximum von Mises stresses between axisymmetric and 3D FE models
E	Young's modulus
$F(y, z)$	Bilinear function for varying heat load within damage
G_i, H_i	Data points of temperature or pressure profiles
k	Thermal conductivity
M	Mach number
n	Number of data points for calculating average difference
P	Pressure
q_{ATS}	Thermal load profile of the ATS vehicle
q/q_0	Heat load ratio of applied thermal loads
q_1, q_2	Thermal load boundary conditions
r, z	Spatial coordinates for axisymmetric FE model
Re	Reynold's number
S_d	Damaged region on tile top surface
S_u	Undamaged region on tile top surface
t_1, t_2	Instances when high von Mises stresses are observed in tile
T	Temperature
T_{axi}, T_{3D}	Maximum temperatures for axisymmetric and 3D FE models
T_0	Stagnation temperature
u_i	Displacement in the i-direction
X	Distance along base of cavity for References 12 and 34
X_s	Distance along centerline of damage from upstream-facing lip of damage
x, y, z	Spatial coordinates for 3D FE model

α	Coefficient of thermal expansion (CTE)
δ	Offset distance of damage from center
ε	Thermal emissivity
ν	Poisson's ratio
ρ	Density
$\sigma_{axi}, \sigma_{3D}$	Maximum von Mises stresses for axisymmetric and 3D FE models
$\sigma_{Eaxi}, \sigma_{E_{3D}}$	von Mises stresses for axisymmetric and 3D FE models
σ_{ij}	Components of stress tensor

Acronyms	Description
AFRSI	Advanced Flexible Reusable Surface Insulation
ARMOR	Adaptable, Robust, Metallic, Operable, Reusable
ATS	Access to Space
CFD	Computational Fluid Dynamics
CTE	Coefficient of Thermal Expansion
FE	Finite Element
FRCI	Fibrous Refractory Composite Insulation
FRSI	Flexible Reusable Surface Insulation
HRSI	High-Temperature Reusable Surface Insulation
LRSI	Low-Temperatures Reusable Surface Insulation
RCC	Reinforced Carbon-Carbon
RLV	Reusable Launch Vehicle
RSI	Reusable Surface Insulation
RTV	Room Temperatures Vulcanizing
SIP	Strain Isolator Pad
TPS	Thermal Protection System
TUFI	Toughened Unipiece Fibrous Insulation

CHAPTER I

INTRODUCTION, BACKGROUND AND OBJECTIVES

The development of thermal protection systems (TPS) for winged flight vehicles originated with the breaking of the sound barrier in 1947 by the Bell X-1 vehicle [14]. Since then, research in hypersonic vehicles has progressed at a rapid pace, from the X-2 supersonic research aircraft flying at a maximum speed of Mach 3.2, to the Apollo capsule at Mach 36, and the Space Shuttle at Mach 27. During this time, it became evident that TPS is a critical component of any hypersonic vehicle and it is often one of the limiting technologies in hypersonic vehicles design.

Severe aerodynamic heating during high-speed flight induces elevated temperatures in the vehicle that adversely affect the structural components by degrading the material properties. This also induces time-dependent changes in material properties, including potentially complex effects such as creep and chemical reactions. The increase in temperatures also induces thermal stresses and strains, which influences the buckling and aerothermoelastic behaviors. Thus, it is critical to maintain the temperatures of the load-bearing structural components of hypersonic vehicles within operational limits to avoid catastrophic failure – this is role of TPS.

1.1 Thermal Protection Systems

The primary function of the TPS is to protect the vehicle and its payload by keeping the temperatures to within acceptable limits. Three TPS concepts have been successfully employed on several hypersonic vehicles:

1. Heat sink/Hot structures: structural components made with high temperature materials with high emissivity surface coating for heat rejection.

2. Ablation: ablative heat shields made with a resinous composite materials that slowly vaporizef during descent, allowing the heat to dissipate along with the ashes.

3. Insulated structures: structural components made from conventional materials (e.g. aluminum) and insulated from aerodynamic heating by a layer of non-load bearing insulation materials.

The choice of the TPS concept used depends on the flight envelope of the hypersonic vehicle, shown in Figure 1.1, which determines the flight duration and maximum temperatures imposed on the vehicle, shown in Figure 1.2. There are many factors involved in selecting materials for a TPS. While strength and stability at operating temperatures are obvious factors, other requirements, like costs, weight efficiency and thermal compatibility with underlying structure, are also important concerns.

A substantial segment of current research on hypersonic vehicles is focused on reusable launch vehicles (RLV), since these have the potential to provide low-cost access to space. The Space Shuttle is the closest to a true RLV, however it has not met the goal of low cost access to space. For RLVs, the long re-entry time, combined with the requirements on reusability, maneuverability, and low weight led to the selection of insulated structures as

the most suitable TPS concept. To survive multiple launches, the TPS has to withstand not only thermal loads, but also mechanical loads as well as harsh chemical environments repeatedly without failure. These conflicting requirements result in some form of compromise, leading to the development of several different types of TPS. An overview of the structural and material technologies that are currently in use, as well as those that may be potential candidates for TPS in RLVs is presented in Reference 42. Some of the future systems include concepts using ceramics, metals, and carbon-, ceramic- and metallic-matrix composites.

1.1.1 NASA Space Shuttle Thermal Protection System

NASA's Space Shuttle is the first and only partially reusable orbital spacecraft. Capable of carrying $5 - 7$ astronauts and up to $50,000$ lbs of payload to low earth orbit, it was also designed to recover payloads from orbit back to Earth. The Space Shuttle system consists of three main components: the reusable orbiter vehicle, the expendable external tank and two partially reusable Solid Rocket Boosters. The discarded external tank and the extensive overhaul required between flights are reasons why the Shuttle is only considered to be partially reusable.

The airframe of the Space Shuttle Orbiter was built primarily from conventional aluminum alloys, so as to reduce development cost and risk. Aluminum structures have a maximum operating temperature of $175\,^{\circ}\mathrm{C}$, which is substantially below the temperatures encountered during re-entry flight. Previous re-entry vehicles were not meant to be reusable and thus employed ablative heat shields. Materials used for these heat shields are heavy; however, this was not a big disadvantage due to the relative small size of the vehicles. The Shuttle orbiter is much larger and has a substantial surface area, thus new

light-weight, high-performance TPS had to be developed.

Figure 1.3 shows the approximate re-entry surface temperature contours for the Space Shuttle Orbiter that can vary between $315\,^{\circ}\mathrm{C}$ and $1500\,^{\circ}\mathrm{C}$. The wide range of temperatures combined with the need for minimizing structural weight led to a design utilizing several materials. Initially, four materials, as shown in Figure 1.5, were used for the TPS of the orbiter:

1. Felt reusable surface insulation (FRSI)
2. High-temperature reusable surface insulation (HRSI) tiles
3. Low-temperature reusable surface insulation (LRSI) tiles
4. Reinforced carbon-carbon (RCC)

Each material has different heat protection, impact resistance and weight characteristics, and thus are used on different location on the vehicle as shown in Figure 1.4

Felt reusable surface insulation

FRSI blankets protect the orbiter against temperatures between 175 and $400\,^{\circ}\mathrm{C}$. These flexible felt blankets, shown in Figure 1.5(a), are made of a nylon material called Nomex that is coated with a waterproof silicone elastomer to achieve required thermal and optical properties. These blankets have a density of 5.4 lb/ft^3 and are bonded directly to the shuttle surface using a room-temperature vulcanizing (RTV) silicone adhesive. The blankets are manufactured in sheets of 3 to 4 square feet and in thicknesses from 0.16" to 0.40".

Reusable Surface Insulation Tiles

Two types of RSI tiles are used on orbiter's surfaces that experience temperatures between $400\,^{\circ}\mathrm{C}$ and $1260\,^{\circ}\mathrm{C}$. They are essentially made from the same base material: high purity silica fibers. These fibers are bonded together via a sintering process, which give rise to solid billets that are extremely porous, where fibers only make up about 10% by volume. This results in a material, called LI-900, with a density of only 9 lbs/ft^3, and very low thermal conductivity for thermal protection. It also has low coefficient of thermal expansion and stiffness, which minimizes thermal stresses and allows the material to resist thermal shock damage from repeated and drastic temperature changes during operation. These properties, combined with the ability to retain its shape while subjected to aerodynamic loads under high temperatures, make it an ideal TPS material for the winged Shuttle Orbiter, since it allows the aerodynamic surfaces to maintain their shape during re-entry. This component is used on up to 70% of the exterior surface of the shuttle. These desirable properties compromise the overall strength of the material. Therefore, the brittle LI-900 cannot be used around high stress areas around landing gear doors and windows. A higher strength version, the LI-2200, with density of 22 lb/ft^3, was developed for use in these areas. The high porosity of the tiles causes moisture absorption that can lead to degradation in thermal properties. This is prevented by coating the tiles with waterproof compounds that also enhance their heat rejection capabilities. The difference between HRSI and LRSI tiles, as shown in Figures 1.5(b) and 1.5(c) respectively, lies in the coating used.

The black coating on HRSI tiles is made from a mixture of powdered tetrasilicide and borosilicate glass and is often referred to as reaction-cured glass (RCG). The HRSI tiles

usually have a 6" by 6" square configuration with thicknesses that vary from 1 to 5 inches depending on the heat load encountered during re-entry. They provide protection for temperatures between 650 °C and 1260 °C.

The LRSI tiles are coated with a mixture of silica compounds combined with aluminum oxide, which give them a white appearance. This coating has high thermal reflectivity that minimizes the heat absorbed from the sun while the shuttle is in orbit. They are used in areas where temperatures vary between 400 °C and 650 °C. Due to the lower heat load in these areas, LRSI tiles are larger and thinner and usually have of 8" by 8" square configuration and their thicknesses vary between 0.2" and 1.0".

The tiles are brittle, thus they cannot be attached directly to the surface of the vehicle, because they cannot withstand the mechanical and thermal strains sustained by the underlying airframe. A strain isolator pad (SIP) is used to isolate the tiles from the strains of the underlying structure. The three layers are attached to each other using a silicone RTV adhesive. A schematic illustration of the lay-up is shown in Figure 1.6. The SIP is a felt pad of randomly oriented horizontal Nomex fibers, a family of fibers produced by DuPont. The pad has a very low modulus of elasticity which absorbs the strains of the underlying airframe and greatly reduces the strains transferred to the tiles.

Reinforced Carbon-Carbon

The RCC is a composite consisting of carbon matrix reinforced with graphite fibers. The outer layers of the RCC are converted to silicon carbide to resist oxidation. The material, as shown in Figure 1.5(d), has high strength and stiffness that are retained up to a maximum service temperature of 1650 °C. Furthermore, the RCC has good fatigue resistance and

therefore, is used in areas where the highest temperatures, aerodynamic and vibrational loads are expected to occur; typical locations include nose cap, wing leading edges and external tank attachment points.

A series of floating joints are used to mechanically attach the RCC panels to the obiter in order to minimize loading. The high conductivity of the RCC panels requires the installation of insulating blankets and HRSI tiles beneath the panels to protect the joints and underlying structure from excessive temperatures.

Other Shuttle Thermal Protection System Materials

As technology advances, new materials were developed to better serve the flight and operational requirements of the shuttle. These materials include Advanced Flexible Reusable Surface Insulation (AFRSI) blankets, Fibrous Refractory Composite Insulation (FRCI) tiles, and Toughened Unipiece Fibrous Insulation (TUFI) tiles.

AFRSI blankets, shown in Figure 1.7, were developed to replace the FRSI blankets and majority of the LRSI tile on the upper surface of the shuttle. These blankets consist of low-density fibrous silica batting material sandwiched between a layer of silica fabric on the hot side and a layer of glass fabric, stitched together to give a quilt-like appearance. These blankets have the same thermal performance as the LRSI tiles, but with better durability and lower operational costs. They are manufactured in 3 by 3 feet squares and vary in thicknesses from 0.45" to 0.95".

FRCI tiles are made the same way as LI-900 tile except that alumina-borosilicate fibers are added for higher strength and they are used to replace the LI-2200 HRSI tiles. The FRCI tiles have a much lower density at 12 lb/ft^3 and provide better strength and durability.

TUFI tiles are essentially LI-900 tile with a more durable surface coating. The coating permeates the pores near the surface of the tile, creating a strong, crack-resistant outer surface. However, this process also increases the conductivity of the tile. Thus, these tiles have only replaced the HRSI tiles in areas where higher impact resistance are required, e.g. near main engines and the upper body flap.

1.1.2 Other Thermal Protection Systems

The effectiveness of the TPS on the shuttle has been demonstrated, however, their fragility and high maintenance cost remain an important issue. This has motivated new research on TPS for vehicles, such as X-33 [26] and X-34 [24]. The new TPS envisioned for these vehicles are expected to be more robust, lightweight, and low maintenance. Some of the new TPS concepts are metallic such as titanium multiwall TPS [43], superalloy honeycomb TPS [21] and most recently the Adaptable, Robust, Metallic, Operable, Reusable (ARMOR) TPS [4].

1.2 Literature Review

The majority of studies on TPS deal with the Space Shuttle since it is the only operational reusable spacecraft. The maiden flight of the shuttle took place in April, 1981 [37]. Until then, only a limited number of studies on the structural aspects of the Space Shuttle tiles were conducted. Preflight thermal stress analysis of the Space Shuttle Orbiter TPS and skin panel was conducted using a one-dimensional temperature profile across the tile's thickness [19]. Tension, and combined tension and bending tests were conducted on the RSI tile specimen by incorporating photoelastic material to determine the nature of

stress-transfer between SIP and tile [33]. Static and fatigue strength of the TPS tile were determined using both static and cyclic load tests [41]. The dynamic response of the TPS was also investigated [17,25].

During subsequent flights, the operational performance of the Space Shuttle RSI TPS were understood and certified [10,32]. The availability of flight data allowed an improved evaluation of the analytical tools used to predict TPS thermal performance. Numerical predictions using three-dimensional finite-volume models were found to match flight data well [31,36].

Early flights exposed several shortcomings in the structural performance of the TPS. This motivated studies aimed at the verification of the structural integrity of the TPS as well as potential improvements. In these studies, fracture properties for the tiles were characterized [20], and the effect of SIP modulus on in-plane strains was determined experimentally [39]. Simulated mission load tests, consisting of a series of combined static and random dynamic loads with substructure deformations, were also conducted to determine the integrity of the TPS [7,23,27,38].

Other studies examined new metallic TPS concepts. The Multiwall TPS was studied using a combined analytical and experimental approach that include radiant-heat, wind-tunnel and lightning strike tests [43]. Numerical simulation were conducted on superalloy honeycomb TPS to determine its thermoelastic response [21]. The ARMOR TPS concept was evaluated using one-dimensional finite volume thermal analysis to determine the resultant deformations [8], followed by thermal, structural and creep FE analyses [4].

The recent Space Shuttle *Columbia* incident highlighted the vulnerability of the TPS to damage associated with impact of debris such as foam. The initial uncertainty as to which

TPS was affected and the precise nature of the damage motivated the need for research on damaged TPS. Extensive investigation has attributed the cause for the accident to a damaged RCC panel on the left wing leading edge [1]. The accident resulted in a few studies on damaged TPS, however, most of these studies only sought to either determine and characterize types of damage caused by debris impact via experiments [18] or numerical methods [11,13,46], or determine the change in aerothermal loading due to TPS defects [12,34]. Thus, there are no systematic studies on the effect of damage on the thermomechanical response of TPS, except for one study [44], where aerothermal tests on a couple of damaged TPS were conducted in a high temperature wind tunnel. This study was primarily qualitative and post-test inspection of the TPS specimens could not be performed because they were destroyed accidentally during the experiment.

1.3 Objectives of the Dissertation

From the literature review provided in the previous section, it can be seen that there have been limited published research on the thermomechanical behavior of damaged TPS. In particular, systematic studies of the effects of damage on the thermomechanical response of a TPS do not exist. With the exception of Reference 44, where surface-heating test was conducted on damaged TPS, there had been no other studies on the performance and structural response of damaged TPS.

The main objective of this research is to determine the effects of damage on the performance and structural integrity of a representative TPS. This study has both analytical as well as experimental objectives, and the Space Shuttle *Columbia* accident combined with the availability of actual test articles for the TPS that were provided by NASA, caused the

study to focus on the TPS of the Space Shuttle. The specific objectives of this dissertation are:

1. Develop two finite element (FE) models capable of analyzing the effects of damage induced by impact on the performance of the TPS, and the structural integrity of the underlying structure. The first FE model is an approximate axisymmetric model that yields a two-dimensional representation of the TPS and the underlying structure. The second FE model is a complete three-dimensional model of a rectangular tile and associated elements of the TPS. The goal of this part of the research is to determine the relative accuracy of the two models and their ability to represent the behavior of the TPS system under a set of simplifying assumptions.

2. Replace the initial set of simplifying assumptions in the FE models by a more realistic set of assumptions, and determine the role and validity of these simplifying assumptions.

3. Develop a thermal structural test facility and use it to determine the validity and accuracy of the three-dimensional FE model of undamaged and damaged TPS system under conditions that simulate re-entry.

4. Extend the three-dimensional FE analysis to include a more realistic representation of the thermal loading by considering the interaction between the damaged tile and the external high speed flow using both computational fluid dynamics (CFD) as well as some experimental data gleaned from a number of recent papers [12, 34].

1.4 Principal Contributions of the Dissertation

The research produces several new and original contributions to the analysis and testing of damaged TPS:

1. Development of two FE models, an approximate axisymmetric model and a more accurate 3D model described in the previous sections, that are capable of representing damage due to impact in a TPS.

2. A careful examination and comparison of the role of various assumptions in modeling TPS damage using FE modeling.

3. Construction of a thermal structure testing facility in the Department of Aerospace Engineering of the University of Michigan and its use in validating FE analysis of undamaged and damaged TPS.

4. Incorporation of interaction between external high speed flow and damage geometry into thermomechanical analysis of a damaged TPS.

1.5 Outline of Dissertation

This dissertation contains seven chapters. It should be noted that the tables and figures associated with each chapter are presented at the end of the particular chapter.

Chapter II describes the preliminary FE analysis on damaged Shuttle HRSI tile TPS system using an approximate axisymmetric model using a number of simplifying assumptions.

In Chapter III, a more accurate three-dimensional FE model was developed and results

from this model are compared to those from the approximate axisymmetric model to determine the accuracy of the axisymmetric model. The validity of the simplifying assumptions used in Chapter II are systematically examined, by using more accurate assumptions, which are incorporated into the 3D model. The improved FE model is subsequently used to determine the effects of damage location on the thermomechanical response of the TPS.

Development of a thermal structures test facility is described in Chapter IV. The calibration of the facility as well as its performance are also considered. The facility, which uses radiant heaters, allows high-temperature experiments to be conducted on undamaged and damaged TPS. These experiments, described in Chapter V, provide the basis for validating the FE model that was developed and improved in previous chapters.

Subsequently, the validated model is extended to include modified heat loads that take into account the interactions of high-speed flow past a cavity in Chapter VI. Using the improved model, the relative effects of damage on the thermal protection capability and thermal stress within the TPS are determined by comparing the thermal and structural response of damaged configurations with the undamaged configuration.

The last chapter, Chapter VII contains the conclusions gleaned from the research conducted and the recommendations for future research.

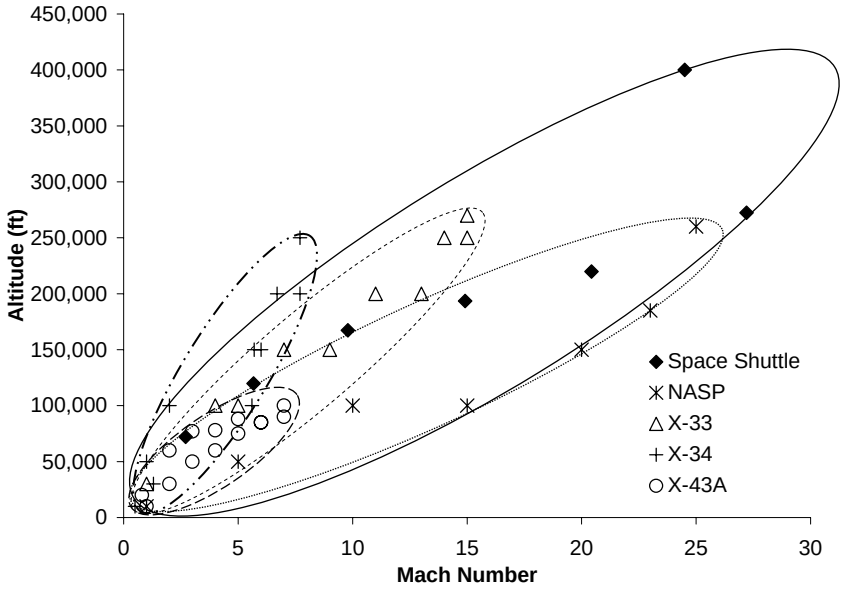

Figure 1.1: Flight envelopes for hypersonic vehicles

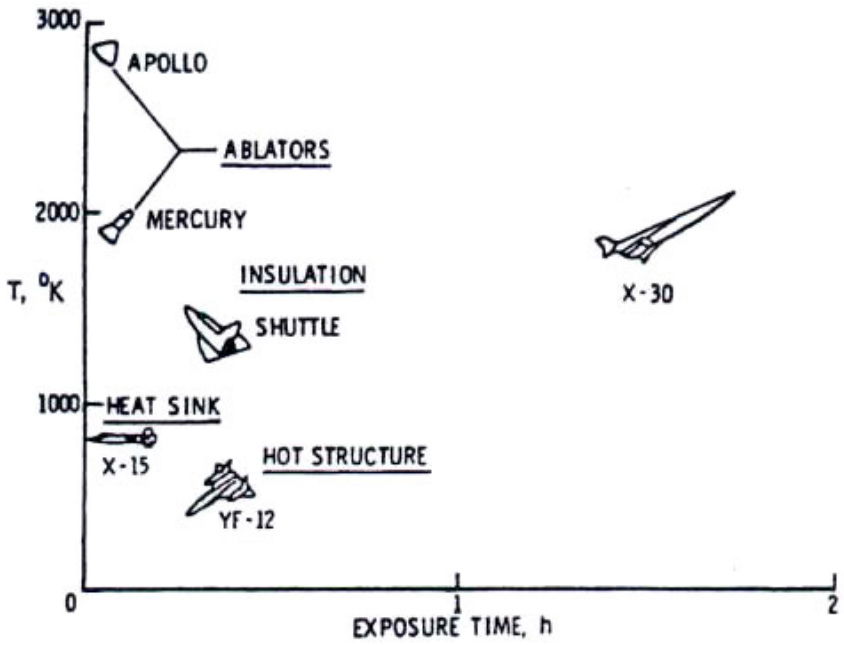

Figure 1.2: Temperatures and exposure times for hypersonic vehicles(Ref. 48, Pg. 19)

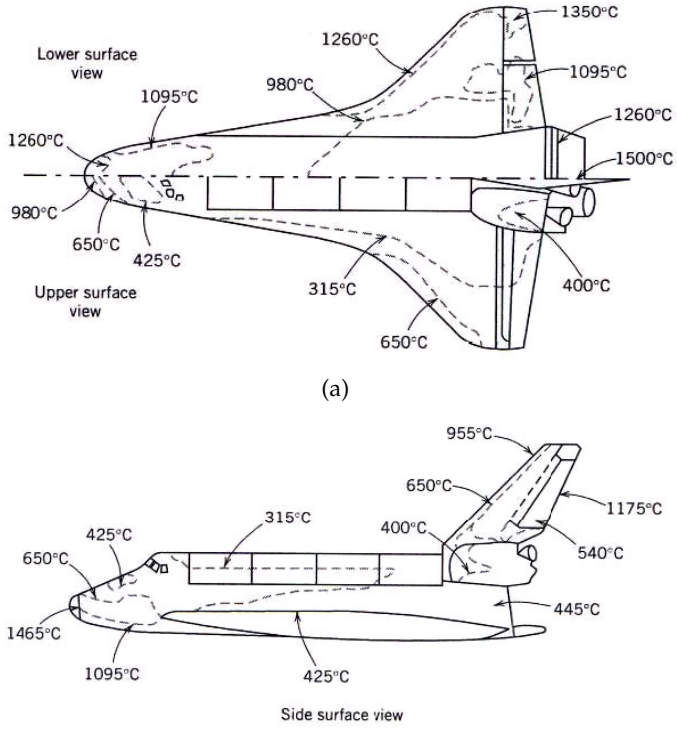

Figure 1.3: Approximate maximum re-entry temperatures on outer surface of Space Shuttle Orbiter (Ref. 5, Pg. W-98)

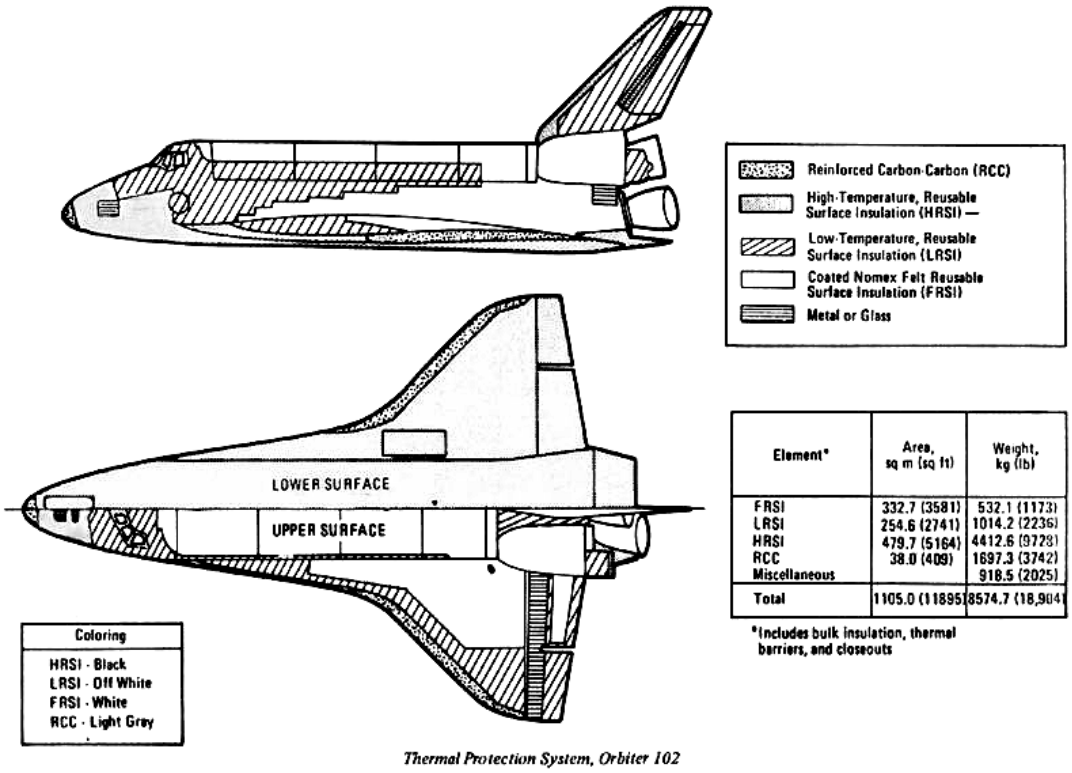

Figure 1.4: Locations of various TPS

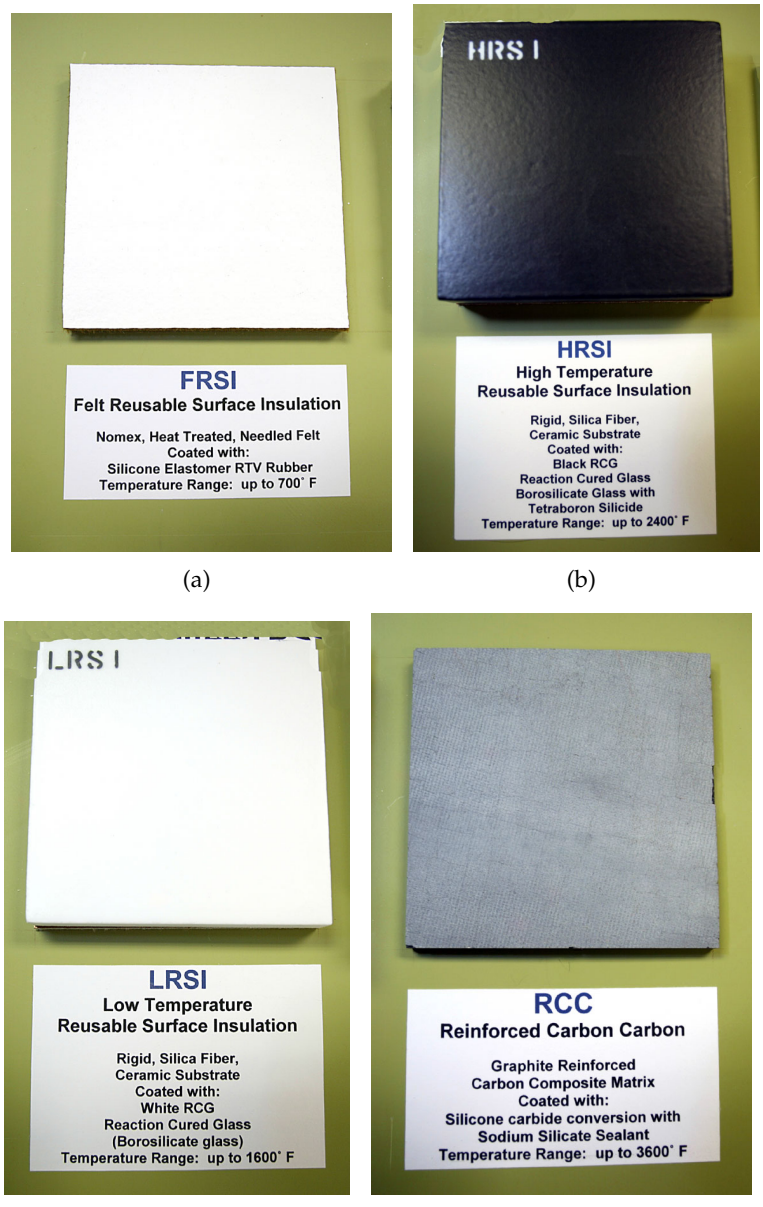

(a) (b)

(c) (d)

Figure 1.5: Initial materials used for Space Shuttle TPS)

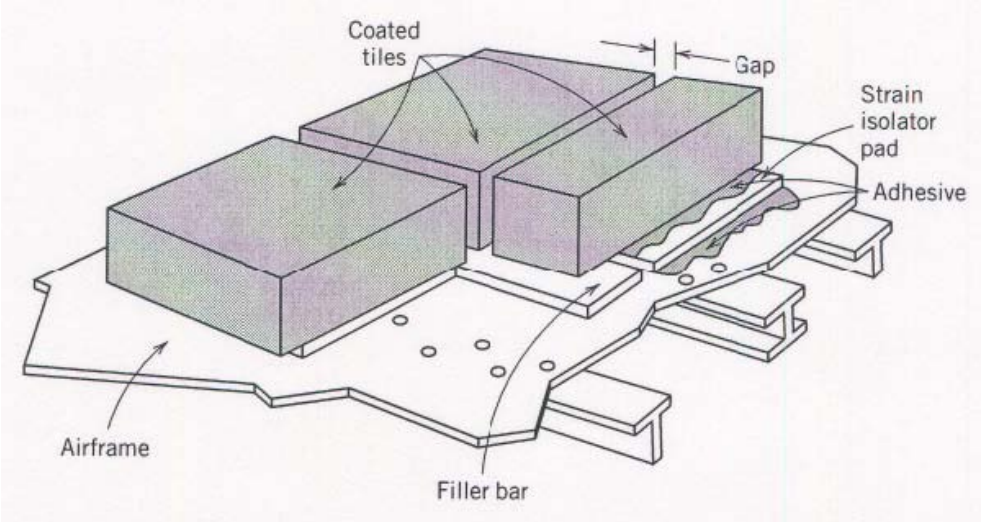

Figure 1.6: Space Shuttle HRSI Tile and Airframe (Ref. 5, Pg. W-102)

Figure 1.7: Advanced Flexible Reusable Surface Insulation

CHAPTER II

DAMAGE MODELING AND AXISYMMETRIC FINITE ELEMENT MODEL

Many studies utilize a one-dimensional model for the heat transfer analysis to size the TPS [4, 28], or to obtain approximate temperatures in vehicle structures for stress analysis [47]. While a one-dimensional model is generally sufficient to model non-damaged TPS, these models are insufficient when damage or heat shorts exist. For such cases, approximate two-dimensional models [24, 32] and full three-dimensional models [21, 26, 31] have to be used instead. Complete three-dimensional models are the most accurate, however they are more complex and entail more associated computational cost.

In this chapter, thermomechanical analysis on a damaged TPS is conducted using an approximate axisymmetric FE model. The TPS chosen for study is the HRSI tile system used on the space shuttle orbiter. The HRSI tiles are extensively used TPS on the shuttle and together with the RCC panels, protect the orbiter from the most severe aerodynamic heating sustained by the vehicle. However, unlike the RCC panels, HRSI tiles have low strength and are highly susceptible to damage.

2.1 TPS Damaged Model and Finite Element Mesh

The TPS is modeled as a discrete three layered system, shown in Figure 2.1, that resembles the actual configuration of the Shuttle Orbiter HRSI tile system shown in Figure 1.6 in the previous chapter. The axisymmetric model is based on the assumption that the system can be modeled as a circular segment, which for the specific case considered, has a diameter of 6", as shown in Figure 2.2. The damage profile depicted in Figure 2.2 simulates the so-called "hypervelocity impact" [6], which has an actual damage profile shown in Figure 2.3. For convenience, the actual damage configuration is replaced by an approximate damage profile that consists of a cylindrical hole, ending with a spherical cap. The total depth of the damaged region is equal to its diameter as shown in Figure 2.2.

The same mesh is used in both the heat transfer and thermal stress analyses, therefore it is important to ensure that the mesh produces converged results for both analyses. The presence of damage, material discontinuities, and corners give rise to stress concentrations that has to be taken into account during mesh generation. The mesh has to be sufficiently fine to capture the rapid variations. It should be noted that the stress concentration associated with the damaged region is less severe than those present at the edges and corners of the material interfaces. Figure 2.4(a) shows the finest mesh that was used in the convergence study. From the figure, it can be seen that the mesh is refined near the damaged region, as well as the edges and corners of the material interfaces. This axisymmetric FE mesh consists of $5,523$ elements with $16,850$ nodes. However, even with such considerable refinement, the mesh is unable to produce converged results. This suggests that stress singularities exist within the model and they were found to occur at the edges and corners of material interfaces. The presence of geometric and material discontinuities at these re-

gions gives rise to what is often called the "boundary-layer effect", where stress gradient changes rapidly.

Tong and Pian [49] concluded that refining meshes and increasing order of element formulation when using conventional finite elements, is inadequate for producing convergence in elasticity problems with singularities. Thus, the use of the finest mesh possible may not produce an accurate solution. Wang and Yuan [50] developed a singular composite-edge element which uses stress intensity factors to characterize singular edge stress field. The results in Reference 50 indicate that stress results based on the singular element start to deviate from results based on the conventional element when one is approaching within 5% (based on specimen length) of the location of the singularity. Assuming that the boundary layer effects in the TPS are confined to a region of similar proportions, a modified portion of the axisymmetric model with the boundary region shaded in grey is depicted in Figure 2.5. This boundary region is located at the periphery of the TPS with a width of 5% of its diameter near the material interfaces. Since the computational results are based on conventional elements, results in the shaded region are deemed to be unreliable. Thus, the meshes used ensure converged results only in the regions excluding the shaded areas in Figure 2.5.

The resultant converged FE mesh for the axisymmetric model with $D = 1$" damaged configuration is shown in Figure 2.4(b). This mesh consists of $1,280$ elements with $3,963$ nodes, which represent a significant reduction in the size of the problem when compared to the refined mesh in Figure 2.4(a).

The finite element model is used with ABAQUS code version 6.4 [15]. The DCAX8 elements are used for the heat transfer problem and the CAX8 elements for the thermal

stress problem. Both types of elements are eight-node biquadratic elements, shown in Figure 2.6, available in ABAQUS element library for axisymmetric analyses [15]. The DCAX8 has one degree of freedom per node, which is the temperature at the node. The CAX8 element has two degrees of freedom, u_r and u_z at each node representing the appropriate displacements.

2.2 Finite Element Analysis

All FE simulations in this dissertation are based on the ABAQUS code version 6.4 [15] to generate the thermomechanical response of damaged TPS. Thermal-mechanical coupling, which represents the conversion of mechanical energy to thermal energy, is neglected, compared to the large amount energy supplied to the system via thermal loading. Thus, the thermomechanical response of the system is obtained in two independent steps. In the first step, the heat transfer problem is solved to obtain the time-dependent temperature distribution in the TPS system due to the applied thermal loads and the boundary conditions. In the second step, the thermal stresses caused by the temperature distributions are determined. The solutions are facilitated by using the same mesh for both the heat transfer and thermal stress problems.

2.2.1 Heat Transfer Analysis

In the heat transfer analysis, the transient heat flux profile, $q_{ATS}(t)$ shown in Figure 2.7, is applied to the top surface of the TPS. The represents the re-entry heat flux profile for the Access to Space (ATS) reference vehicle [28]. The sides and the inner surface of the underlying structure are assumed to be perfectly insulated, representing a worst case scenario.

For the damaged configurations, there is considerable uncertainty regarding the effect of damage on the flow field and thus the heat load experienced by the TPS. To deal with this uncertainty, two thermal loading conditions, $q_1(t)$ and $q_2(t)$, which represent the lower and upper bounds of the heat load, respectively, are applied. On the undamaged surface, S_u shown in Figure 2.8, the ATS heat flux profile is applied. On the surface of the damaged region, S_d in Figure 2.8, no heat flux is applied for the lower bound case, while the ATS heat flux profile is applied for the upper bound case, thus:

$$Lowerbound: \qquad q_1(t) = \begin{cases} q_{ATS}(t) & \text{on } S_u \\ 0 & \text{on } S_d \end{cases} \tag{2.1}$$

$$Upperbound: \qquad q_2(t) = q_{ATS}(t) \quad \text{on } S_u \text{ and } S_d \tag{2.2}$$

The primary mode of heat loss in the TPS is due to radiation from the top surface of the tile. Emissivity (ε) of the tile surface is 0.85, and is assumed to be unaffected by damage. Convection heat loss is not considered in the analysis. On the undamaged surface, all radiated heat is lost to open space. However, in the damaged region, some of the heat radiated from the damaged surface is intercepted by opposite surfaces, as shown schematically in Figure 2.9, resulting in lower net heat loss to space. This cavity radiation in the damaged region is taken into account in the analysis by using the keyword commands *CAVITY DEFINITION and *RADIATION VIEWFACTOR in ABAQUS, which determines the heat exchange between element surfaces within the damage.

The unsteady heat transfer problem is solved in the time domain by using a suitable time-step, which is selected carefully so as to ensure convergence of the transient solution.

The magnitude of the time-step is determined by repeatedly solving the heat transfer problem with time-steps that are progressively reduced until convergence is achieved. When the difference in the temperature results between two consecutive time-steps is less than 1.0%, the solution is considered converged. New nodal temperatures are computed at each time-step based on the time-dependent thermal loading conditions as well as the temperature distribution obtained from the previous time step. The nodal temperatures at each time step are stored for subsequent use by the thermal stress analysis.

2.2.2 Thermal Stress Analysis

The thermal stress analysis is conducted for two types of boundary conditions, (a) the unrestrained, BC1, and (b) the restrained, BC2, boundary conditions. The schematic description of these boundary conditions is shown in Figure 2.10. These boundary conditions represent the upper and lower bounds for the actual condition that may exist in practice. The boundary conditions are applied only to the underlying structure since the tile and SIP are attached to the underlying structure in such a manner that they are not load bearing elements. Symmetric boundary conditions are applied to nodes lying on the axisymmetric line in the axisymmetric configurations.

The displacements and stresses at each time-step are computed using the time-dependent nodal temperatures from the heat transfer solution.

2.2.3 Material Properties and Simplifying Assumptions

A number of assumptions on material properties are used to simplify the analysis:

1. Emissivity of the LI-900 tile is unaffected by damage and is constant

2. Conductivities of the tile and SIP are functions of only temperature

3. LI-900 tile is isotropic

4. Mechanical properties of all materials are constant

The material properties of the LI-900 tile, SIP and underlying structure (aluminum 2024) can be found in Tables 2.1 – 2.3 respectively. The thicknesses of the SIP and underlying structure are 0.173" and 0.063" respectively. The thickness of the tile, 3.09", is chosen such that the maximum temperature attained by the underlying structure for the undamaged configuration is limited to $150\,^{\circ}\mathrm{C}$. The thermal emissivity of the tile surface is constant and equal to 0.85.

2.3 Results and Discussion

In this section, the damaged configurations are examined for three different levels of damage which are characterized by damage diameters, $D = 0.5", 1"$ and $1.5"$. The results for the damaged configurations are compared to the undamaged case, which represents the baseline case.

2.3.1 Axisymmetric Finite Element Results

The maximum temperatures that occur in the tile, SIP and underlying structure, and the times at which they occur for the undamaged and damaged configurations are shown in Table 2.4. Two values are listed for each damaged configurations: one for the q_1 thermal loading case in the left column and the other the q_2 thermal loading case, in the right

column. The percentage changes in the temperatures in the damaged configurations compared to the undamaged configuration are also indicated in the table.

In the tile, the maximum temperatures due to heat load q_1, are found to be unaffected by damage, while the maximum temperatures, due to heat load q_2, are found to increase with increasing damage size. For the SIP and underlying structure, the corresponding temperatures decrease and increase with increasing damage size. It should be noted that the maximum temperatures in the SIP and structure are reached long after the vehicle has landed, as implied by the duration of $2,100$ seconds given in Figure 2.7. This is a well-known behavior in return-from-space type of vehicles which experience temperature soaking after landing, and it can cause damage to the structure.

Figure 2.11 depicts the contour plots of the temperature distribution, in $^{\circ}\mathrm{C}$, at times when the maximum von Mises stresses for the tile occur for both the restrained and unrestrained boundary conditions. The color-coded contour bands for all plots represent the same values to allow comparison. These figures provide a comparison of the undamaged, and the $D = 1$" damaged configurations. The temperature contours for the q_1 thermal loading case are similar to the undamaged case except for changes due to the presence of damage. The temperatures associated with the damage for the q_2 thermal loading case are much higher, as evident in the presence of the yellow, orange and red contour bands shown in Figure 2.11(c).

The corresponding contour plots for the von Mises stresses in Pascal are shown in Figure 2.12. The von Mises stress [3], σ_E for the axisymmetric analysis is defined as

$$\sigma_{Eaxi} = \sqrt{\sigma_{rr}^2 + \sigma_{zz}^2 - \sigma_{zz}\sigma_{rr} + 3\sigma_{zr}^2} \tag{2.3}$$

This quantity is sometimes denoted as the equivalent tensile stress. The von Mises theory states that a ductile material will yield when the von Mises stress reaches the materials yield stress in uniaxial tension.

All three layers of the system are shown in Figure 2.12. A deformation magnification factor of 50 is applied in all figures. Since the maximum stress in the structure is two to three times larger than that in the tile, stresses larger than 140 kPa are represented by the maximum band, color-coded in red, while the rest of the contour bands are equally divided to represent the stresses below 140 kPa. The locations where the maximum stresses occur for the tile are also shown in the figures. Note that the contour plots between the restrained and unrestrained configurations for both q_1 and q_2 thermal loading cases are very similar. The principal effect of the boundary conditions is on the underlying structure, as will be shown later.

There are two time instances, denoted as t_1 and t_2 for convenience, where high von Mises stresses in the tile are observed. The precise value of t_1 and t_2 is dependent on the configuration and the level of damage. Table 2.5 shows the maximum von Mises stress in the tile and the times at which they occur for both thermal loading cases at t_1. In the table, two maximum stresses, one for the unrestrained boundary condition, BC1, and one for the restrained boundary condition, BC2, are provided. The percentage changes in these stresses in the damaged configurations, with respect to the undamaged configuration, are also indicated.

The maximum stresses in the tile are found to increase with damage for both q_1 and q_2 thermal loading cases, and the times when these stresses occur appear to be insensitive to damage size. These stresses occur approximately when the increasing surface heating rate

reaches a plateau, associated with the highest heat flux, as shown in Figure 2.7. For the q_1 heating case, the maximum stresses decrease with increasing damage size. These maximum stresses occur at the upper surface of the damaged region, shown in Figures 2.12(c) and (d). For the q_2 heating case, the maximum tile stresses occur inside the damaged region, as shown in Figures 2.12(d) and (e), and these stresses increase with increasing damage size.

High von Mises stresses in the tile at t_2 are only evident in cases with the unrestrained boundary condition. The maximum von Mises stresses for the tile at time t_2 are shown in Table 2.6. The maximum von Mises stress in the tile at t_2 occurs at the edge of the tile, at the tile-SIP interface which is a site of stress concentration. The maximum stresses for the SIP occur at the edge of the SIP, but depending on the configuration, either at the tile-SIP or SIP-underlying structure interface which are also regions of stress concentration.

The maximum von Mises stresses and the times at which they occur for the SIP for both the restrained and unrestrained boundary conditions are shown in Table 2.7, while that for the underlying structure are in Table 2.8. Damage decreases the maximum stresses in the SIP as well as in the underlying structure for the lower bound thermal loading case, q_1, but increases the maximum stresses for the upper bound thermal loading case, q_2.

T (°C)	**c (J/kg °C)**	**k (W/m °C)**
-73.2	787.0	163.0
26.9	875.0	177.0
126.9	925.0	186.0
326.9	1042.0	–

$\rho = 2770$ kg/m^3
E = 30 kPa
$\nu = 0.33$
$\alpha = 18 \times 10^{-6}$/°C

Table 2.1: Material properties of the underlying structure (Aluminum 2024)

T (°C)	**c (J/kg °C)**	**k (W/m-°C)**
-17.6	1306.3	0.03271
93.5	1339.8	-
204.6	1402.6	0.04636
615.7	1444.5	0.06604

ρ = 194 kg/m^3
E = 807 kPa
ν = 0.3
$\alpha = 18 \times 10^{-6}$/°C

Table 2.2: Material properties of SIP

T (°C)	c (J/kg °C)	k (W/m °C)
-17.6	628.0	0.03165
121.3	879.2	0.03894
260.2	1055.1	0.04779
399.1	1151.4	0.05626
538.0	1205.8	0.06791
676.9	1239.3	0.08536
815.7	1256.0	0.1065
926.9	1264.4	–
954.6	1268.6	0.1327
1093.5	–	0.1632
1260.2	–	0.2006

ρ = 144 kg/m^3
E = 172.4 MPa
ν = 0.16
α = 606 $\times 10^{-6}$/°C

Table 2.3: Material properties of LI-900 tiles

TPS Element	*D* (inch)	Temperature (°C)		% change		Time (s)	
Tile	0	981		NA		850	
	0.5	981	1462	0	49.0	850	850
	1.0	981	1501	0	53.0	850	850
	1.5	981	1516	0	54.5	850	850
SIP	0	150		NA		6600	
	0.5	148	158	-1.3	5.3	6600	6550
	1.0	143	188	-4.7	25.3	6450	6250
	1.5	136	245	-9.3	63.3	6200	5600
Underlying structure	0	150		NA		7150	
	0.5	148	158	-1.3	5.3	7150	7100
	1.0	142	187	-5.3	24.7	7050	6800
	1.5	135	244	-10.0	62.7	6850	6100

Table 2.4: Maximum temperatures and times at which they occur in tile, SIP and underlying structure in axisymmetric models

Thermal Loading	*D* (inch)	Max. von Mises stress (kPa)		% change		Time (s)	
		BC1	BC2	BC1	BC2	BC1	BC2
q_1	0	61.9	62.0	NA	NA	350	350
	0.5	107.0	107.1	72.9	72.7	350	350
	1.0	94.7	94.8	53.0	52.9	350	350
	1.5	86.4	86.5	39.6	39.5	350	350
q_2	0	61.9	62.0	NA	NA	350	350
	0.5	133.4	133.6	115.5	115.5	400	400
	1.0	136.5	136.7	120.5	120.5	400	400
	1.5	152.0	152.1	145.6	145.3	400	400

Table 2.5: Maximum von Mises stresses and times at which they occur in tile for the axisymmetric case at t_1 for the two different thermal loading conditions

Thermal Loading	*D* (inch)	Max. von Mises stress (kPa)	% change	Time (s)
q_1	0	47.0	NA	7050
	0.5	46.9	-0.2	7050
	1.0	44.9	-4.5	7000
	1.5	42.1	-10.4	6750
q_2	0	47.0	NA	7050
	0.5	50.6	7.7	7050
	1.0	61.5	30.9	6700
	1.5	82.2	74.9	6000

Table 2.6: Maximum von Mises stress and times at which they occur in tile for the axisymmetric case at t_2 for the two different thermal loading conditions

Thermal Loading	D (inch)	Max. von Mises stress (kPa)		% change		Time (s)	
		BC1	BC2	BC1	BC2	BC1	BC2
q_1	0	22.0	4.04	NA	NA	7200	6750
	0.5	21.6	3.97	-1.8	-1.7	7150	6750
	1.0	20.7	3.80	-5.9	-5.9	7050	6650
	1.5	19.4	3.56	-11.8	-11.9	6800	6400
q_2	0	22.0	4.04	NA	NA	7200	6750
	0.5	23.3	4.28	5.9	5.9	7100	6700
	1.0	28.4	5.20	29.1	28.7	6800	6400
	1.5	38.0	6.95	72.7	72.0	6050	5700

Table 2.7: Maximum von Mises stress and times at which they occur in the SIP for the axisymmetric case for the two different thermal loading conditions

Thermal Loading	D (inch)	Max. von Mises stress (MPa)		% change		Time (s)	
		BC1	BC2	BC1	BC2	BC1	BC2
q_1	0	1.05	281.2	NA	NA	7350	7150
	0.5	1.04	277.0	-1.0	-1.5	7350	7150
	1.0	0.99	265.1	-5.7	-5.7	7350	7050
	1.5	0.93	248.5	-11.4	-11.6	7100	6850
q_2	0	1.05	281.2	NA	NA	7350	7150
	0.5	1.12	298.5	6.7	6.2	7300	7100
	1.0	1.36	363.1	29.5	29.1	7000	6800
	1.5	1.82	486.0	73.3	72.8	6300	6100

Table 2.8: Maximum von Mises stress and times at which they occur in underlying structure for the axisymmetric case for the two different thermal loading conditions

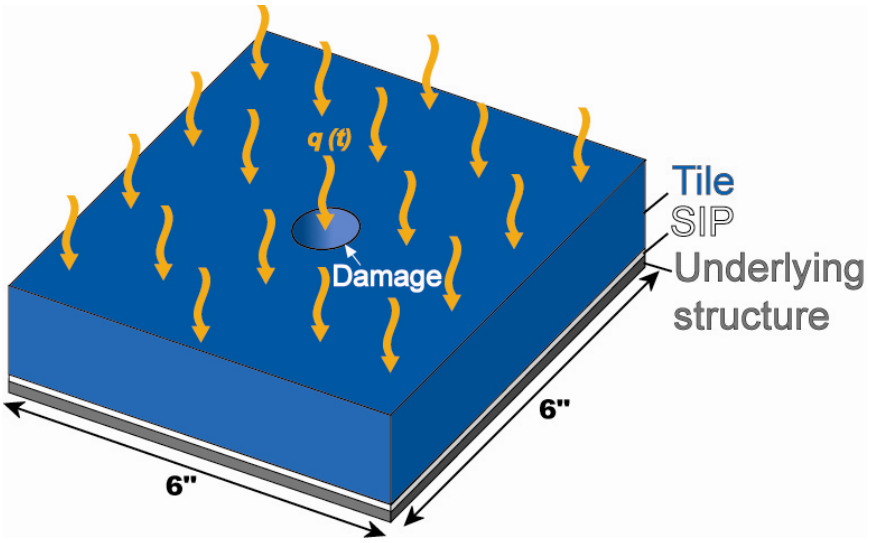

Figure 2.1: Schematic view of square segment of the three-layered TPS configuration

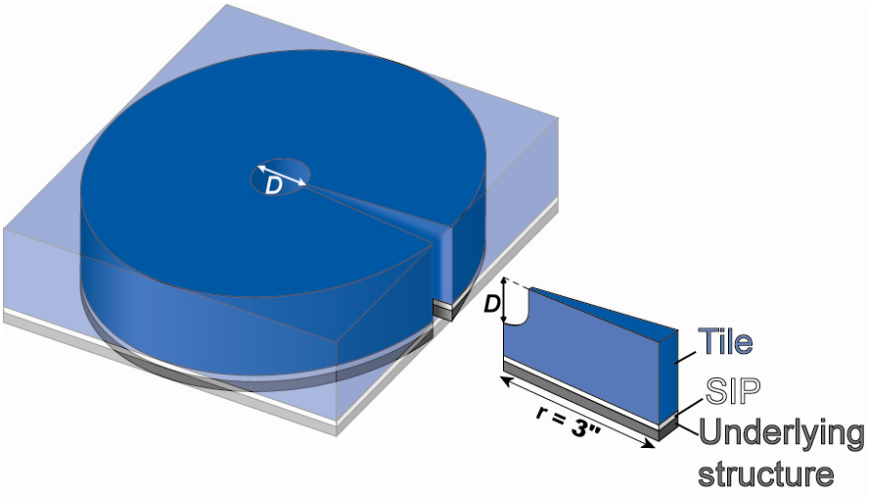

Figure 2.2: Approximate circular axisymmetric configuration

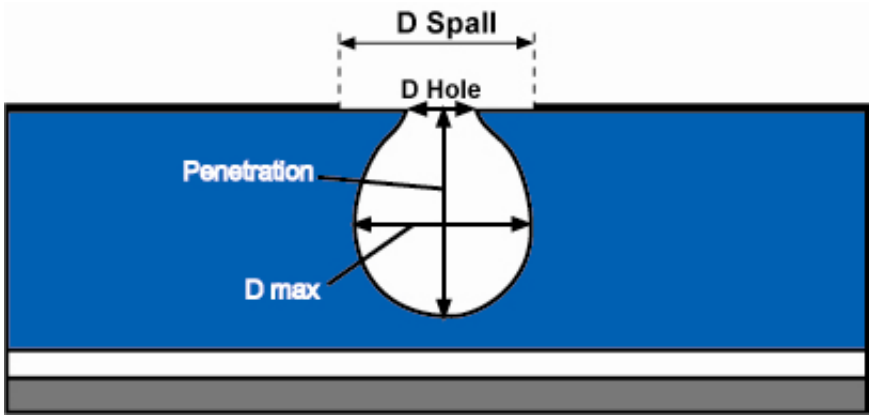

Figure 2.3: Damage geometry associated with hypervelocity impact

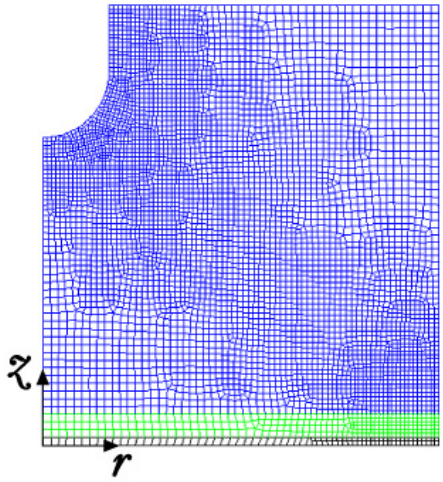

(a) Finest mesh used in convergence study

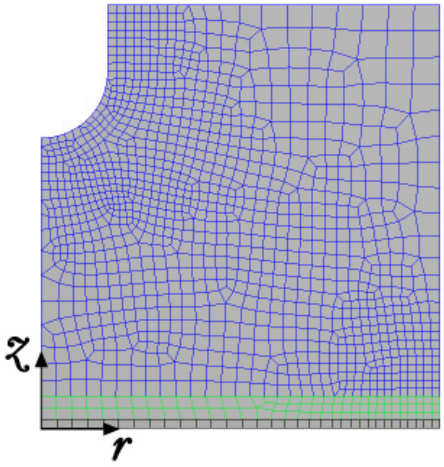

(b) Converged mesh used in FE analysis

Figure 2.4: FE meshes of axisymmetric model illustrating damage geometry and coordinate system

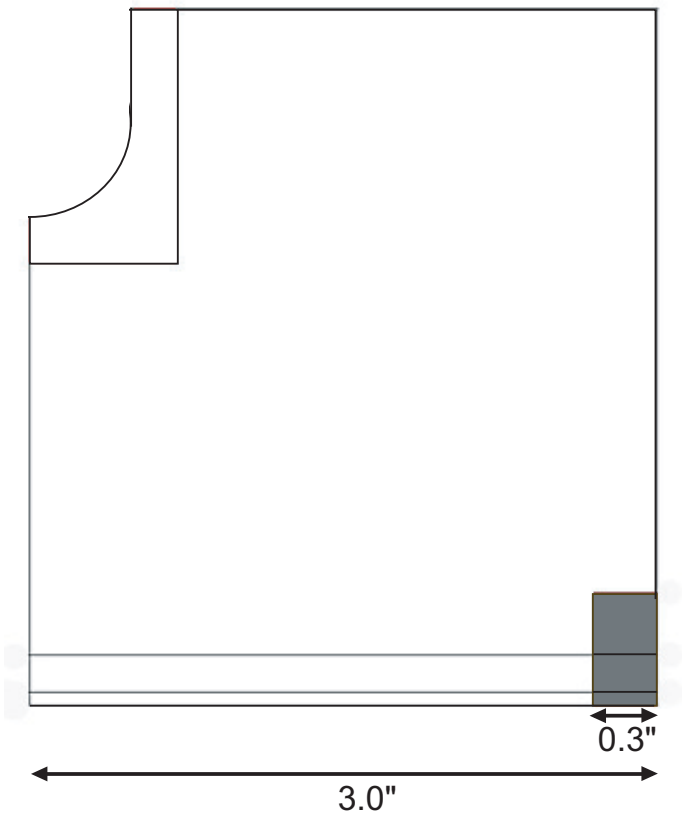

Figure 2.5: Boundary layer region for axisymmetric model

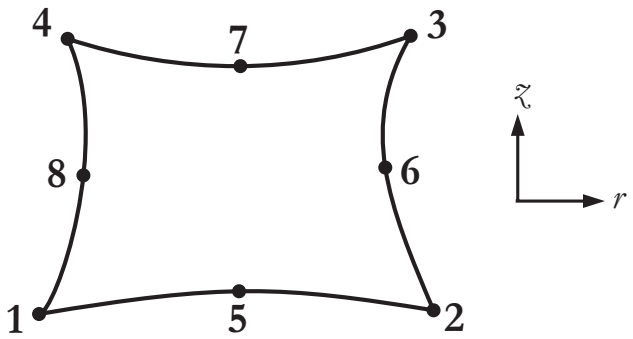

Figure 2.6: 8-node biquadratic elements used for axisymmetric model

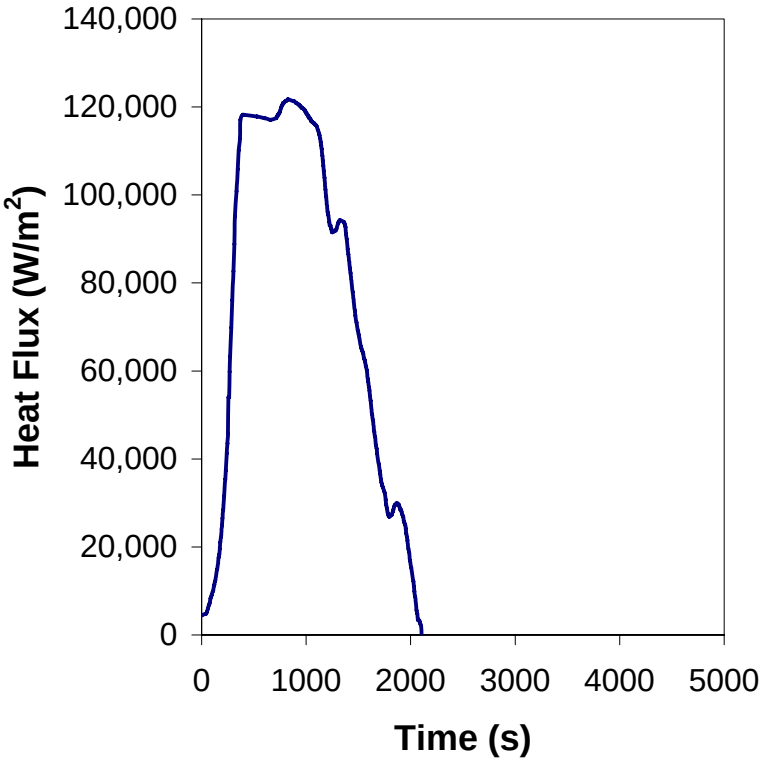

Figure 2.7: Re-entry heat flux loading profile for the ATS vehicle

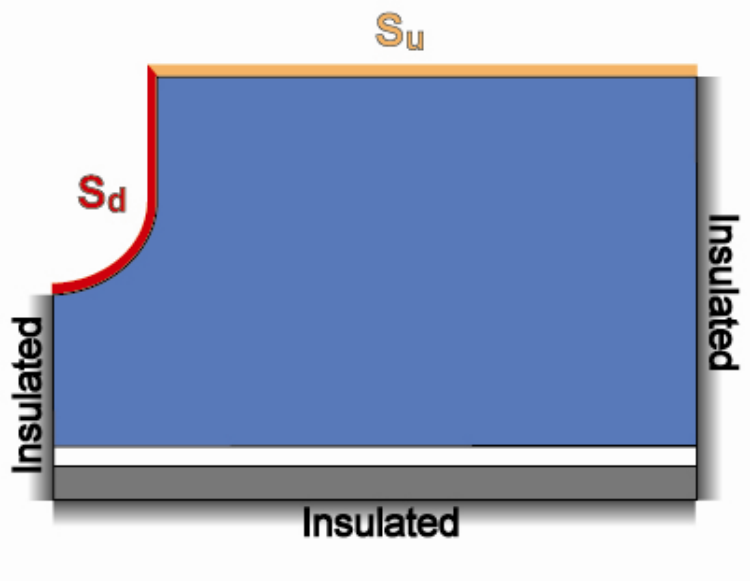

Figure 2.8: Cross section of TPS showing the undamaged and damaged surfaces subjected to thermal loading

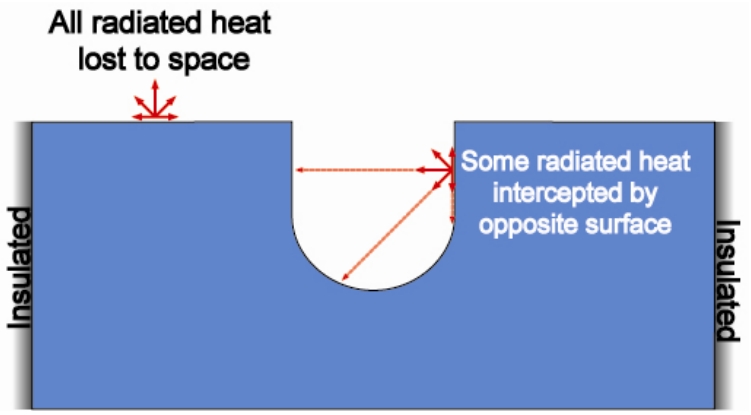

Figure 2.9: Schematic representation of radiation heat loss in the tile

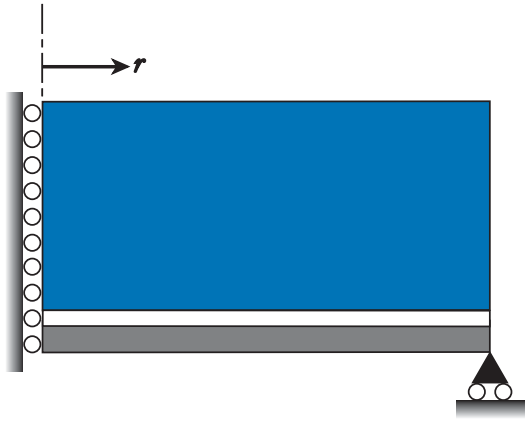

(a) Unrestrained boundary condition, BC1

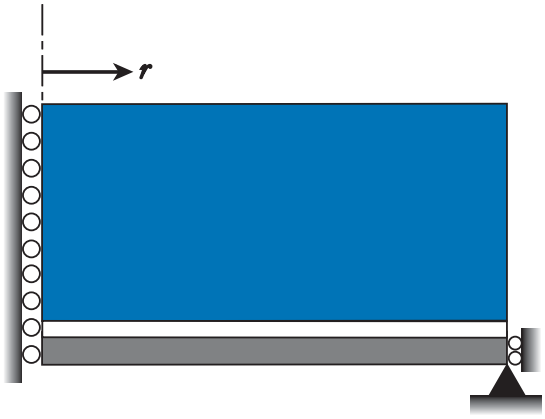

(b) Restrained boundary condition, BC2

Figure 2.10: Structural boundary conditions applied to underlying structure

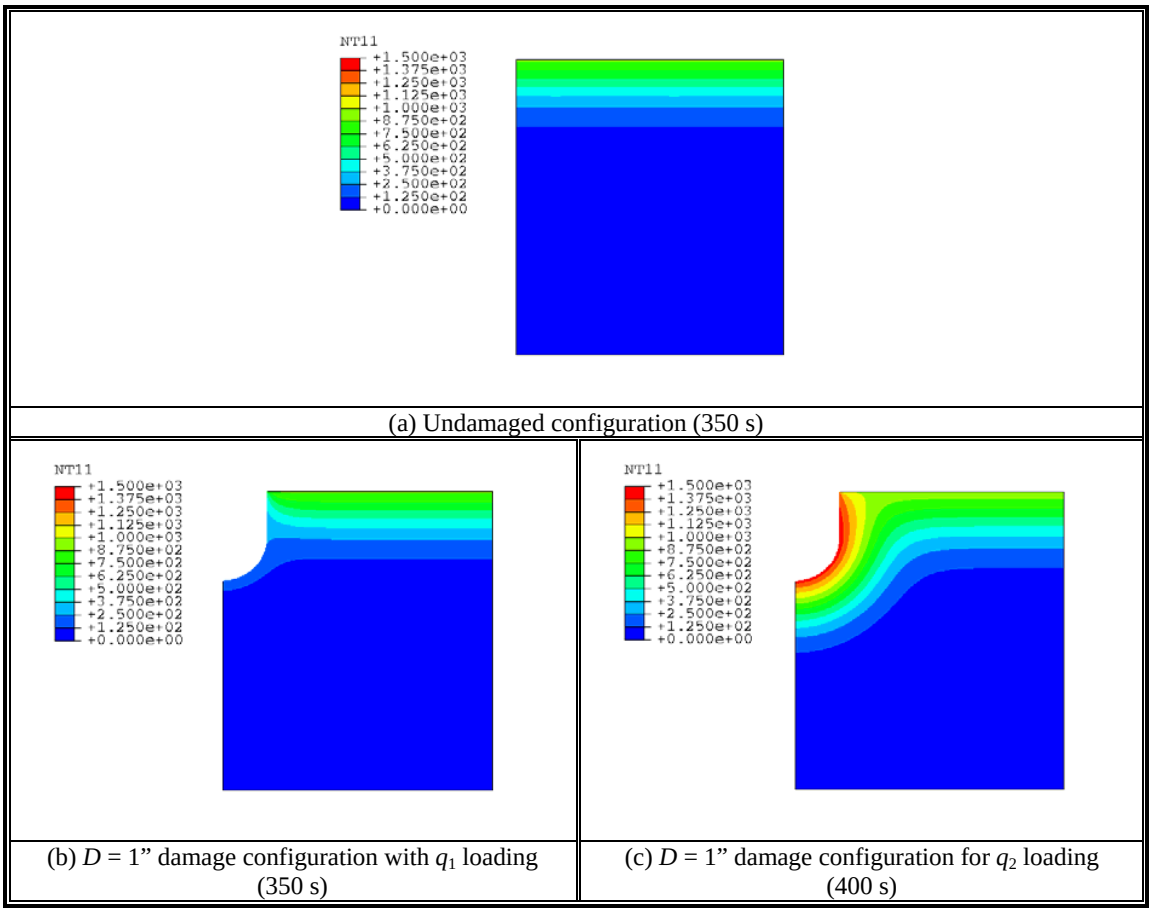

(a) Undamaged configuration (350 s)

(b) D = 1” damage configuration with q_1 loading (350 s)

(c) D = 1” damage configuration for q_2 loading (400 s)

Figure 2.11: Temperature contour plots for the undamaged and D = 1″ damaged axisymmetric models for the two different heat loads at times when the maximum von Mises stress in tile occurs. Legend indicates temperatures in °C

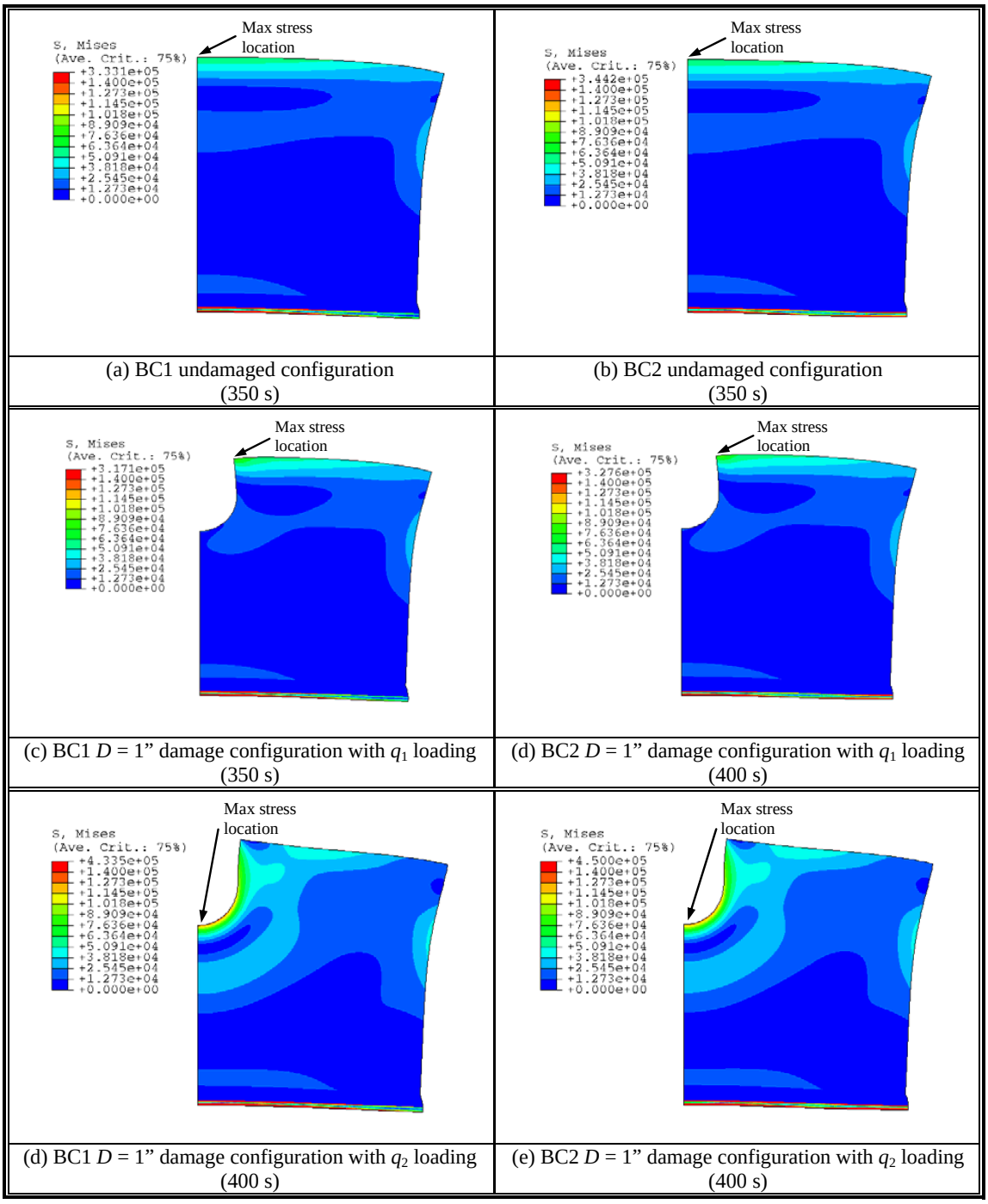

(a) BC1 undamaged configuration (350 s)

(b) BC2 undamaged configuration (350 s)

(c) BC1 D = 1" damage configuration with q_1 loading (350 s)

(d) BC2 D = 1" damage configuration with q_1 loading (400 s)

(d) BC1 D = 1" damage configuration with q_2 loading (400 s)

(e) BC2 D = 1" damage configuration with q_2 loading (400 s)

Figure 2.12: von Mises stress contour plots for the undamaged and D = 1″ damaged axisymmetric models for the two different heat loads at times when the maximum von Mises stress in tile occurs. Legends indicate stresses in Pascal

CHAPTER III

THREE DIMENSIONAL FINITE ELEMENT MODEL

In this chapter, a three-dimensional (3D) FE model is developed to determine the thermomechanical behavior of damaged TPS. The 3D model is a more realistic representation of the actual configuration of the Shuttle Orbiter HRSI tile system and thus, is more accurate than the axisymmetric model. Results generated from the 3D model are used to assess the accuracy of the axisymmetric model. Simiplifying assumptions used in the previous chapter are also replaced with more accurate assumptions to ensure that the 3D model is capable of representing the TPS under realistic conditions.

The 3D model is also used to determine the influence of damage location on the thermomechanical behavior of the TPS. In the axisymmetric model, damage is assumed to occur at the center of the tile, since off-center damage cannot be accurately modeled. However, the 3D model is not subjected to such limitations. Influence of damage location is determined by moving the damage location from the center of the tile by an offset distance, $\delta = 1$" or 2", as shown in Figure 3.1.

3.1 Finite Element Analysis and Meshing Considerations

The TPS is the same discrete three-layered structure described in the previous chapter and shown in Figure 2.1. Due to symmetry considerations, TPS with centrally located damage can be represented by a quarter model, while TPS with off-centered damage requires a half model. The idea of boundary layer introduced in the previous chapter is used again and the boundary layer for the 3D model is shown in Figure 3.2. The FE meshes generated for TPS with damage of size $D = 1$" located centrally, and displaced from center by $\delta = 1$" are shown in Figure 3.3. The quarter model consists of $57,702$ elements and $96,184$ nodes, and the half model consists of $112,697$ elements with $164,368$ nodes. The DC3D10 and C3D10 elements are used for the heat transfer and thermal stress analysis, respectively. These are ten-node quadratic tetrahedron elements shown in Figure 3.4. The DC3D10 elements have one degree of freedom per node, which is the temperature at the node, and the DC3D10 element has three degrees of freedom, u_x, u_y and u_z, at each node representing the appropriate displacements.

The FE procedures used to determine the temperature distribution and thermal stress of the TPS are similar to those described in Chapter II. Similar boundary conditions, shown in Figure 3.5, are also used.

3.2 Simplifying Assumptions

Recall the simplifying assumptions that were used in the previous chapter:

1. Emissivity of the LI-900 tile is unaffected by damage and is constant.

2. Conductivities of the tile and SIP are assumed to be functions of only temperature.

3. LI-900 tile is assumed to be isotropic.

4. Mechanical properties of all materials are constants.

While these assumptions have facilitated the FE solution obtained earlier, the model based on these assumptions may be inaccurate. Thus, the limitations introduced by these simplifying assumptions are removed in this chapter by introducing more realistic assumptions that enhance the accuracy of the model. The consequences of replacing these simplifying assumptions on FE results are examined. The improved assumptions are given below:

1. Emissivity of damaged surface of LI-900 tile is a function of temperature.

2. Conductivities of tile and SIP are functions of both temperature and pressure.

3. LI-900 tile is transversely isotropic.

4. Mechanical properties can be functions of temperature.

3.3 Results and Discussion

The results are presented in four sections: first, results generated using the 3D model with assumptions used in Chapter II are presented and these results are compared with those generated by the axisymmetric model to determine the relative accuracy of the axisymmetric model. Second, the validity of assumptions used in the previous chapter is examined systematically. Third, the thermomechanical behavior of TPS using the 3D model with improved assumptions are described. Last, the effect of damage location on the thermomechanical response of the TPS is discussed.

3.3.1 Results for 3D Model Using Assumptions From Previous Chapter

The maximum temperatures that occur in the tile, SIP and underlying structure, and the times at which they occur for the undamaged and damaged configurations are shown in Table 3.1. The general dependence of the temperatures on damage size resembles that for the axisymmetric case; temperatures are found to decrease with increasing damage size for the q_1 loading case and they increase with increasing damage size for the q_2 loading case. The lower bound maximum temperatures in the tile occur outside of the damaged area and are not affected by cavity radiation, thus these temperatures are insensitive to damage. The upper bound maximum temperatures for the tile, which occur within the damaged area of the tile, increased significantly. For the 3D model, the $D = 1.5$" damage increases the temperature by 54.4% to $1515\,^{\circ}\mathrm{C}$, which is below the melting temperature of the tile, $1700\,^{\circ}\mathrm{C}$, but above its softening temperature of $1370\,^{\circ}\mathrm{C}$.

For the SIP and underlying structure, the lower bound temperatures are found to decrease with increasing damage size. However, the upper bound maximum temperatures for these layers increase with increasing damage size. Since no heat flux is applied to the damaged surface for the q_1 case, the presence of damage reduces the surface area subjected to heating. Therefore, the total heating rate is reduced, resulting in lower amount of energy supplied to the TPS. For the q_2 case, the presence of damage increases the surface area subjected to the thermal loading, at the same time allowing the heat load to penetrate deeper into the system resulting in higher temperatures. For the $D = 1.5$" damaged configuration, the temperature in the structure is found to increase by 49.3%.

Contour plots of the temperature, in $^{\circ}\mathrm{C}$, and the von Mises stress, in Pascal, similar to those presented in the previous section, are shown in Figures 3.6 and 3.7, respectively. The

von Mises stress [3], for the 3D case is defined as

$$\sigma_{E_{3D}} = \sqrt{\sigma_{xx}^2 + \sigma_{yy}^2 + \sigma_{zz}^2 - \sigma_{xx}\sigma_{yy} - \sigma_{yy}\sigma_{zz} - \sigma_{zz}\sigma_{xx} + 3\sigma_{xy}^2 + 3\sigma_{yz}^2 + 3\sigma_{zx}^2} \tag{3.1}$$

The contour plots for the restrained and unrestrained cases are similar. Thus only the unrestrained configurations are shown in Figure 3.7. Note the similarities in the contour features between the axisymmetric and 3D models close to the damaged region. These similarities diminish as one moves away from the damaged region towards the edge.

The maximum von Mises stresses for the tile at t_1 are shown in Table 3.2. In the q_1 case, the highest temperature associated with the damaged region is found on the upper surface of the damage. Even though the temperature is approximately equal to that in the undamaged configuration, the stress increases due to the stress concentration of the damage. Unlike the stress concentrations caused by material discontinuities and sharp corners, the stress concentration in the damaged region is mild and can be adequately resolved by the mesh. In the q_2 case, the maximum temperature occurs within the damaged region. The higher temperatures, coupled with the stress concentration introduced by the damage, increase the stresses significantly. For the axisymmetric model, the maximum stress in the tile at t_1 for the q_2 thermal loading case increases with respect to damage size, but for the 3D model, the maximum stress for the $D = 0.5$" damaged configuration is larger than that for the $D = 1$" damaged configuration, even though temperatures are higher in the $D = 1$" damaged configuration.

The maximum tile stresses that occur at t_2 are given in Table 3.3 and the maximum von Mises stresses in the SIP and underlying structure are shown in Tables 3.4 and 3.5, respectively. As evident, the maximum values occur approximately at the time when the SIP

and structure reach their maximum temperatures, and they are caused predominantly by the mismatch in the coefficients of thermal expansion associated with the different layers. These maximum stresses depend on the maximum temperatures reached by the SIP and structure, and the total heat applied to the system. Increasing damage decreases these stresses for the q_1 loading case and increases that for the q_2 loading case. These high stresses do not show up in the tile and SIP for the restrained case, because the boundary condition prevents the structure layer from expanding, and thus reduces the effect of mismatch in the coefficients of thermal expansion. This constraint in thermal expansion of the underlying structure in the restrained case also induces much higher stresses in the underlying structure than those present in the unrestrained case.

The differences in maximum temperature and stress results between the axisymmetric and 3D model are shown in Figures 3.8 through 3.11. The percentage difference in maximum temperatures and stresses, E_T and E_σ, respectively, are defined as

$$E_T = \frac{T_{axi} - T_{3D}}{T_{3D}} \cdot 100\% \tag{3.2}$$

$$E_\sigma = \frac{\sigma_{axi} - \sigma_{3D}}{\sigma_{3D}} \cdot 100\% \tag{3.3}$$

where T_{axi} and T_{3D} are the maximum temperatures for the axisymmetric and 3D models, respectively, and σ_{axi} and σ_{3D} are the maximum von Mises stress for the axisymmetric and 3D model, respectively.

The maximum temperatures in the tile for both axisymmetric and 3D cases are very similar. The simplification due to the axisymmetric case is equivalent to removing material from the corners of the 3D model and modifying the boundary conditions accordingly. The maximum temperatures in the tile occur on the undamaged tile surface or the surface

within the damaged region. The axisymmetric assumption does not influence the surface properties and damage geometry, therefore the differences between the maximum tile temperatures of the two analyses are small, less than 0.35%.

The difference in temperature results between the axisymmetric and 3D cases for the SIP and structure layers are more significant. The size and geometry of the damaged region are the same in both models, so the change in energy experienced by the TPS is the same. The reduction in mass for the axisymmetric model allows the SIP and structure to experience a larger change in temperatures for the same amount of heat input or loss. Thus, the changes in maximum temperatures present in the SIP and underlying structure, due to damage, are higher for the axisymmetric case than in the 3D case.

The differences in maximum stresses in the tile at t_1 are relatively small, up to about 11%. These stresses occur in the damaged region that is distant from the edges, it is relatively insensitive to the simplifying assumptions associated with the axisymmetric model. For the 3D models, the maximum SIP stresses and tile stresses at t_2, occur at the corners of the material interfaces, which are not modeled in the axisymmetric case. Thus, the stresses in the tile at t_2 and the SIP selected for comparison in the axisymmetric and 3D models are from different locations. The stress concentrations in the 3D model are also more substantial than the axisymmetric case, thus differences in these stresses are larger.

Like for the SIP, the maximum stresses for the unrestrained structure in the 3D model also occur at the corners, but not at the material interface. Thus, the differences in the maximum stresses are large. The restrained boundary condition results in very high stresses, with little variation, in the underlying structure. While the locations of maximum stresses in the underlying structure for the restrained axisymmetric and square cases are different,

the small variation in the stress results produces smaller differences. Note that these differences are approximately of the same magnitude as those for temperatures in the structure.

For the maximum temperature results, the axisymmetric model yields relatively good results for the damage sizes considered, with differences less than 9%. For the stress results, the differences can be as high as 57%, because these stresses in the 3D models occur in regions that are not captured by the axisymmetric model. It should be noted however, that the 3D models require approximately 15 times more degrees of freedom when compared to the axisymmetric cases. Therefore the approximate axisymmetric models are useful for rapid trend-type studies where accuracy is less important than computational efficiency.

3.3.2 Validity of Assumptions Used in The Previous Chapter

The axisymmetric model is used to determine the validity of the simplifying assumptions used in the previous chapter. While the axisymmetric model is not as accurate as the 3D one, it is, nonetheless, capable of predicting correct trends without excessive computational cost.

Starting with the analysis carried out in the previous chapter, each of the simplifying assumptions described earlier is replaced with more accurate assumption one at a time. Using this systematic approach, the results from the approximate analysis are compared to the improved results to assess the influence of each simplifying assumption. For the results in this section, the q_2 thermal load and BC2 boundary condition are used, since they represent the more severe case.

The thickness of the tile is chosen such that the maximum temperature attained by the underlying structure is limited to $150\,^{\circ}\mathrm{C}$. Depending on whether its conductivity is

assumed to be a function of both temperature and pressure, or just a function of temperature, the required tile thicknesses are different. The material properties, density (ρ), specific heat (c), thermal conductivity (k), Young's modulus (E), Poissons ratio (ν) and coefficient of thermal expansion (α) used in the analyses for the underlying structure (Aluminum 2024) are given in Table 3.6. The conductivity of the SIP as a function of pressure and temperature are given in Table 3.7 and its other material properties are shown in Table 3.8. The conductivity of the LI-900 tile as a function of pressure and temperature can be found in Table 3.9. The tile is transversely isotropic, which implies that its in-plane (xz-plane) properties are different from the out-of-plane (y-direction) properties. The first value listed is the in-plane conductivity and the value in parentheses is the out-of-plane conductivity. Other material properties of the tile are given in Table 3.10. These material properties are collected from a number of sources [2, 40, 40]

Emissivity of damaged surfaces as a function of temperature

In the previous chapter, the emissivity of the tile ($\varepsilon = 0.85$) was assumed to be unaffected by damage. In reality, the tile is coated by a reaction cured glass (RCG) that enhances the emissivity characteristics of the tile and limits moisture absorption. Since damage breaches the tile coating, it affects the emissivity. The emissivity of the uncoated tile is a function of temperature (See Table 3.11) and it decreases with increasing temperature. Assuming that damage totally removes the coating, a new analysis using the axisymmetric, $D = 1$" damage configuration is conducted. The emissivity of the damaged region is now assumed to be temperature-dependent and the emissivity values used correspond to those of an uncoated tile.

The maximum temperatures reached by each TPS component are shown in Table 3.12.

The rapid decrease in emissivity in the damaged region, coupled with the effect of cavity radiation, severely reduces the radiation heat lost from the surface resulting in very high temperatures in the TPS. The results clearly indicate that assuming emissivity to be unaffected by damage leads to an under-prediction of the maximum temperatures in the system by as much as 31% and this error is likely to increase with increasing damage size.

Conductivity of Tile as a Function of Both Temperature and Pressure

Previously, the conductivity of the tile and SIP were assumed to be only a function of temperature, i.e. $k = f(T)$ and the conductivity at $P = 1013.3$ Pa in Table 3.9 was used. However, due to the porous nature of the tile, its conductivity is actually a function of both temperature and pressure, i.e. $k = g(T, P)$. During re-entry, the static pressure changes from almost zero to atmospheric pressure, which affects the conductivity. To determine effect of the previous assumption, a new analysis using the undamaged axisymmetric model, with the tile and SIPs conductivities that depend on both temperature and pressure, is conducted.

The TPS is assumed to be exposed to the pressure profile shown in Figure 3.12, which is the re-entry profile of the ATS vehicle. There is relatively small increase in pressure in the initial $2,400$ seconds, followed by a rapid rise to atmospheric pressure at about $3,000$ seconds. Thus, in the previous analysis, the conductivity of the tile used is higher initially, until about 965 seconds, and becomes lower in the later stage of the analysis.

The thickness of the tile is determined by the limit on the maximum temperature attained by the underlying structure, which is assumed to be $150\,^{\circ}\mathrm{C}$. The inclusion of pressure dependency for conductivity in the tile reduces the required thickness by approxi-

mately 5%, from 3.09" to 2.94".

Figure 3.13 depicts the transient temperature results for both the approximate and improved analyses at the surface and center of the tile, as well as at the underlying structure. The surface temperature of the tile is largely unaffected by the previous simplifying assumption. However, the temperature distributions within the TPS changed by a significant extent. The higher initial conductivity used in the previous analysis allowed heat to penetrate faster, resulting in higher temperatures at the center of the tile as seen in the Figure 3.13(b). For the later times, the reduced conductivity slows the heat penetration into the underlying structure, increasing the time required before the structure reaches its maximum temperature as indicated in Figure 3.13(c). The lower conductivity also reduces the heat loss from the TPS by preventing the heat that has penetrated into the TPS from being conducted back to surface of the tile as the surface cools. This aggravates the effects of temperature soaking, and thus the tile had to be thicker in the previous analysis.

The temperature results from the improved analysis are used to determine the thermal stresses in the TPS. The maximum von Mises stresses that occur in the tile, SIP and underlying structure subjected to the BC2 boundary condition using the previous and new temperature results are presented in Table 3.13. When neglecting the pressure dependence of the conductivity, the von Mises stress in the tile is underestimated by 13.8%. The higher initial conductivity for the simplifying assumption results in less severe thermal gradients, which yield lower stresses. However, the increased thickness requirement of the tile produces higher stresses in the SIP and underlying structure.

The assumption that the conductivities of the tile and SIP is only a function of temperature yields conservative results in TPS sizing and the heat transfer analysis, however,

it underestimates the maximum stresses in the tile significantly. Thus, it is important to include the pressure dependence of conductivity, in order to obtain conservative thermal stress results.

Tile as a Transversely Isotropic Material

In the previous analysis, the tile was assumed to be isotropic. The tile is actually transversely isotropic, where its out-of-plane properties are different from its in-plane properties. In the heat transfer analysis, only conductivity of the material is affected by this assumption and in the thermal stress analysis, only the elastic material properties are affected. To determine these effects, results from analyses using isotropic and transversely isotropic material properties are compared. In these analyses, improved assumptions from the previous two sections are included.

While trying to incorporate the assumptions of temperature dependency in emissivity, and pressure and temperature dependency in conductivity, some problems with the ABAQUS code were encountered. To include the temperature dependency in emissivity using ABAQUS requires that the heat transfer analysis be conducted in two stages. An analysis where conductivities of the materials are only a function temperature was conducted as a first stage. The temperature results in the damaged region are then stored. In a subsequent analysis, representing the second stage, conductivities of the materials are functions of both temperature and pressure, the temperature results from the first stage are used to govern the selection of emissivity values for the calculations in the second stage. This ensures the correct emissivity data is used. This approximate method yields satisfactory results since the surface temperatures were found to be only marginally affected by the inclusion of pressure dependency on conductivity.

In the previous heat transfer analysis the out-of-plane conductivity was used. From Table 3.9, it can be seen that the in-plane conductivity used in the previous analysis is about 42% to 55% lower. Using the transversely isotropic properties with the $D = 1$" axisymmetric model, the maximum temperature results were found to be largely unaffected even though temperature distributions in the tile are slightly modified.

The results from the heat transfer analysis described above are used to determine the thermal stress. In the previous analysis, the in-plane stiffness was used for the assumed isotropic properties, thus the out-of-plane stiffness used was approximately 2.5 times higher. The maximum von Mises stresses that occur in the tile, SIP and underlying structure subjected to BC2 using isotropic and transversely isotropic properties are shown in Table 3.14. For the $D = 1$" axisymmetric case, the maximum stresses in the TPS are only slightly modified ($< 6\%$). In the undamaged case, where the heat transfer results between the isotropic and anisotropic tile analyses are the same, the thermal stress results show a much larger difference in the tile (14.2%).

Assuming an isotropic tile was found to influence the results in most cases and the changes are not all conservative. It should also be noted that von Mises stress is generally not used as a failure criterion for anisotropic materials. For this class of materials, the Hill criterion [16] is applied.

Temperature Dependent Mechanical Properties

The coefficient of thermal expansion (CTE) for the tile, and the CTE and Youngs modulus of the underlying structure are actually functions of temperature. For the underlying structure, the CTE increases with temperature while the modulus decreases. The CTE of

the LI-900 tile does not increase monotonically with temperature; instead it increases with temperatures up to about $540\,^{\circ}\mathrm{C}$, and afterwards it decreases. In the previous chapter, all mechanical properties are assumed to be constants. The room temperature CTE and modulus were used for the underlying structure. For the tile, an average value of CTE ($6.06 \times 10^{-7}/\,^{\circ}\mathrm{C}$) was used.

The maximum von Mises stresses that occur in the tile, SIP and underlying structure for the undamaged and $D = 1$" axisymmetric model subjected to BC2 for constant and temperature dependent mechanical properties are shown in Table 3.15. For the undamaged configuration, using constant mechanical properties produces lower maximum von Mises stresses in the tile and underlying structure, however, for the damaged configuration, these stresses are higher.

In the structure, the decrease in stiffness produces a decrease in maximum stresses, but this is overcome by the increase in stress due to the increase in CTE. Thus higher stresses are obtained in the analyses where mechanical properties are functions of temperature. For the damaged configuration, where the temperature reached in the structure is higher, the effects of the decreasing modulus outweigh that of the increasing CTE, so lower stresses are obtained. However, these differences are modest ($< 10\%$).

For the tile, the different CTE used, as shown in Figure 3.14, gives rise to interesting results. For the undamaged configuration, the maximum von Misses stress using constant mechanical properties is lower by 3% while the stress is higher by 80% for the damaged configuration. The maximum temperature reached in the undamaged configuration is relatively low, $980\,^{\circ}\mathrm{C}$. The maximum stress for the analysis based on constant mechanical properties is reached when the maximum temperature occurs. This is not true for the case

with temperature dependent properties. In this case, the maximum stress was reached when the maximum temperature in the tile was $540\,^{\circ}\mathrm{C}$, which corresponds to the temperature where CTE is the highest. In the damaged configuration, however, the maximum temperature in the tile is so high that the maximum stresses occur when the maximum temperature is reached, even with the reduction in CTE at these high temperatures. The high maximum temperatures also produce a large over-prediction in maximum stresses when the average constant CTE is used.

3.3.3 Thermomechanical Behavior with Improved Assumptions Based on the 3D Model and Comparison with Previous Results

The maximum temperatures that occur in the tile, SIP and underlying structure, including the times when they occur are shown in Table 3.16. Two values are provided for each damaged configuration: one for the q_1 thermal loading case (left column) and the other for the q_2 thermal loading case (right column). The percentage changes in the maximum temperatures for the damaged configurations compared to the undamaged (baseline) configuration are also provided in the tables.

The lower bound temperatures for all TPS components are relatively insensitive to the changes in the assumptions. For the upper bound temperatures, the reduction in emissivity in the damaged region raises the temperatures significantly. The effects of damage size on these temperatures are also more severe with the new assumptions. Maximum temperatures in the SIP and underlying structure also occur at earlier times.

Tables 3.17 through 3.19 provide the maximum von Mises stresses in the tile, SIP and underlying structure, together with the times at which they occur for both thermal load-

ing cases using the improved assumptions. In the tables, two maximum stresses, one for the unrestrained boundary condition, BC1, and one for the restrained boundary condition, BC2, are provided. The percentage changes in these stresses in the damaged configurations, with respect to the baseline configuration, are also indicated.

For the lower bound loading case, the maximum stresses in the tile from the improved and previous sets of results are quite similar. The maximum difference between the two sets of results is approximately -5.5%. For the upper bound loading case, the differences are larger. The higher temperatures in the tile as a result of the new assumptions did not produce higher maximum stresses. The maximum stresses are actually lower due to the lower CTE used. The differences in the results are between 13% and 44%.

In the SIP, maximum stresses using the new assumptions are higher in the BC1 cases while that for the BC2 cases are generally lower. The differences in results vary between -51% and 50%. These differences are due to a combination of higher temperatures and the larger CTE mismatch between the tile and the underlying structure.

With the new assumptions, the maximum stresses in the underlying structure for the BC1 cases are generally lower while those for the BC2 cases are all higher. Differences in these results are between -36% and 26%. The higher temperatures and the changing CTE and stiffness of the underlying structure with respect to temperature are the primary causes of the differences.

It is evident that the simplifying assumptions used in the previous chapter produced results that have substantial errors. For the TPS considered, which include three very dissimilar materials operating under a wide range of temperatures and pressures, these simplifying assumptions were found to affect the accuracy of the results in a fairly complicated

manner. It is not possible to choose simplifying assumptions that guarantee conservative results for both heat transfer and thermal stress analysis. Therefore, it is important to use the refined models that incorporate realistic assumptions. The simplifying assumptions should be avoided.

3.3.4 Effects of Damage Location

Using a damage size of $D = 1$" and the 3D model with q_2 thermal loading, the maximum temperatures reached in each TPS component for each value of δ, representing different damage locations is presented in Table 3.20. The maximum temperature in the tile increases by only 4.4% with increasing damage offset distance from the center. This is probably due to the insulated boundary condition on the side of the TPS. The maximum temperatures in the SIP and structure were found to remain almost unchanged. Thus, for the cases considered, the results indicate that the maximum temperatures in the TPS remain practically unchanged.

The maximum von Mises stresses that occur in the tile, SIP and underlying structure are shown in Table 3.21. For the BC1 case, the stress in the tile was found to decrease by up to 5.9% when damage was displaced from the center. For the BC2 case, the stress in the tile was found to decrease by up to 21.3%. For the SIP and underlying structure, the changes in stresses are very small ($< 3.5\%$).

These results indicate that damage location has a minor influence on the SIP and underlying structure, but is more significant for the tile. Note,however, that the results for $\delta = 0$" are the most severe. This implies that central damage appears to be the worst-case, therefore only this damage location will be used in the calculations that are presented in

the rest of the disssertation.

TPS Element	*D* (inch)	Temperature (°C)		% change		Time (s)	
Tile	0	981		NA		850	
	0.5	981	1457	0	48.5	850	850
	1.0	981	1499	0	52.8	850	850
	1.5	981	1515	0	54.4	850	850
SIP	0	150		NA		6600	
	0.5	149	156	-0.7	4.0	6550	6550
	1.0	145	180	-3.3	20.0	6450	6300
	1.5	139	225	-7.3	50.0	6250	5800
Underlying structure	0	150		NA		7150	
	0.5	148	156	-1.3	4.0	7150	7100
	1.0	144	179	-4.0	19.3	7100	6850
	1.5	138	224	-8.0	49.3	6900	6300

Table 3.1: Maximum temperatures and times at which they occur in the tile, SIP and underlying structure in 3D models

Thermal Loading	*D* (inch)	Max. von Mises stress (kPa)		% change		Time (s)	
		BC1	BC2	BC1	BC2	BC1	BC2
q_1	0	63.4	63.6	NA	NA	350	350
	0.5	111.2	111.6	75.4	75.5	350	350
	1.0	99.5	99.9	56.9	57.1	400	400
	1.5	96.4	96.8	52.1	52.2	400	400
q_2	0	63.4	63.6	NA	NA	350	350
	0.5	138.1	138.3	117.8	117.5	400	400
	1.0	136.8	137.1	115.8	115.6	400	400
	1.5	149.9	150.0	136.4	135.8	400	400

Table 3.2: Maximum von Mises stresses and times at which they occur in tile for the 3D models at t1 for the two different thermal loading conditions

Thermal Loading	*D* (inch)	Max. von Mises stress (kPa)	% change	Time (s)
q_1	0	75.0	NA	7100
	0.5	71.3	-4.9	7100
	1.0	68.9	-8.1	7050
	1.5	65.5	-12.7	6850
q_2	0	75.0	NA	7100
	0.5	75.6	0.8	7100
	1.0	88.6	18.1	6750
	1.5	113.5	51.3	6250

Table 3.3: Maximum von Mises stresses and times at which they occur in tile for the 3D models at t2 for the two different thermal loading conditions

Thermal Loading	*D* (inch)	Max. von Mises stress (kPa)		% change		Time (s)	
		BC1	BC2	BC1	BC2	BC1	BC2
q_1	0	30.1	4.61	NA	NA	7150	6050
	0.5	30.0	4.31	-0.3	-6.5	7250	5600
	1.0	29.0	4.20	-3.7	-8.9	7200	5450
	1.5	27.6	3.94	-8.3	-14.5	7000	5150
q_2	0	30.1	4.61	NA	NA	7150	6050
	0.5	31.8	4.65	5.6	0.9	7200	5900
	1.0	37.3	5.45	23.9	18.2	6800	5700
	1.5	47.7	6.99	58.5	51.6	6350	5250

Table 3.4: Maximum von Mises stresses and times at which they occur in SIP for the 3D models for the two different thermal loading conditions

Thermal Loading	*D* (inch)	Max. von Mises stress (MPa)		% change		Time (s)	
		BC1	BC2	BC1	BC2	BC1	BC2
q_1	0	2.32	283.1	NA	NA	7300	7150
	0.5	2.34	277.9	0.8	-1.8	7300	7150
	1.0	2.26	268.6	-2.6	-5.1	7250	7100
	1.5	2.16	255.5	-6.9	-9.7	7100	6900
q_2	0	2.32	283.1	NA	NA	7300	7150
	0.5	2.48	294.6	6.9	4.1	7300	7100
	1.0	2.91	345.5	25.4	22.0	6900	6850
	1.5	3.73	442.3	60.8	56.2	6450	6300

Table 3.5: Maximum von Mises stresses and times at which they occur in underlying structure for the 3D models for the two different thermal loading conditions

T (°C)	**c (J/kg °C)**	**k (W/m °C)**	**E (GPa)**	**α (10^{-6}/°C)**
-73.2	787.0	163.0	–	–
-17.8	–	–	–	21.9
21.0	–	–	72.4	–
26.9	875.0	177.0	–	–
37.8	–	–	72.0	22.6
93.3	–	–	70.4	23.2
126.9	925.0	186.0	–	–
148.9	–	–	68.5	23.6
204.4	–	–	64.3	24.0
260.0	–	–	57.3	24.4
315.6	–	–	50.5	24.9
326.9	1042.0	–	–	–
371.1	–	–	–	25.4
426.7	–	–	–	26.0
482.2	–	–	–	26.7

ρ = 2770 kg/m^3
ν = 0.33

Table 3.6: Material properties of the underlying structure (Aluminum 2024)

	P (Pa)				
T (°C)	10.133	101.33	1013.3	10133	101330
-17.6	0.009173	0.01904	0.03081	0.03427	0.03548
38.0	0.009865	0.02146	0.03600	0.04067	0.04223
93.5	0.01090	0.02337	0.04154	0.04725	0.04933
149.1	0.01263	0.02631	0.04708	0.05504	0.05711
204.6	0.01575	0.02908	0.05244	0.06421	0.06611
315.7	0.02077	0.03548	0.06750	0.08308	0.08533
426.9	0.02700	0.04327	0.08654	0.1052	0.1073

Table 3.7: Conductivity of SIP (W/m-°C) with respect to temperature and pressure

T (°C)	**c (J/kg °C)**	α **(10^{-6}/°C)**
-17.6	628.0	0.405
121.3	879.2	0.540
260.2	1055.1	0.648
399.1	1151.4	0.720
538.0	1205.8	0.792
676.9	1239.3	0.576
815.7	1256.0	0.480
926.9	1264.4	0.432
954.6	1268.6	–
1093.5	–	0.360

ρ	=	144	kg/m^3
E_x, E_z	=	172.4	MPa
E_y	=	48.3	MPa
G_{xy}, G_{yz}	=	20.7	MPa
G_{xz}	=	72.4	MPa
ν_{xy}	=	0.16	
ν_{xz}	=	0.18	
ν_{yz}	=	0.04	

Table 3.8: Material properties of SIP

	P (Pa)				
T (°C)	10.133	101.33	1013.3	10133	101330
-17.6	0.02597 (0.01298)	0.03116 (0.01731)	0.04847 (0.03168)	0.05712 (0.04328)	0.06751 (0.04760)
121.3	0.03462 (0.01593)	0.03981 (0.02164)	0.05712 (0.03895)	0.07097 (0.05470)	0.08136 (0.05903)
260.2	0.04501 (0.02164)	0.05193 (0.02891)	0.07270 (0.04778)	0.08828 (0.06924)	0.09867 (0.07495)
399.1	0.06059 (0.03029)	0.06924 (0.3739)	0.08828 (0.05626)	0.1108 (0.08517)	0.1212 (0.09244)
538.0	0.08482 (0.04033)	0.09001 (0.04760)	0.1091 (0.06786)	0.1402 (0.1039)	0.1523 (0.1139)
676.9	0.1142 (0.05331)	0.1229 (0.06059)	0.1437 (0.08517)	0.1800 (0.1255)	0.1921 (0.1354)
815.7	0.1541 (0.07201)	0.1662 (0.07945)	0.1887 (0.1068)	0.2285 (0.1515)	0.2423 (0.1631)
954.6	0.2060 (0.09815)	0.2164 (0.1056)	0.2423 (0.1328)	0.2891 (0.1835)	0.3029 (0.1956)
1093.5	0.2648 (0.1271)	0.2804 (0.1354)	0.3116 (0.1631)	0.3670 (0.2198)	0.3826 (0.2354)
1260.2	0.3687 (0.1672)	0.3826 (0.1766)	0.4154 (0.2008)	0.4726 (0.2683)	0.4985 (0.2891)
1371.3	– (0.2008)	– (0.2129)	– (0.2406)	– (0.3098)	– (0.3358)
1538.0	– (0.2666)	– (0.2804)	– (0.3116)	– (0.3843)	– (0.4189)
1649.1	– (0.3289)	– (0.3393)	– (0.3791)	– (0.4535)	– (0.5020)

Table 3.9: Conductivity of LI-900 tile (W/m-°C) with respect to temperature and pressure

T (°C)	**c (J/kg °C)**	α **(10^{-6}/°C)**
-17.6	628.0	0.405
121.3	879.2	0.540
260.2	1055.1	0.648
399.1	1151.4	0.720
538.0	1205.8	0.792
676.9	1239.3	0.576
815.7	1256.0	0.480
926.9	1264.4	0.432
954.6	1268.6	–
1093.5	–	0.360

ρ	=	194	kg/m^3
E_x, E_z	=	172.4	MPa
E_y	=	48.3	MPa
G_{xy}, G_{yz}	=	20.7	MPa
G_{xz}	=	72.4	MPa
ν_{xy}	=	0.16	
ν_{xz}	=	0.18	
ν_{yz}	=	0.04	

Table 3.10: Material properties of LI-900 tile

Temperature (°C)	Emissivity of Uncoated LI-900 Tile
27	0.88050
127	0.83613
227	0.76578
327	0.68410
427	0.60390
527	0.53177
627	0.46981
727	0.41785
827	0.37477
927	0.33918
1027	0.30980
1127	0.28548
1227	0.26527
1327	0.24841

Table 3.11: Emissivity (ε) of uncoated tile with respect to temperature

TPS Component	Max. temperatures with constant emissivity (°C)	Max. temperature with emissivity as function of temperature (°C)
LI-900	1501	2178
SIP	188.1	228.9
Structure	187.3	228.1

Table 3.12: Maximum temperature results for $D = 1$" axisymmetric model for analysis with or without temperature dependent emissivity

TPS Component	Max. von Mises stress with $k = f(T)$ (Pa)	Max. von Mises stress with $k = g(T, P)$ (Pa)
LI-900	6.20×10^4	7.17×10^4
SIP	4.03×10^3	2.86×10^3
Structure	2.81×10^8	2.80×10^8

Table 3.13: Maximum von Mises stresses attained for each TPS component with or without pressure dependency in conductivity

D	TPS Component	Max. von Mises stress with isotropic properties (Pa)	Max. von Mises stress with transversely isotropic properties (Pa)
0”	LI-900	7.17×10^4	6.15×10^4
	SIP	2.86×10^3	2.83×10^3
	Structure	2.80×10^8	2.79×10^8
1”	LI-900	2.11×10^5	2.09×10^5
	SIP	5.15×10^3	5.41×10^3
	Structure	5.04×10^8	5.34×10^8

Table 3.14: Maximum von Mises stresses attained for analysis using isotropic or transversely isotropic material properties

D	TPS Component	Max. von Mises stress with constant mechanical properties (Pa)	Max. von Mises stress with mechanical properties as function of temperature (Pa)
0”	LI-900	6.15×10^4	6.34×10^4
	SIP	2.83×10^3	2.83×10^3
	Structure	2.79×10^8	3.09×10^8
1”	LI-900	2.09×10^5	1.16×10^5
	SIP	5.41×10^3	5.46×10^3
	Structure	5.34×10^8	5.05×10^8

Table 3.15: Maximum von Mises stresses attained for each TPS component with constant or temperature-dependent material properties

TPS component	*D* (inch)	Temperature (°C)		% change		Time (s)	
Tile	0	981		NA		850	
	0.5	981	1846	0	88.2	850	850
	1.0	981	2048	0	108.8	850	850
	1.5	981	2133	0	117.4	850	850
SIP	0	150		NA		5000	
	0.5	148	167	-1.3	11.3	5000	4900
	1.0	145	242	-3.3	61.3	4900	4550
	1.5	140	382	-6.7	154.7	4750	3900
Underlying structure	0	150		NA		5450	
	0.5	148	166	-1.3	10.7	5450	5350
	1.0	144	241	-4.0	60.7	5400	4950
	1.5	139	380	-7.3	153.3	5300	4200

Table 3.16: Maximum temperature results for 3D models using improved assumptions

Thermal Loading	*D* (inch)	Max. von Mises stress (kPa)		% change		Time (s)	
		BC1	BC2	BC1	BC2	BC1	BC2
q_1	0	64.9	65.0	NA	NA	200	200
	0.5	111.7	112.0	72.1	72.3	250	250
	1.0	105.3	105.5	62.2	62.3	250	250
	1.5	96.3	96.5	48.4	48.5	250	250
q_2	0	64.9	65.0	NA	NA	200	200
	0.5	96.4	96.6	48.5	48.6	400	400
	1.0	119.1	119.3	83.5	83.5	400	400
	1.5	132.2	132.4	103.7	103.7	400	400

Table 3.17: Maximum von Mises stresses and times at which they occur in tile for the 3D models using improved assumptions

Thermal Loading	*D* (inch)	Max. von Mises stress (kPa)		% change		Time (s)	
		BC1	BC2	BC1	BC2	BC1	BC2
q_1	0	32.2	3.08	NA	NA	5450	5500
	0.5	31.9	3.05	-0.9	-1.0	5450	5500
	1.0	30.9	2.96	-4.0	-3.9	5400	5450
	1.5	29.5	2.85	-8.4	-7.5	5300	5350
q_2	0	32.2	3.08	NA	NA	5450	5500
	0.5	36.8	3.51	14.3	14.0	5350	5400
	1.0	56.7	5.38	76.1	74.7	4950	5000
	1.5	96.7	8.89	200.3	188.6	4200	4250

Table 3.18: Maximum von Mises stresses and times at which they occur in SIP for the 3D models using improved assumptions

Thermal Loading	*D* (inch)	Max. von Mises stress (MPa)		% change		Time (s)	
		BC1	BC2	BC1	BC2	BC1	BC2
q_1	0	1.86	308.9	NA	NA	5550	5450
	0.5	1.84	305.9	-1.1	-1.0	5550	5450
	1.0	1.79	297.0	-3.8	-3.9	5500	5400
	1.5	1.72	284.9	-7.5	-7.8	5400	5300
q_2	0	1.86	308.9	NA	NA	5550	5450
	0.5	2.11	347.0	13.4	12.3	5450	5350
	1.0	3.09	476.5	66.1	54.3	5050	4950
	1.5	4.88	688.8	162.4	123.0	4250	4200

Table 3.19: Maximum von Mises stresses and times at which they occur in underlying structure for the 3D models using improved assumptions

TPS Component	Max. temperatures with δ = 0" (°C)	Max. temperatures with δ = 1" (°C)	Max. temperature with δ = 2" (°C)
LI-900	2048	2080	2100
SIP	242	244	241
Structure	241	241	237

Table 3.20: Maximum temperatures attained for each TPS component for different δ with q_2 thermal loading

Structural BC	TPS Component	Max. von Mises Stress with δ = 0" (Pa)	Max. von Mises Stress with δ = 1" (Pa)	Max. von Mises Stress with δ = 2" (Pa)
BC1	**LI-900**	1.19×10^5	1.12×10^5	1.14×10^5
	SIP	2.96×10^3	2.96×10^3	2.96×10^3
	Structure	2.97×10^8	2.98×10^8	2.98×10^8
BC2	**LI-900**	1.19×10^5	1.14×10^5	9.37×10^4
	SIP	5.38×10^3	5.37×10^3	5.27×10^3
	Structure	4.77×10^8	4.76×10^8	4.71×10^8

Table 3.21: Maximum vom Mises stresses attained for each TPS component for BC1 and BC2 boundary conditions

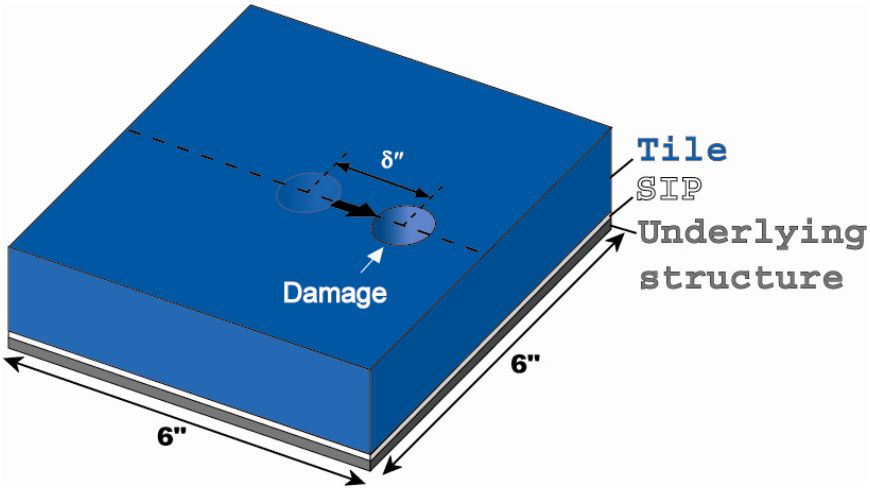

Figure 3.1: Schematic of 3D model illustrating the change in location of damage from center

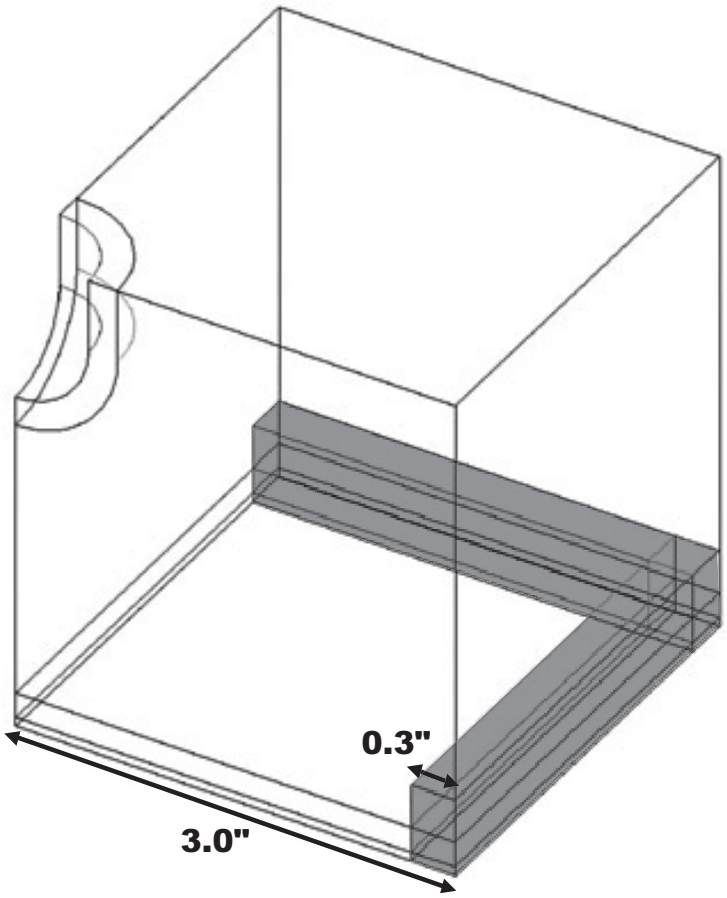

Figure 3.2: Illustration the boundary layer region in 3D model

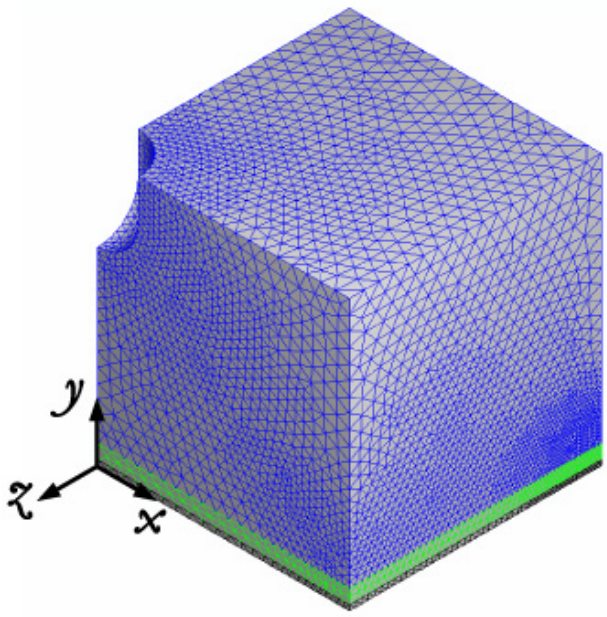

(a) 3D model with $\delta = 0$"

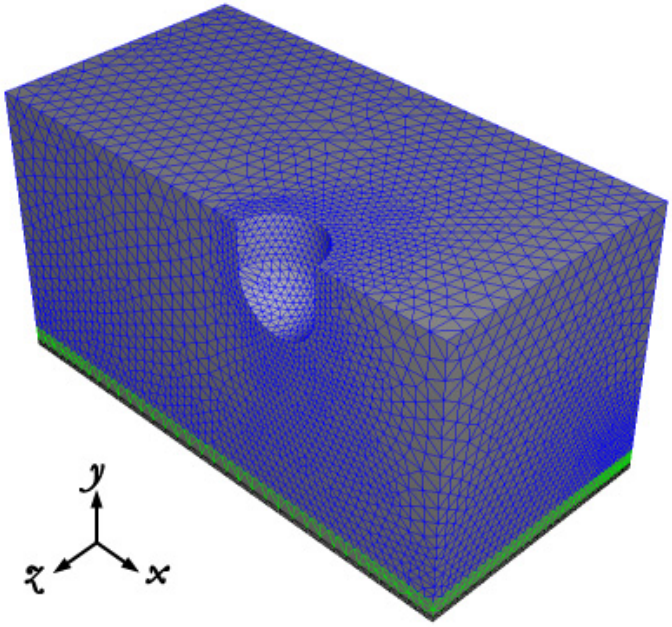

(b) 3D model with $\delta = 1$"

Figure 3.3: FE meshes for 3D models with $D = 1$" damage

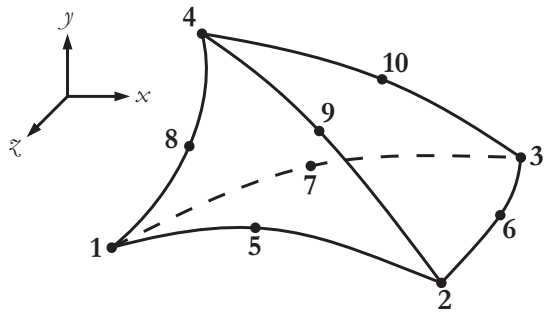

Figure 3.4: 10-node quadratic tetrahedron element used for 3D model

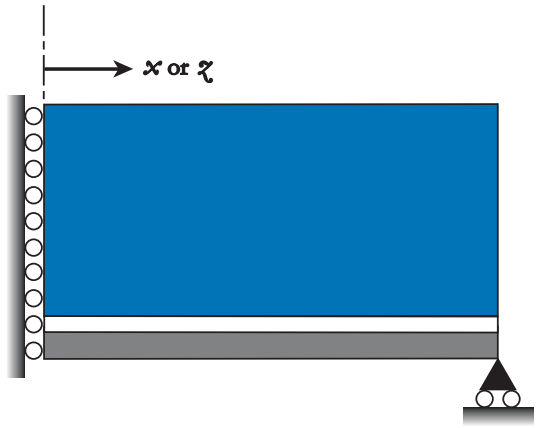

(a) unrestrained boundary condition, BC1

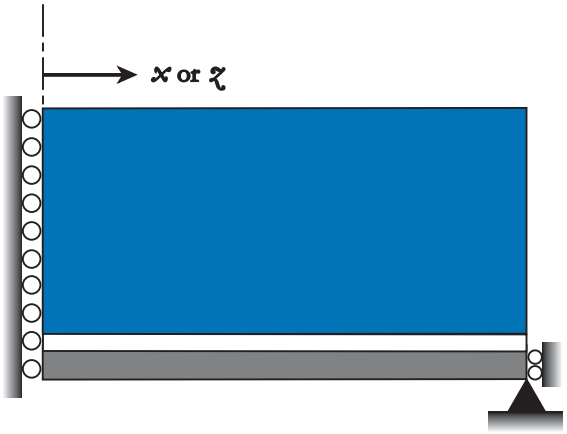

(b) restrained boundary condition, BC2

Figure 3.5: Structural boundary conditions applied to underlying structure

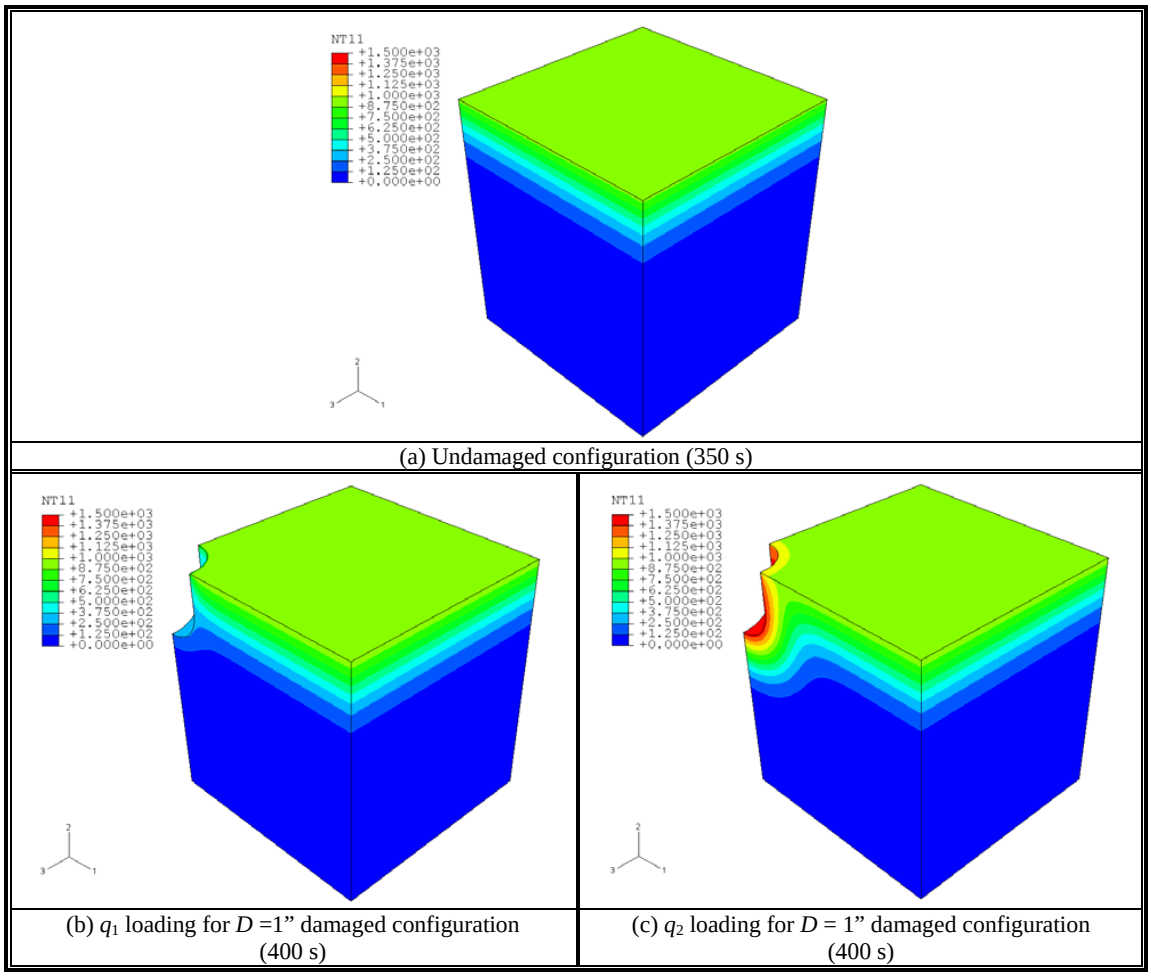

(a) Undamaged configuration (350 s)

(b) q_1 loading for D =1" damaged configuration (400 s)

(c) q_2 loading for D = 1" damaged configuration (400 s)

Figure 3.6: Temperature contour plots for the undamaged and damaged (D = 1″) 3D models for the two different heat loads at times when the maximum von Mises stress in tile occurs. Legends indicate temperatures in °C

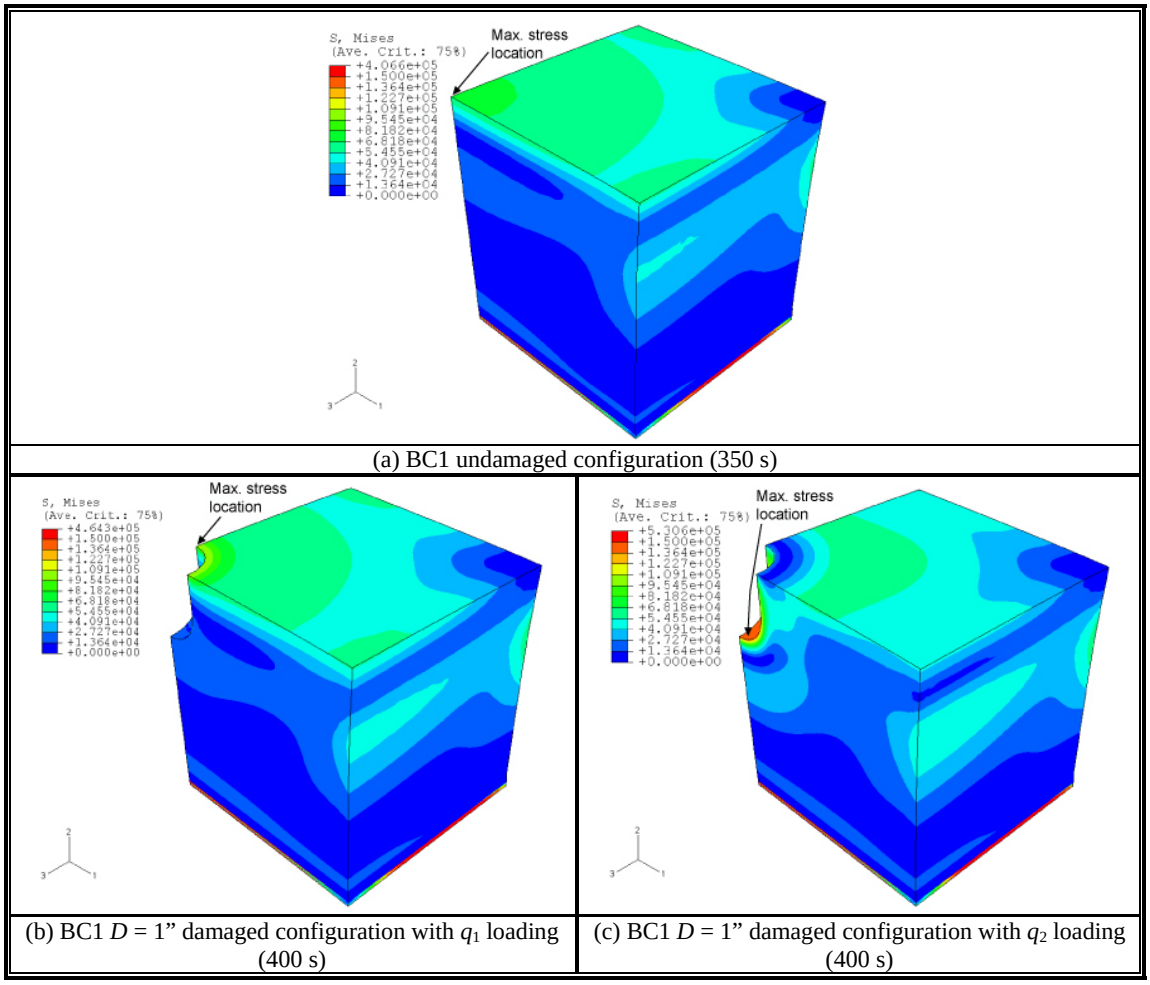

Figure 3.7: von Mises stress contour plots for the undamaged and D = 1″ damaged 3D models for the two different heat loads at times when the maximum von Mises stress in tile occurs. Legends indicate stresses in Pascal

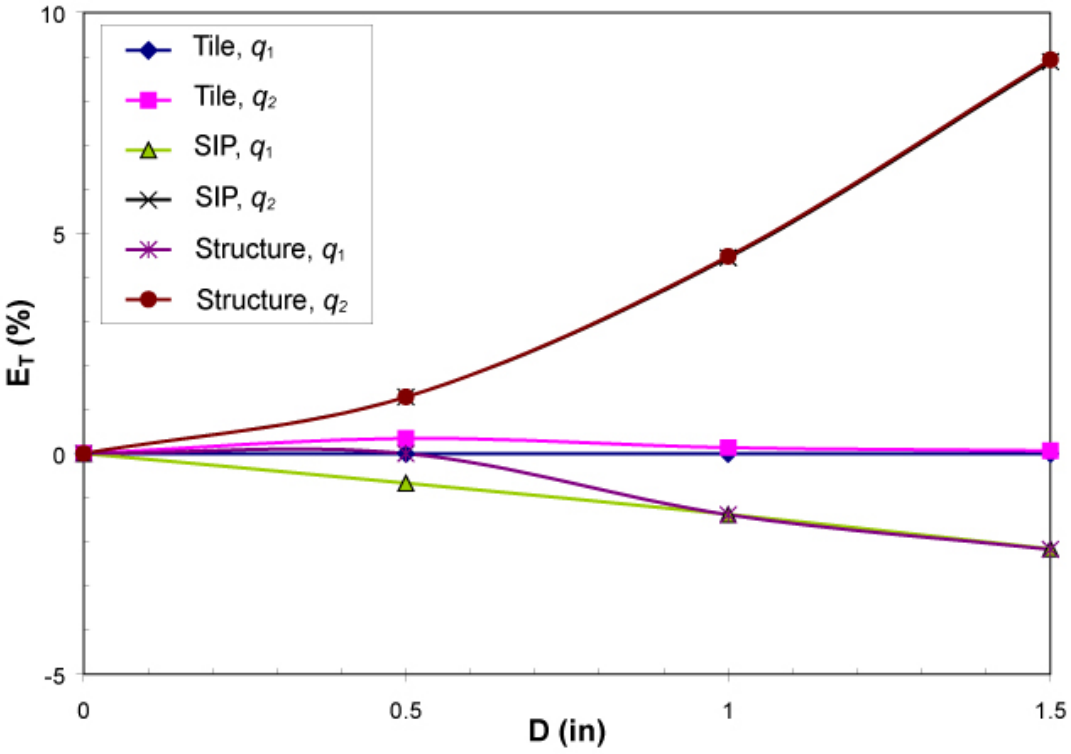

Figure 3.8: Comparison of maximum temperatures for axisymmetric and 3D models

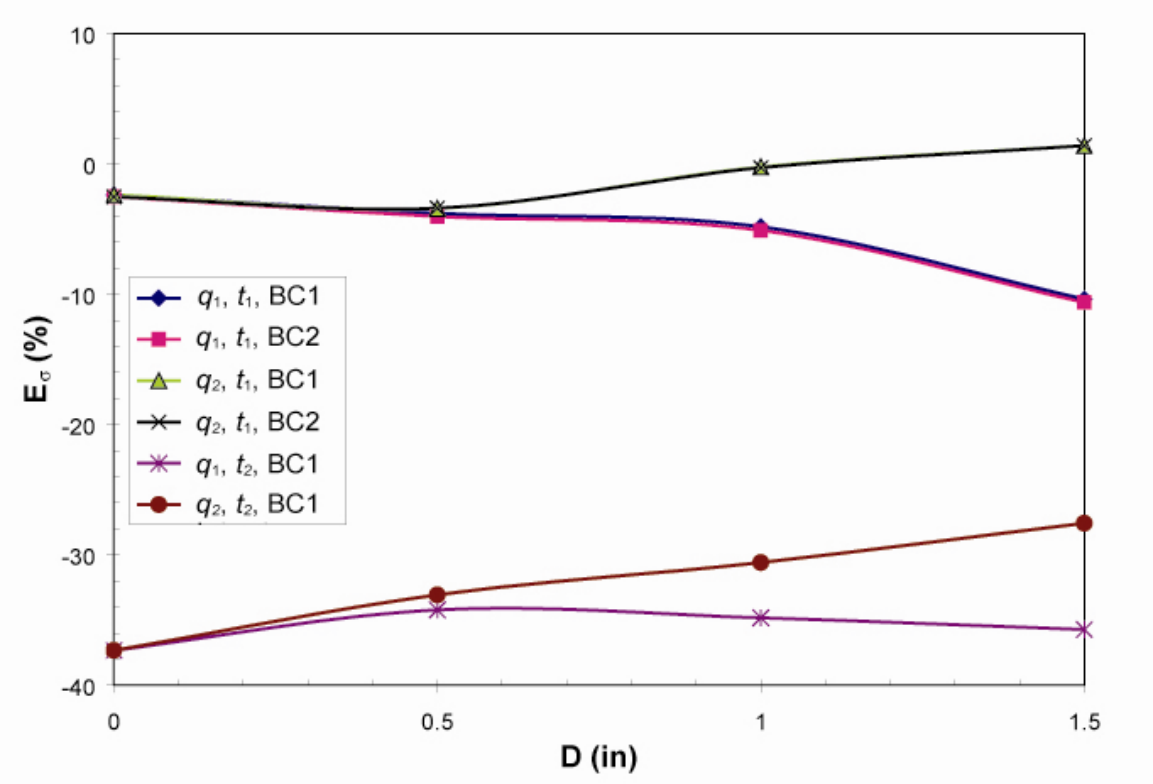

Figure 3.9: Comparison of maximum von Mises stresses in the tile for axisymmetric and 3D models

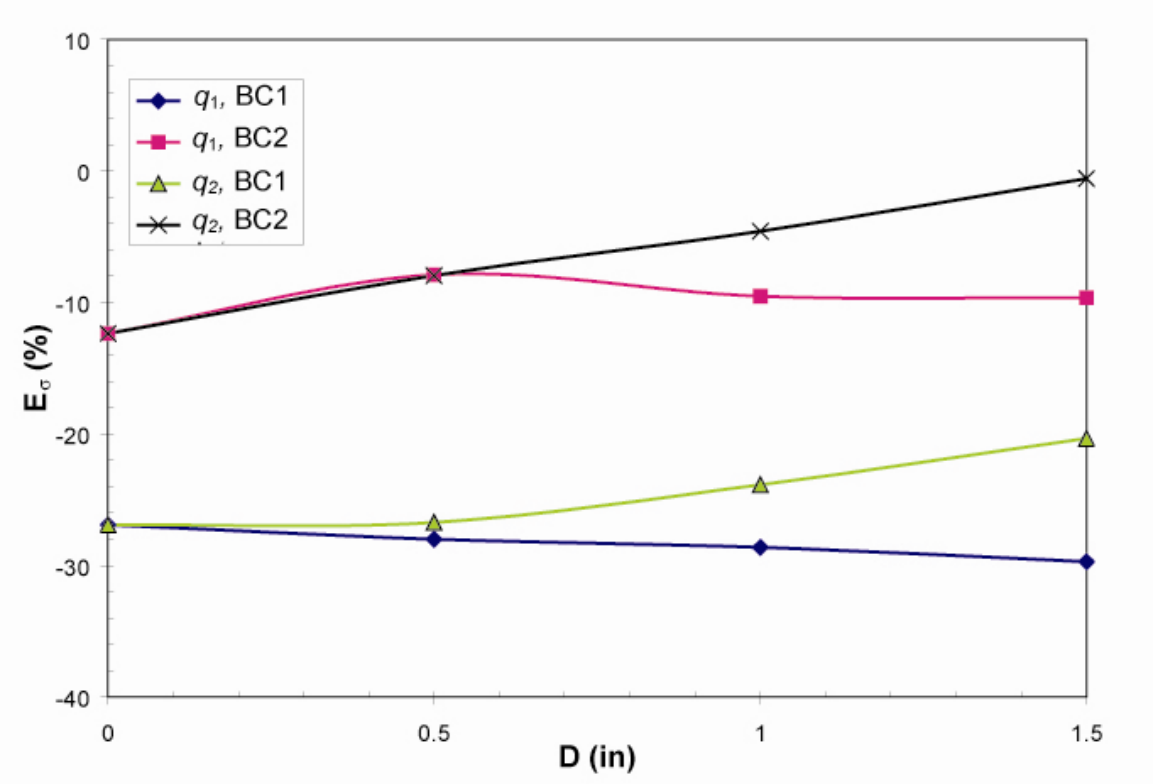

Figure 3.10: Comparison of maximum von Mises stresses in the SIP for axisymmetric and 3D models

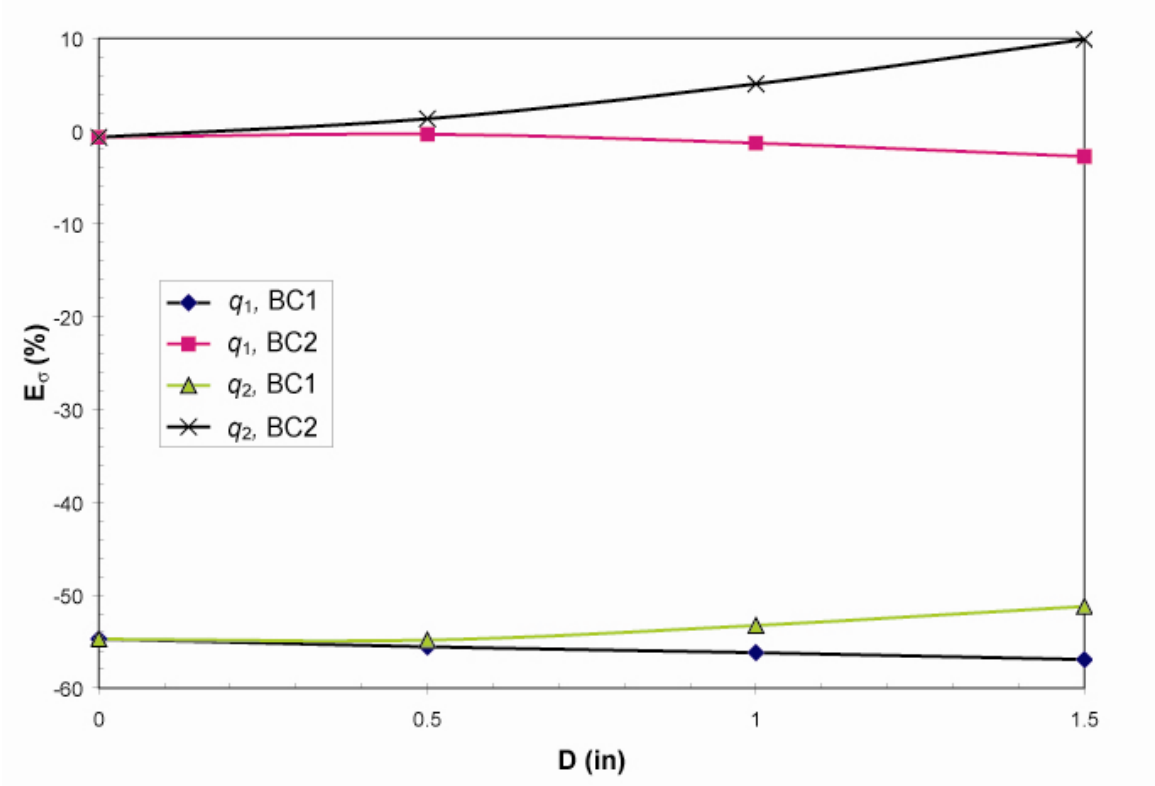

Figure 3.11: Comparison of maximum von Mises stresses in underlying structure for axisymmetric and 3D models

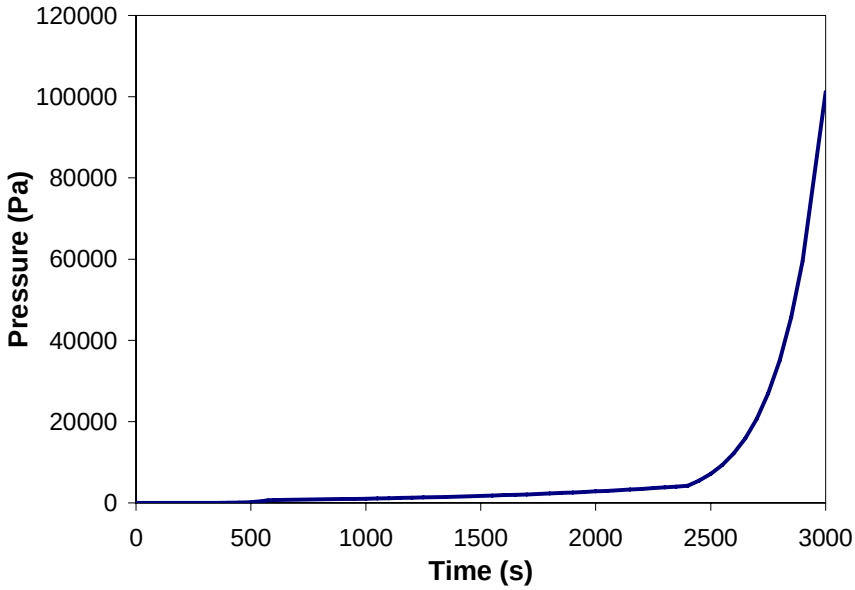

Figure 3.12: ATS vehicle operating pressure profile

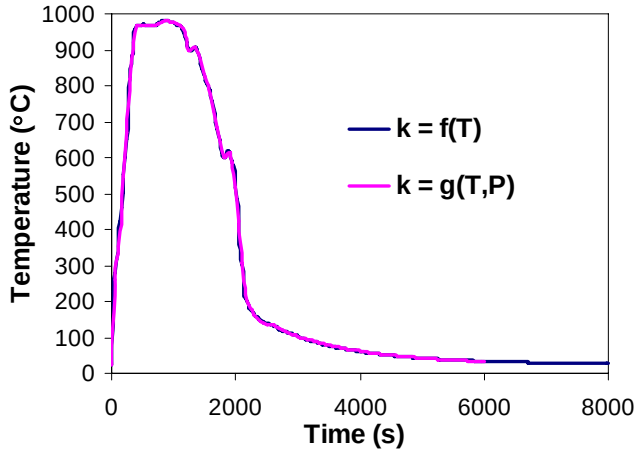

(a) Surface of tile

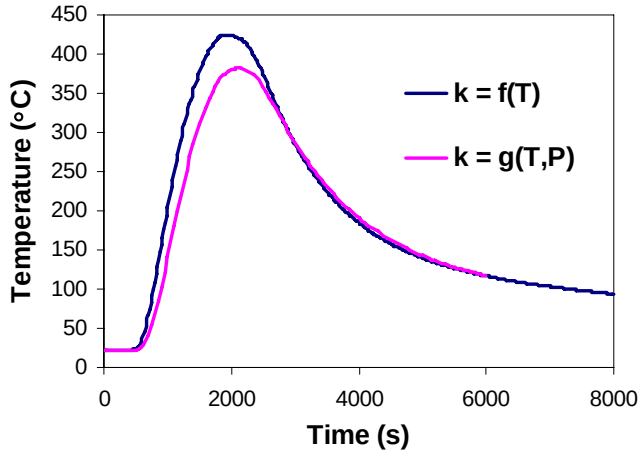

(b) Middle of tile

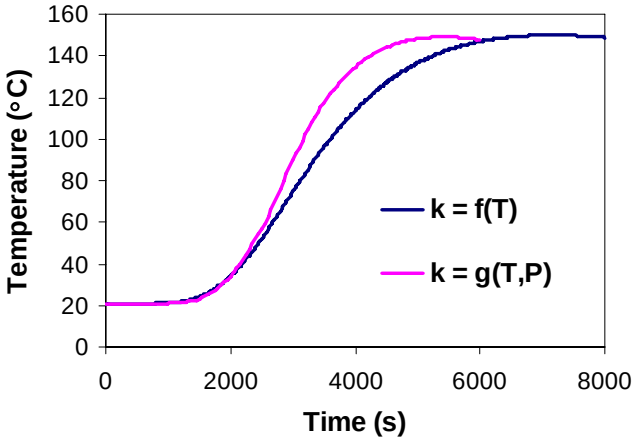

(c) Underlying structure

Figure 3.13: Transient temperature results at the surface and middle of the tile and at underlying structure for analyses with and without pressure dependent conductivity

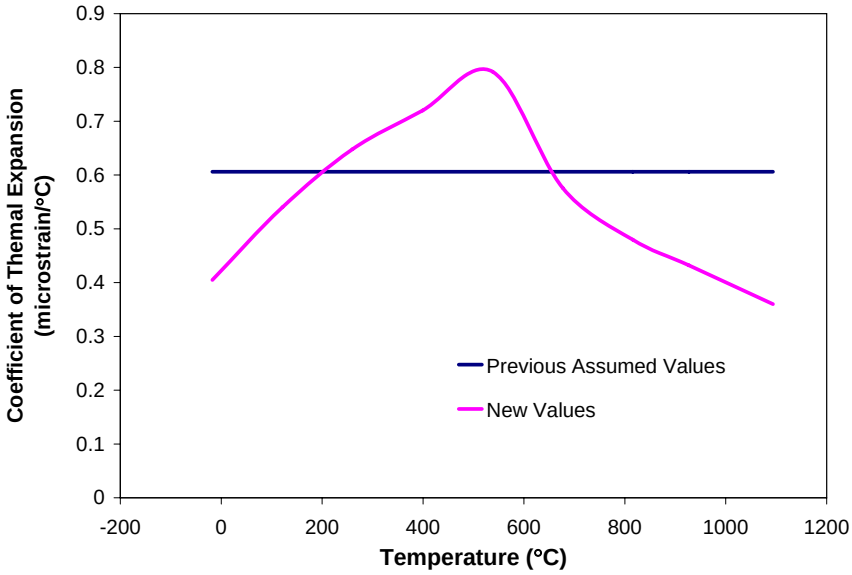

Figure 3.14: Previous and new values of CTE with respect to temperature

CHAPTER IV

DEVELOPMENT OF A THERMAL STRUCTURES TEST FACILITY AND ITS CALIBRATION

A new facility for high temperature structures testing was designed and developed in order to carry out experiments on undamaged and damaged HRSI tiles. The facility resembles to some extent a test chamber that exists at NASA Langley [9]. The laboratory and its calibration are described in this chapter.

4.1 Design Requirements

The goal of the laboratory is to carry out experiments to be conducted on TPS. The objective is to obtain temperature and strain measurements that goven the thermal and structural behavior for undamaged and damaged TPS.

As mentioned earlier, the function of the TPS is to protect the underlying structure against high temperatures due to aerodynamic heating on the exposed surface of the TPS during re-entry. For most high temperature insulation materials used in TPS, their conductivities are also functions of pressure due to material porosity. Thus, the performance for thermal protection is dependent on changes in pressures during re-entry. The precise

re-entry conditions for testing TPS are difficult to duplicate. An alternative is to apply a transient temperature boundary condition that approximates the temperatures experienced during re-entry to the surface of the TPS test specimen, while simulating re-entry static pressure in a vacuum chamber.

An approximate re-entry temperature profile based on the ATS heating rates can be obtained from FE analysis conducted in previous chapters. This re-entry temperature profile and its associated pressure profile are shown in Figure 4.1. Due to the large heat fluxes and fast thermal rates required to simulate the temperature profile, radiant heaters are the most suitable heat source for the following reasons: (i) they have fast temperature response times, (ii) they offer uniform heat fluxes and thus uniform temperature distribution over 80% of their length, and (iii) they have been proven effective in previous TPS testing.

In order to simulate re-entry pressures, the experiments have to be conducted in a vacuum chamber. This also allows an inert environment to prevent sensors (strain gages and thermocouples) degradation at high temperatures.

4.2 Test Facility

The facility constructed is shown in Figure 4.2. It consists of the vacuum chamber, pressure control system, radiant heater system, and data acquisition system.

The cylindrical steel vacuum chamber has a diameter of 33.5" and a length of 37". The chamber is equipped with feed-through for power, gas, and instrumentation for 20 pairs of type K thermocouples and 12 pairs of strain gages. A vacuum of 40 millitorrs can be achieved when equipped with a 24 cfm dual-stage rotary vacuum pump. Nitrogen is bled into the chamber at a controlled rate to simulate re-entry pressures. This is done using

the MKS Instruments type 244/245 control system which includes a control module and a servo-controlled valve. The system has closed-loop feedback using pressure readings from two capacitance manometers which cover a range of pressure from 1 millitorr to 760 torr.

The radiant heater is a high energy electric infrared heater system manufactured by Innovative Industries, which has also provided a similar unit to NASA. The system uses a quartz lamp radiant heating array capable of rapid changes in heating that is needed for simulating transient re-entry temperatures. The 15" by 16" heating array can achieve uniform heating on the surface of a specimen having a maximum dimensions of 12" by 12". The system includes a temperature controller, which allows the user to govern the time-dependent temperature profile during the experiments.

The data acquisition system consists of two PCI-6259 data acquisition cards, manufactured by National Instruments. The two cards allow a total of 32 analog inputs for thermocouple and strain measurements and 8 analog outputs to specify the target pressure and temperature profiles to the pressure and heater controller respectively. A program written in LabVIEW [29] was used to synchronize the inputs and outputs to ensure accurate re-entry temperature and pressure simulation. The program also ensures seamless switching between the two manometers in the pressure control system.

4.3 Calibration Tests

Calibration tests were conducted to determine and fine-tune the overall performance of the laboratory. The calibration test specimen consist of a LI-900 HRSI tile instrumented with four type-K Nextel-insulated thermocouples (XC-24-K-30, Omega Engineering) as shown in Figure 4.3. One of the thermocouples, designated Ts indicated in Figure 4.3, is

used for feedback control for the radiant heater system. Due to the smooth surface of the RCG coating of the tile and the high temperatures reached during experiments, special ceramic adhesive had to be used to connect the thermocouple to the specimen. In the tests, it was determined that the best adhesive is the Omegabond-600 ceramic adhesive from Omega Engineering.

The instrumented specimen was placed on top of a steel platform that was lined with cerachem blanket, which is an alumina-silica-zirconia fiber based insulation manufactured by Thermal Ceramics. The sides of the specimen were also covered with cerachem blankets, leaving only the top surface exposed. The platform was placed underneath the radiant heater, which is suspended from the ceiling of the vacuum chamber as shown in Figure 4.4.

4.4 Calibration Results

A series of calibration tests were conducted and the final results are presented here. The pressures measured during experiment are compared with the target re-entry pressure profile shown in Figure 4.5. Due to the limitations of the pressure control system, there are considerable differences between the measured and target profiles for the first 500 seconds. Subsequently, the average difference between measured and target pressure is less than 2%. The average difference is defined as

$$\frac{1}{n}\sum_{i=1}^{n}\left|\frac{G_i - H_i}{H_i}\right| \cdot 100\% \tag{4.1}$$

where G_i and H_i are data points in the profiles being compared and n is number of data points.

Figure 4.6 shows the temperatures measured on the top surface at three different locations on the specimen as well as the target re-entry temperature profile. Using the center thermocouple, T1 in Figure 4.3, it is evident that temperature measured matches the target temperatures, with an average difference of 2.2% in the initial $2,000$ seconds. Beyond that, the rapid drop in target temperature cannot be simulated without active cooling, a feature that is not available in the current test facility. From Figure 4.6, it is evident that the temperature uniformity on the surface of the specimen is very good up to $3,000$ seconds. Subsequently, temperatures at the edge of the specimen diverge from the value at the center.

The results indicate that the laboratory could not simulate the re-entry temperature and pressure perfectly. However, the difference between target and simulated values was small and results generated are useful for FE model validation.

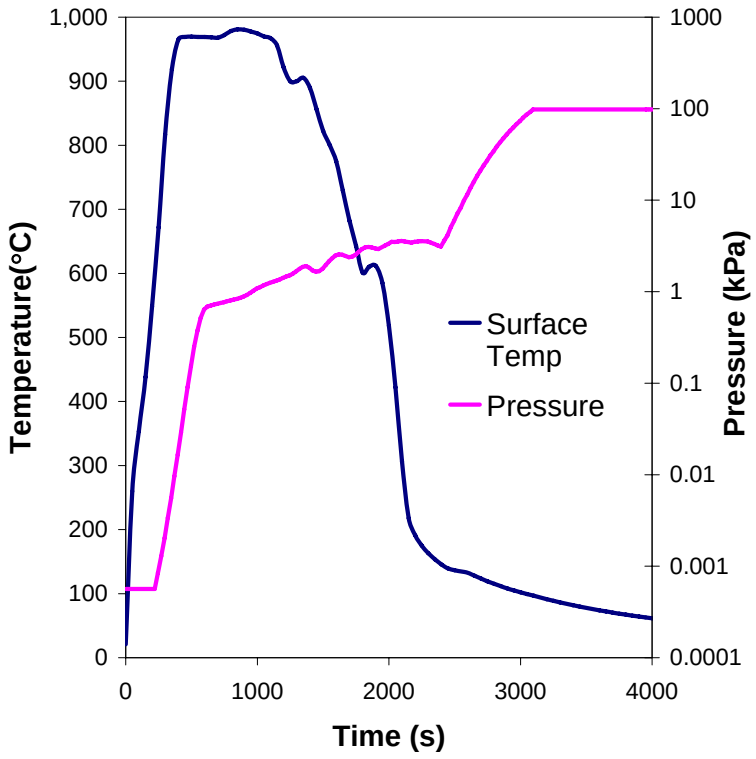

Figure 4.1: Re-entry temperature and pressure profiles of ATS vehicle

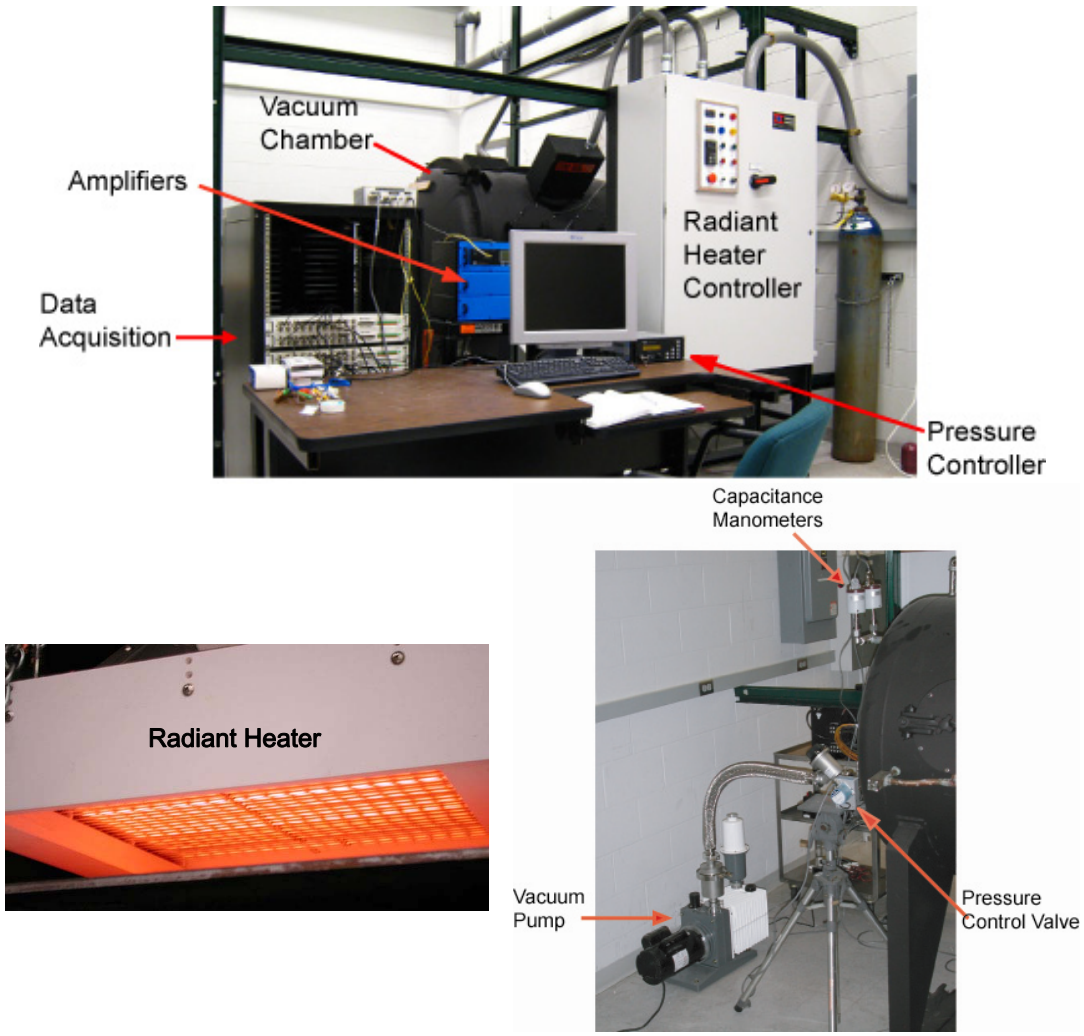

Figure 4.2: Overview of High Temperature Thermal Structures Testing Laboratory

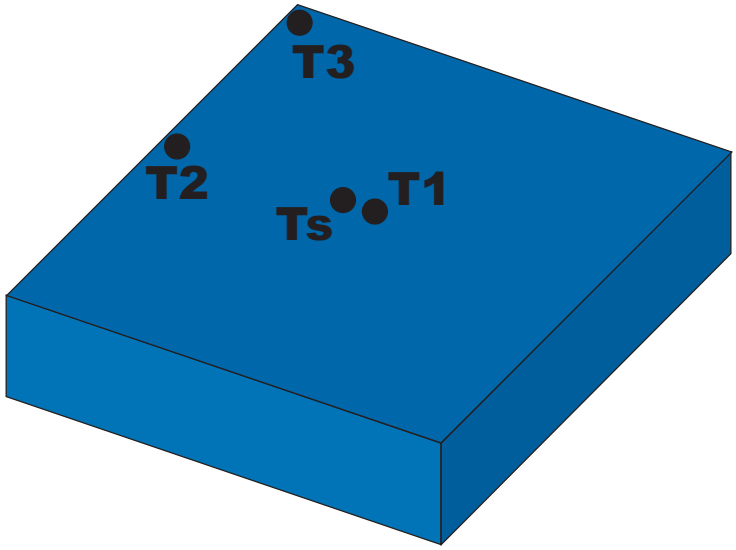

Figure 4.3: Location of thermocouples on calibration specimen

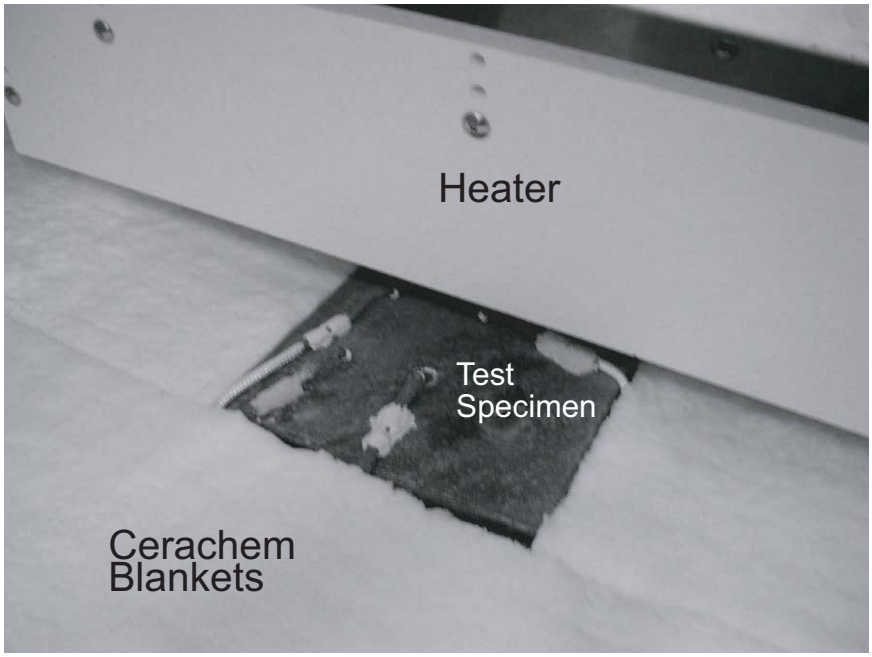

Figure 4.4: Calibration test setup

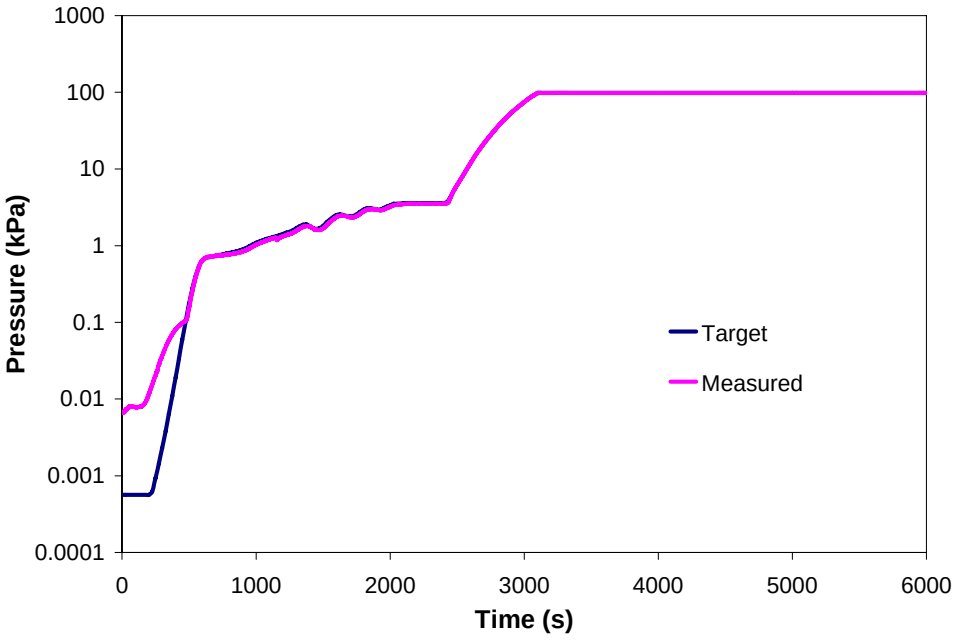

Figure 4.5: Comparison of target and measured re-entry pressure

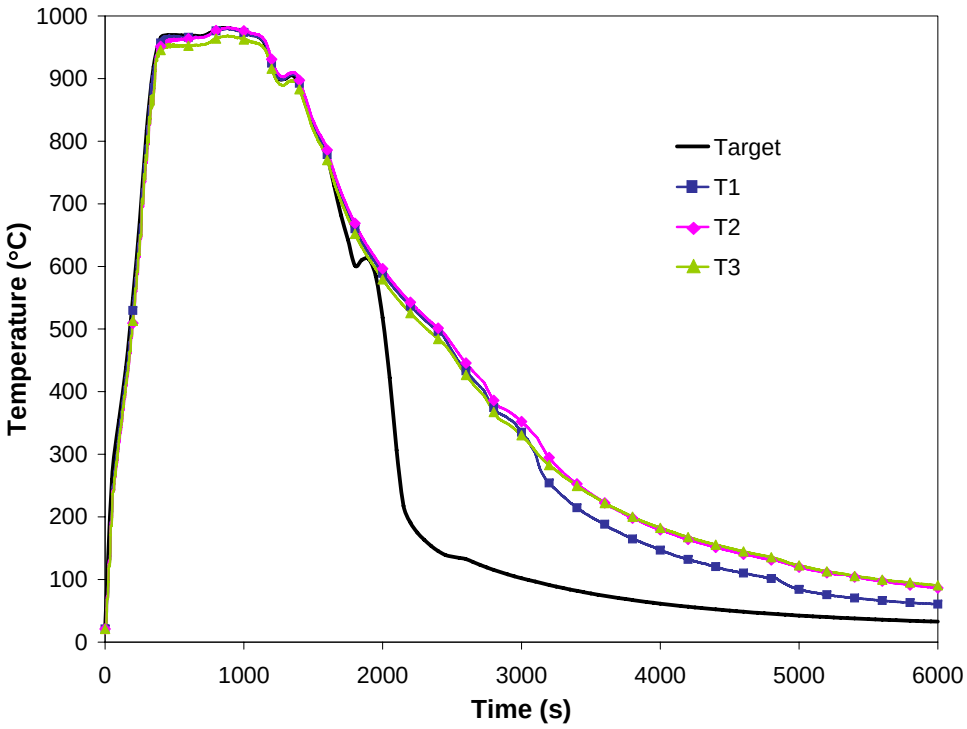

Figure 4.6: Comparison of target and measured surface temperature

CHAPTER V

EXPERIMENTS ON UNDAMAGED AND DAMAGED SHUTTLE TILES AND CORRELATION WITH THE FINITE ELEMENT MODEL

As mentioned in Chapter I, experimental data on the thermomechanical response of damaged TPS is not available in literature. Such results are needed to validate the FE models that have been developed. In this chapter, the experiments conducted on undamaged and damaged HRSI tiles are described. The experimental results are compared with numerical results based on the FE model to determine the accuracy of the FE model.

5.1 Description of Experiments

The experiments are conducted in the Thermal Structure Testing Laboratory described in the previous chapter. Specimen used for the experiments include undamaged and damaged configurations with three different damage sizes, $D = 1.0", 1.5"$ or $1.875"$. Due to the limited number of specimen available, only two tests were conducted for each configuration.

5.1.1 Test Specimen and Load Fixture

The TPS specimen is composed of the LI-900 HRSI tile, Nomex SIP and aluminum panel, which simulates the underlying structure. The square tile has dimensions of 6.0" by 6.0" and a thickness of 2.0". It is coated on five sides with reaction-cured glass (RCG) and the uncoated bottom surface is bonded to the SIP with RTV-560, which is a room-temperature vulcanizing adhesive. The 0.173" thick SIP is also bonded to a square aluminum panel with dimensions 7.5" by 7.5" by 0.063" that represents the underlying structure. A larger aluminum panel is used to allow the use of a load fixture.

The load fixture is similar to that used in Reference 35. The load fixture is made up of two identical square frames with an outer length of 9". The inner window of the frame has a length of 6.2", which is marginally larger than the length of the tile (6.0"). The frames are recessed to allow the aluminum panel to fit snugly. When the specimen and frames are assembled, the underlying structure forms a 0.1" wide border around the tile and SIP, so as to prevent the fixture from interfering with the thermal expansion of the tile and SIP. The test assembly is shown in Figure 5.1. The stainless steel fixture has a different CTE from that of the aluminum panel. When temperature increases, in-plane loads are generated within the aluminum panel due to the mismatched CTE between the fixture and specimen.

5.1.2 Instrumentation

The instrumented specimen and fixture for undamaged and damaged tiles are shown in Figure 5.2. The undamaged specimen was instrumented with eight type-K Nextel-insulated thermocouples (XC-24-K-30, Omega Engineering) and two high-temperature

fully encapsulated Karma-based alloy strain gages (WK-13-062AP-350, Vishay Micromeasurements). For specimen with damage, three additional metal-sheathed type-K thermocouples (XL-K-MO-040, Omega Engineering) were used to measure temperatures within the damaged region. One of the thermocouples, designated Ts, was used for feedback control for the radiant heater system. The procedure for post-processing the raw strain readings from the gages is described in Appendix A. Post-processing of these readings is required to account for the thermal expansion and the change in resistivity and gage factor of the strain gages due to changing temperatures.

5.1.3 Specimen Assembly

The assembled specimen and fixture was placed on top of a steel platform that was lined with cerachem blanket, which is an alumina-silica-zirconia fiber based insulation manufactured by Thermal Ceramics. The sides of the specimen were also covered with the cerachem blankets, leaving only the top surface exposed. The platform was placed underneath the radiant heater which is suspended from the ceiling of the vacuum chamber. Photographs and illustration of the assembly are shown in Figure 5.3.

5.1.4 Pressure and Temperature Profiles

The target re-entry static pressures and temperatures chosen for the experiments were based on the re-entry profile of the Access-to-Space (ATS) reference vehicle. The ATS re-entry pressure and temperature profile are shown in Figure 4.1.

It should be noted that the applied temperatures that would be obtained in the damaged portion of the tile were not known a priori. The damaged surfaces, without the RCG

coating, have different surface properties that affect radiation heat transfer, which is the principal mode of heat transfer in the experiments. The emissivity of the uncoated tile, listed in Table 3.11, decreases rapidly with temperature, while that for the RCG coating remains relatively constant at 0.85. Moreover, uniform heating implemented with radiant heater requires that the heated surface should be at a certain distance away from the heat source and this distance should be at four times the bulb spacing. While the undamaged surfaces are at the required distance from the bulbs, the damaged surfaces are at different distance and orientation relative to the heater.

5.2 Finite Element Model

The FE meshes used for correlating experimental results are shown in Figure 5.4. Again, the DC3D10 and C3D10 elements are used. The mesh in Figure 5.4 (a), consists of the tile, SIP, aluminum panel, fixture and portion of the cerachem insulation, is used for correlating the temperature results obtained in experiments. Due to symmetry, the specimen can be represented by a quarter model of the TPS. Typically in heat transfer numerical analysis, the lower surface of the underlying structure is assumed to be perfectly insulated. However, this cannot be achieved in practice, since all insulation conducts and absorbs heat. Therefore, it is more appropriate to use the measured temperature at the lower surface of the insulation as a boundary condition. The mesh in Figure 5.4 (b) is used for correlating the strain results. In this mesh, the cerachem insulation is not included because it is flexible and thus, it is assumed to have no effect on the stresses and strains in the system. For this case, transient temperature distribution in the system is recalculated by using the measured temperature at the lower surface of the underlying structure as the applied boundary condition, so as to produce more accurate results.

For the heat transfer analysis, the measured temperatures from experiments are applied as boundary conditions at the nodes on the top and bottom surfaces of the meshes, as well as the nodes on the damaged surfaces. All side surfaces are assumed to be perfectly insulated.

In the thermal stress analysis, thermal stresses in the FE model, subjected to structural boundary condition shown in Figure 5.5, are calculated from pre-determined temperature distributions from the heat transfer analysis.

5.3 Experimental Results

The measured temperatures in the damaged region of specimen with $D = 1.5$", TD1, TD2 and TD3, are shown in Figure 5.6. These temperatures are quite similar to the surface temperatures, and the variations between the three measured temperatures are small, with a standard deviation of less than $14\,^{\circ}\mathrm{C}$ after the initial 500 seconds. Figure 5.7 shows the measured temperature, TD3, at the base of the damaged region for damaged specimen with $D = 1.0$", 1.5" and 1.875". The variation in size of the damaged region did not seem to have a large effect on these temperatures, since their average stardard deviation is less than $14\,^{\circ}\mathrm{C}$. These results indicate the limitations of testing damaged TPS in such a facility, since elevated temperatures within damaged region and variations in applied temperatures due to cavity radiation cannot be properly simulated.

As shown in the previous chapter, the temperature uniformity on undamaged surface is very good. Based on these experimental results, the assumption that the applied temperatures on the undamaged and damaged surfaces are uniform is used. The measured temperatures from the center thermocouple (T1 in Figure 5.2) and the average tempera-

ture of the three thermocouples within the damaged region, TD1, TD2 and TD3, are used as boundary conditions in the FE analysis.

5.4 Validation of Finite Element Model

The material properties used in the model are the same as those in Tables 3.6 through 3.11, except for the Young's modulus for the SIP; since the SIP used in the experiments was not proof-loaded [40]. Additional properties required for the cerachem insulation are shown in Table 5.1.

The measured temperature at the center of the underlying structure, T4 in Figure 5.2, is used for validation purposes. The measured temperature and predicted temperature from FE analysis are shown in Figure 5.8. Since the differences in results for the undamaged and damaged configuration with $D = 1.0$" for both experiments and FE analysis are very similar, the $D = 1.0$" results are not plotted. The plots for the experiments in the figure are the averaged data of the two tests conducted for each configuration, and the error bars indicate the spread of the experimental results. No error bars is shown for the $D = 1.875$" experimental results, because only one test was successful. The presence of damage allows the surface temperatures to be applied closer to the underlying structure, however, the damaged size considered combined with the applied temperature load that can be achieved in the test facility results only in modest increase in heat retained within the system. Thus, the changes in temperatures within the structure due to damage are not significant. However, the FE models are able to predict the measured temperatures well, with an average difference (Equation 4.1) of 5.2%, 5.2% and 4.9% for the undamaged and damaged configurations with $D = 1.5$" and 1.875" respectively. When predicting peak

temperatures, the differences are even smaller at 1.4%, 2.8% and 3.2%

Figure 5.9 shows the predicted and measured strain results for the undamaged and damaged ($D = 1.5$" and 1.875") configuration. The FE models yield good results, with an average differences of 5.9%, 5.9% and 10.1% for the undamaged and damaged configurations respectively. The predictions of the peak strain results are even better with a difference of 6.3%, 1.3% and -4.8%.

From Figures 5.8 and 5.9, it can be seen that the FE and experimental results for the $D = 1.875$" specimen deviate from each other to a larger extent. While the difference is still small, it should be noted that the FE results for this damaged configuration indicate that the temperature limit of the SIP ($371\,^{\circ}\mathrm{C}$) is exceeded, as shown in Figure 5.10, where the FEA temperature results for the SIP just beneath the damage for the $D = 1.5$" and 1.875" specimen are plotted. The figure also shows that SIP temperature limit is not exceeded for the $D = 1.5$" specimen. Nomex fibers, which make up the SIP, do not have a melting point, but they decompose above the temperature limit. This decomposition can be seen in Figure 5.11 , where a charred area is evident for the $D = 1.875$" specimen, but not the $D = 1.5$" specimen. This decomposition could be the reason for the lower temperatures, since thermal energy is absorbed during the process. A close examination revealed that the bond between the SIP and the tile at the charred area is compromised, however, the bond line between the SIP and underlying structure is still intact. This may account for the higher strains in the underlying structure since the SIP affected would allow larger deformations in the structure. The results indicate that exceeding the temperature limit of the SIP does not seem to have a significant effect on the TPS response. Thus, it can be concluded that the FE model is in good agreement with the experiments, which represents a verification of the FE analysis.

Results from experiments illustrate the limitations of testing damaged TPS under radiant heating. Due to the inability to reproduce non-uniform and elevated temperatures within the damaged region, such tests have limited value. However, these results were very useful for the validating the FE simulation model, which subsequently is extended to incorporate more realistic heat loads based on interaction between flow and damaged TPS that corresponds to a situation encountered under flight conditions.

T (°C)	c (J/kg °C)	k (W/m-°C)
0	659.8	0.04
260	1055	0.07
538	1206	0.15
816	1256	0.27
955	1269	0.35
1093	–	0.41

$\rho = 96 \ kg/m^3$

Table 5.1: Material properties for Cerachem blankets

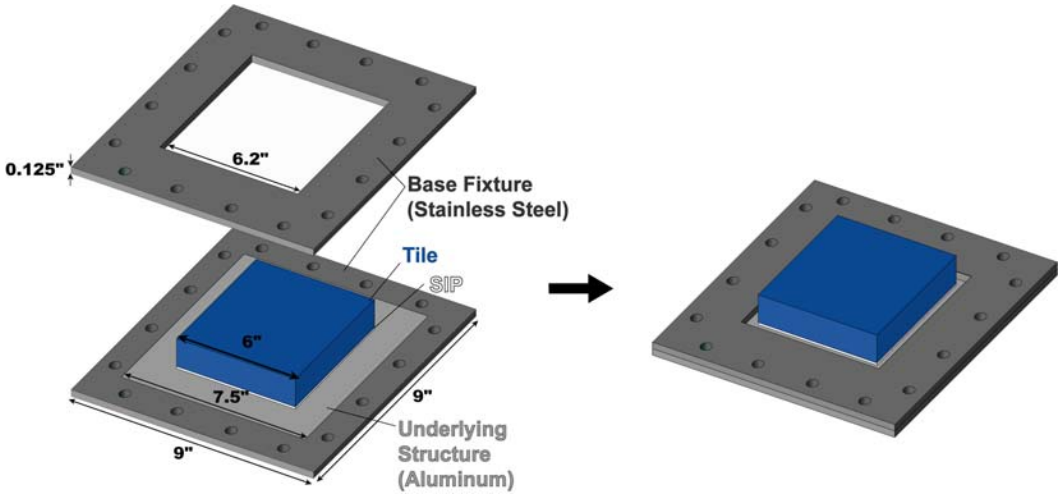

Figure 5.1: TPS specimen and load fixture

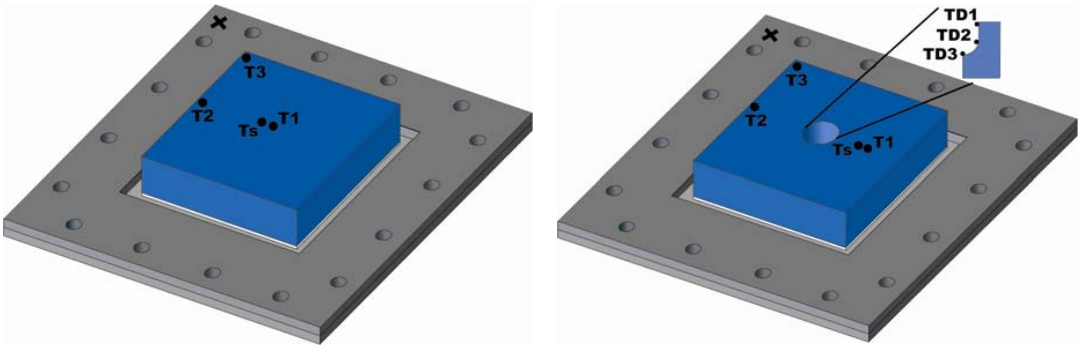

Top view

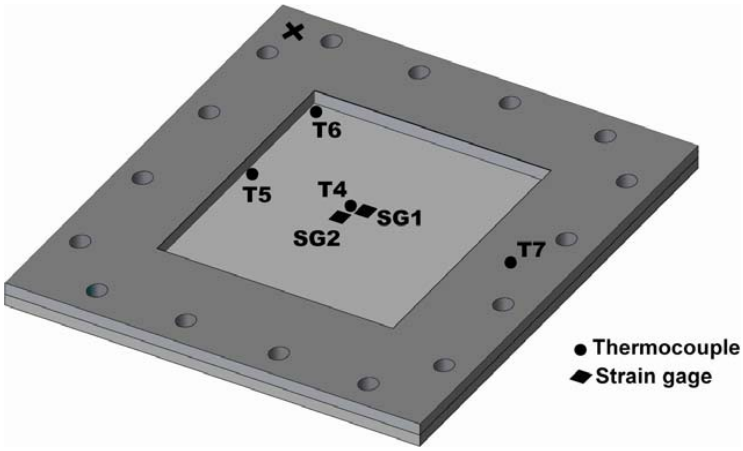

Bottom view

Figure 5.2: Location of thermocouples and strain gages on instrumented specimen

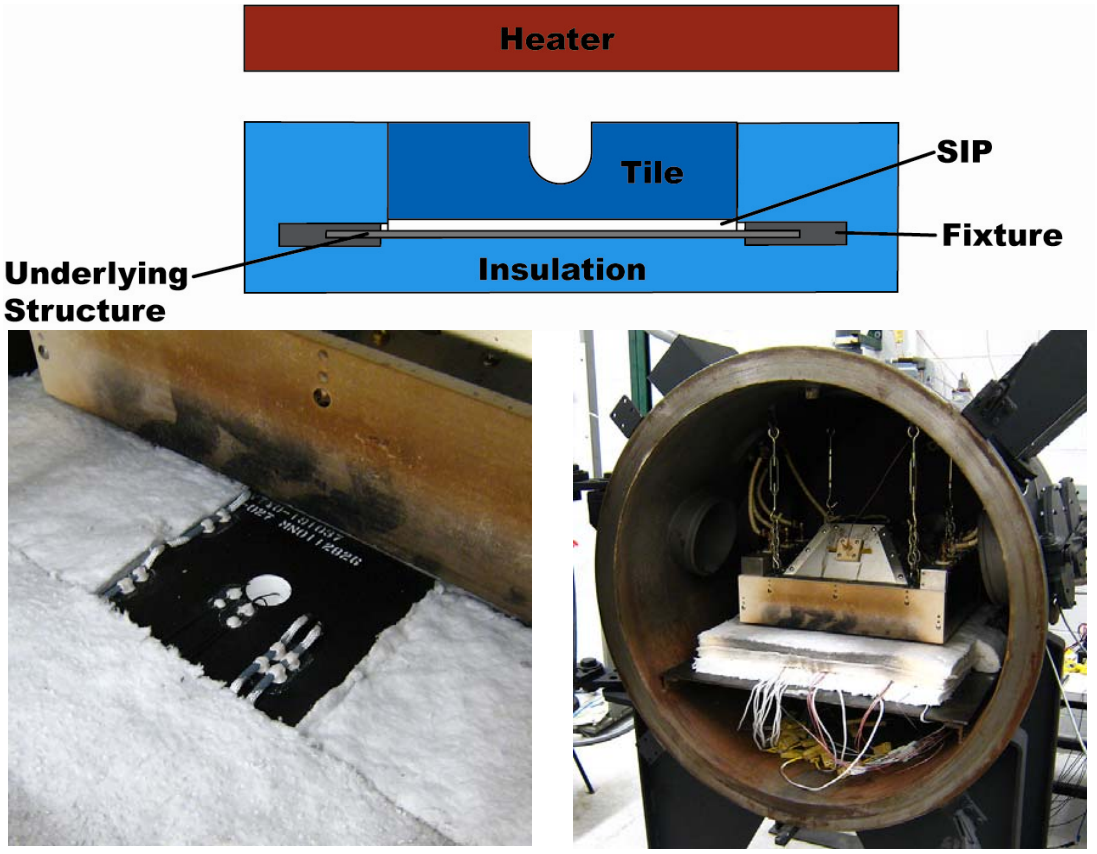

Figure 5.3: Illustration and photographs of test setup

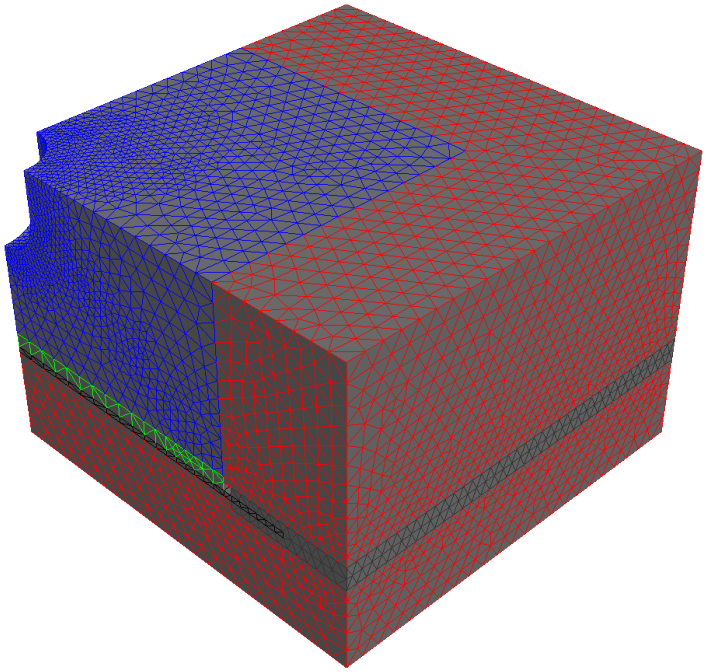

(a)

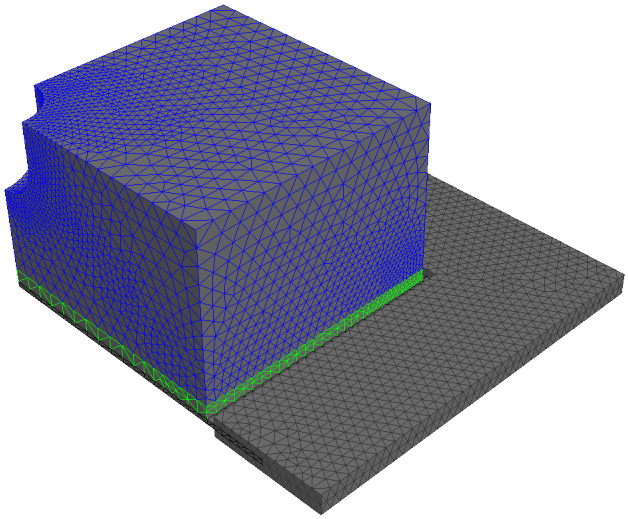

(b)

Figure 5.4: FE meshes for correlation studies

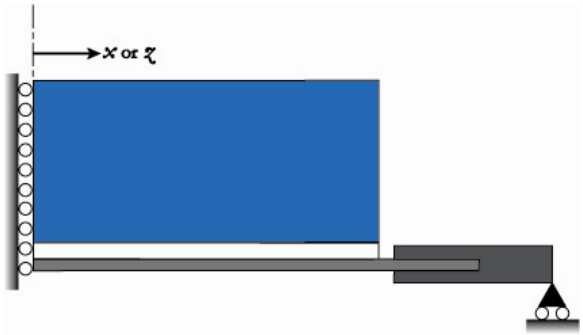

Figure 5.5: Unrestrained boundary condition applied to underlying structure

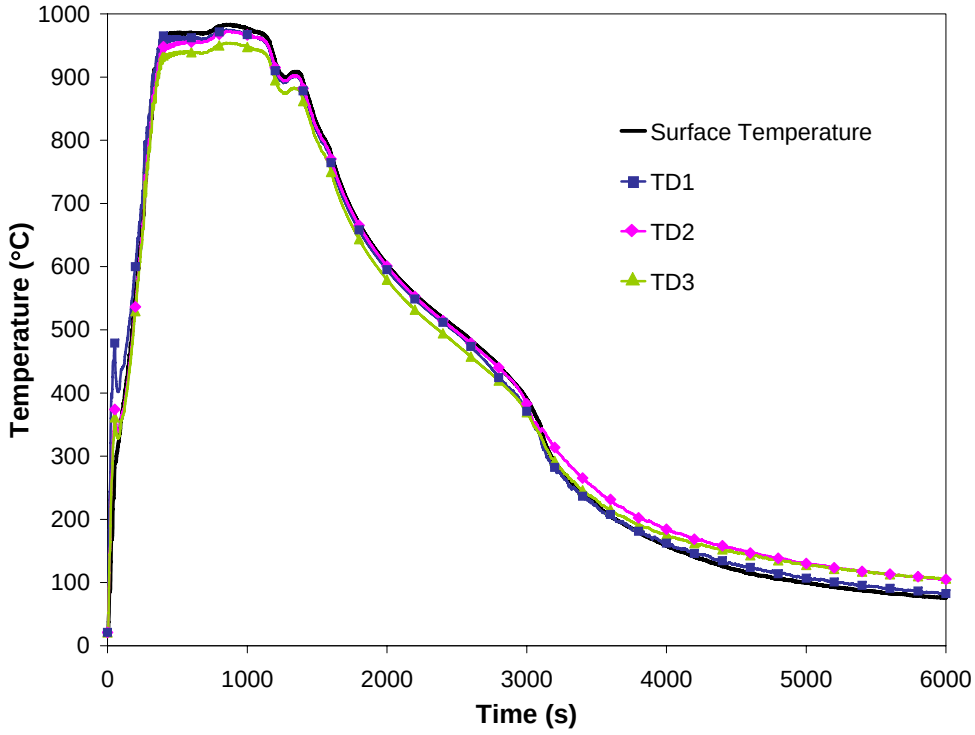

Figure 5.6: Comparison of temperatures obtained in experiment on surface and in damaged region of specimen

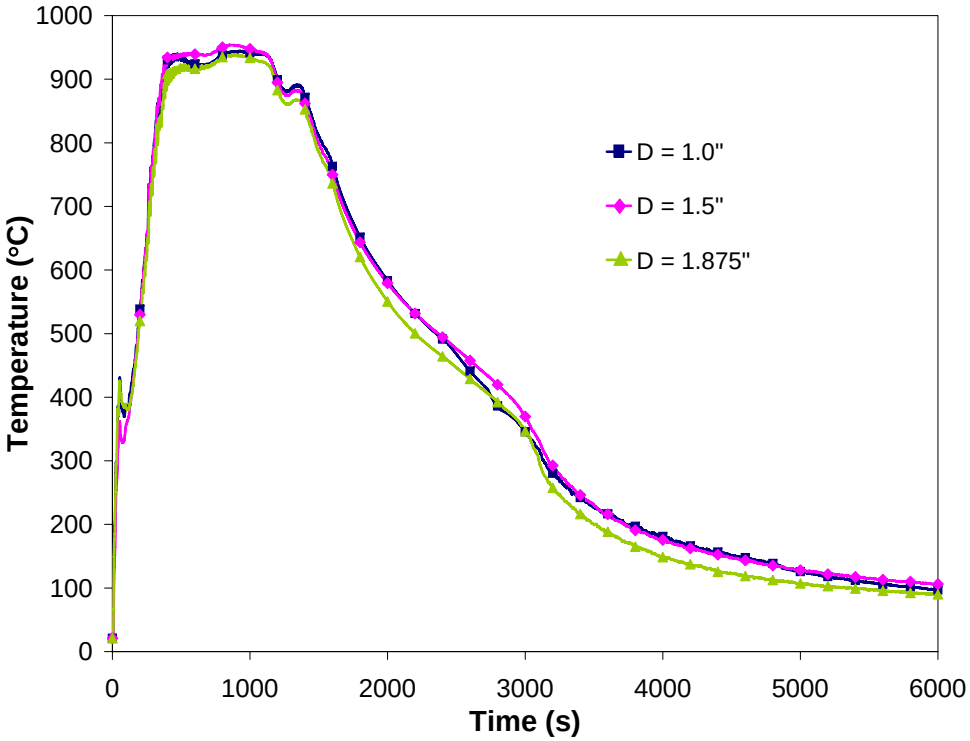

Figure 5.7: Comparison of temperatures at base of damaged region for various damage size

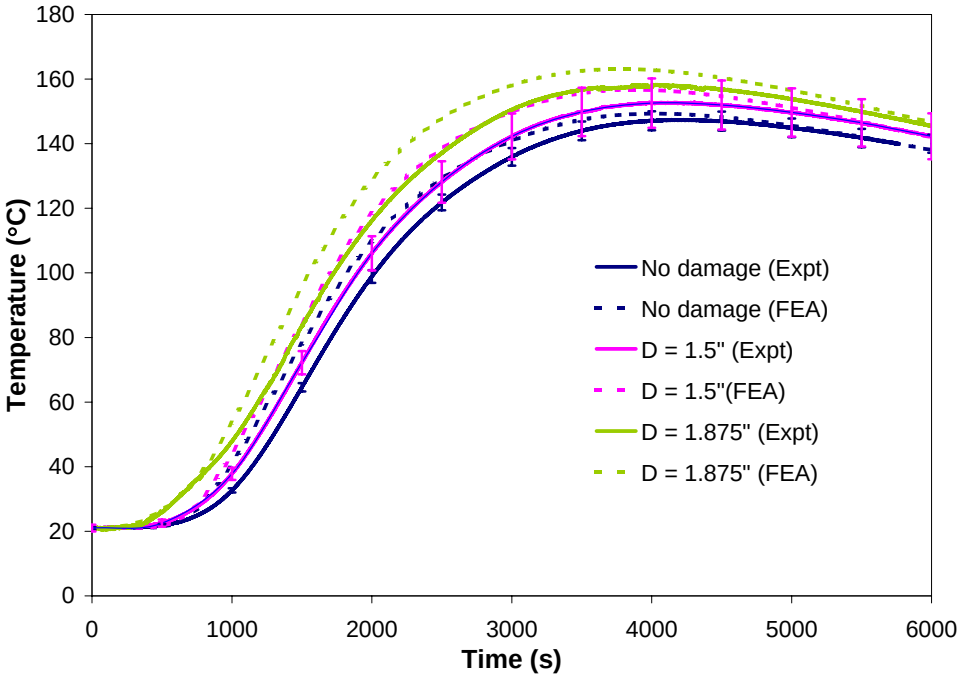

Figure 5.8: Comparison of predicted and measured temperatures

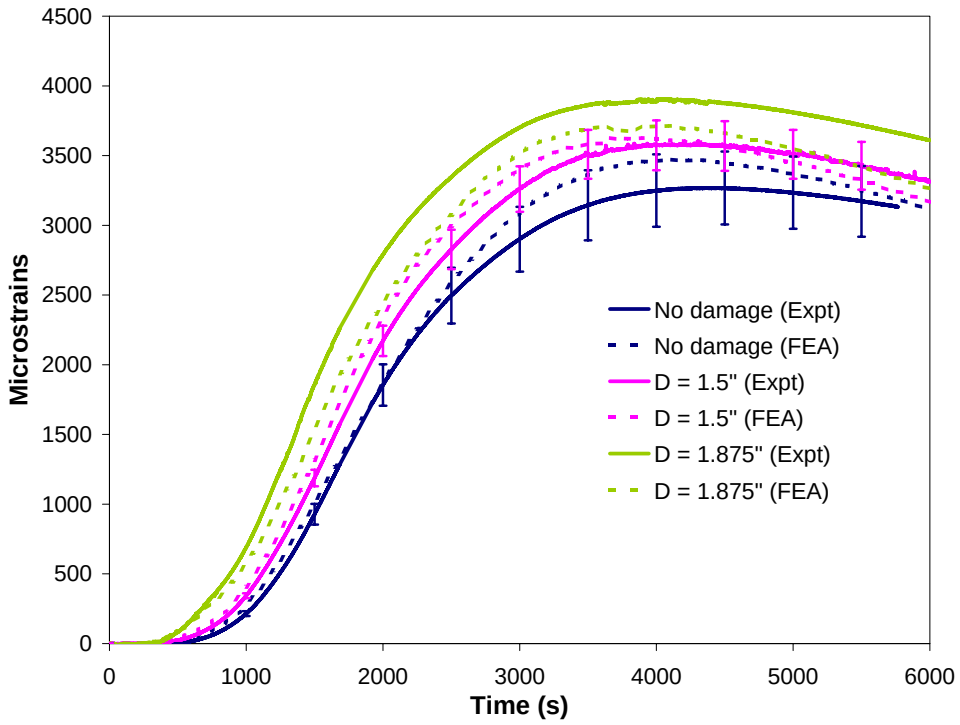

Figure 5.9: Comparison of predicted and measured strains

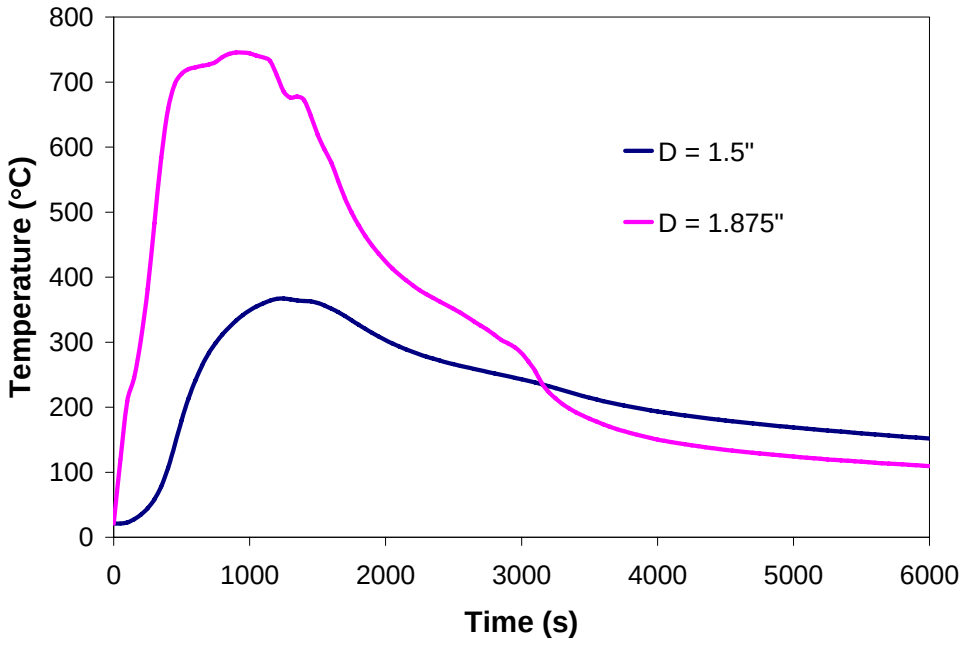

Figure 5.10: FEA temperature results in the SIP for $D = 1.5$" and 1.875" damaged configuration

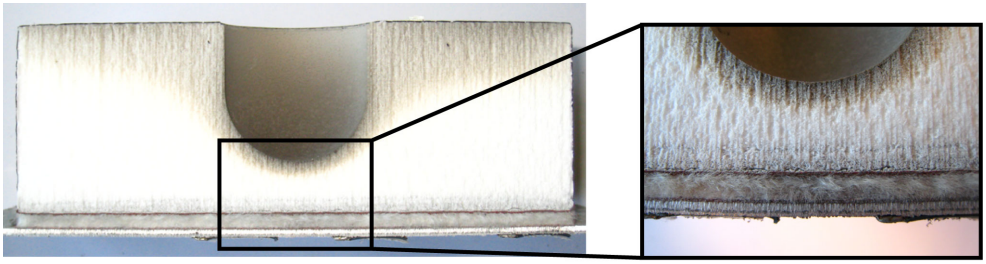

(a) $D = 1.5$” specimen

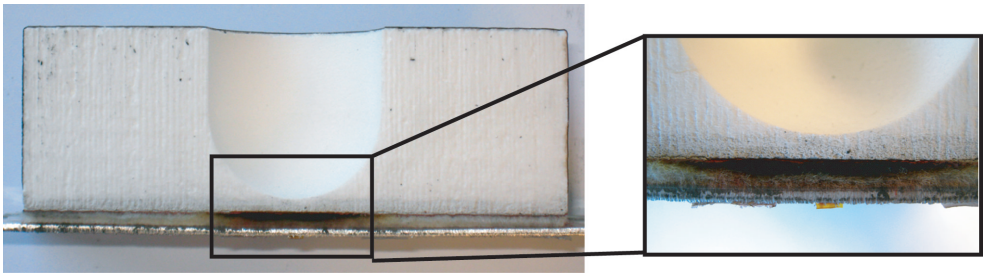

(b) $D = 1.875$” specimen

Figure 5.11: Cross section of experimental specimen

CHAPTER VI

THERMOMECHANICAL BEHAVIOR OF DAMAGED TPS SUBJECTED TO FLOW-DEPENDENT HEAT LOAD

The FE analysis described in previous chapters assumed that the aerodynamic heating through the damaged region is spatially uniform. However, the heat load profile on the damaged surface of the tile is dependent on the fluid dynamics of a high speed flow past a cavity. The interaction between the damaged region and the high speed flow will modify substantially the uniform heat load used for undamaged surfaces [30, 45]. To improve on the thermomechanical analysis, the flow conditions in the damaged region must be carefully considered.

6.1 Flow Dependent Thermal Loads

The temperature profiles on damaged TPS obtained in the experiments conducted are quite different to what may be actually observed in actual re-entry flight. If the thermal loads based on actual flight conditions are known, the experimentally validated FE models can be extended to predict the TPS behavior more accurately.

6.1.1 Hypersonic Cavity Flow

Hypersonic flow past a cavity on the surface of a vehicle is a challenging problem due to complex flow characteristics, such as hypersonic flow separation [12, 30]. Flow separation is important for the heat transfer problem since the aerodynamic heat load varies spatially as the flow passes over the cavity representing the damaged region on the surface of the TPS. For cavity geometries shown in Figure 6.1, this flow problem was studied both computationally [34, 45], and experimentally [12, 30, 45]. Cavity flows are typically denoted as either open or closed, depending on certain flow characteristics. In open cavity flows, the external flow passes over the cavity and the separated shear layer re-attaches near the top corner of the upstream-facing wall, thus producing circulation inside the cavity, as shown in Figure 6.1. Conversely, for closed cavity flows, the separated shear layer re-attaches to the cavity floor upon impingement and then separates again as it approaches the upstream-facing wall [12, 34, 45]. The combination between the length to depth ratio of the cavity and the speed of the flow determines whether the cavity flow will be open or closed. Typically, supersonic and hypersonic cavity flows are open if the length to depth ratio of the cavity varies from 1 to 10. Note that the damage considered in this study has a length to depth ratio of 1, and thus it will produce an open cavity flow.

Two approaches to improve the heat load estimate on a damaged tile are considered in this study. First, the aerothermodynamic flow conditions in the cavity were computed using computational fluid dynamics (CFD) code CFL3D developed by NASA Langley Research Center [22]. This approach is convenient since the computation can be performed for any damage profile considered in the thermomechanical analysis. Two issues that limit the accuracy of this approach are the lack of ability to model real gas effects and the limited

information of local operating conditions near the damaged tile.

In the second approach, an approximate heat load profile was extracted from results provided in recent studies [12, 34] dealing with the *Columbia* accident investigation and Space Shuttle Return to Flight Program. The advantage of this approach is that both real gas effects and local flow conditions are captured by this data. Another advantage is the availability of experimental results for validation purposes. The disadvantage is the inability to match the details of the required damage geometry.

6.1.2 Thermal Loads from CFL3D

The CFL3D code uses an implicit finite-volume algorithm based on upwind-biased spatial differencing to solve the time-dependent Euler and Reynolds-averaged Navier-Stokes equations. Multi-grid and mesh sequencing are available for convergence acceleration. The algorithm, which is based on a cell-centered scheme, uses upwind-differencing based on either flux-vector splitting or flux-difference splitting, and can sharply capture shock waves. This study utilizes the flux-vector splitting scheme. The grid used to generate aerodynamic heating data for the damaged tile is shown in Figure 6.2. It consists of $2 \times 433 \times 225$ grid points that extend from 3.5" in front of the damaged section to 2.5" behind the damaged section, and 4.0" above the tile surface. Note that the damaged portion of the tile considered here consists of a strip having a width of 1.0", and a depth of 1.0", and it contains $2 \times 151 \times 140$ grid points. This grid geometry implies that only two-dimensional flow past the cavity is considered.

The operating conditions used to generate the aerodynamic heating on the tile are provided in Table 6.1. These operating conditions are based on those used in a previous exper-

imental and computational study of hypersonic cavity flows [45]. They were selected since the actual flow conditions on the ATS vehicle are not readily available. These conditions produce laminar flow conditions [45], and therefore the laminar flow option in CFL3D was implemented. The maximum heat load values for the ATS are assumed to occur during laminar flow conditions, so the use of the laminar flow assumption is appropriate.

Figure 6.3 depicts the heat load ratio profile obtained from the CFL3D simulation. The heat load ratio is defined as the local heating data (q) normalized by reference heating data (q_0) obtained from undamaged smooth surface configuration with the same simulation conditions. The results are plotted as a function of a non-dimensional coordinate X_s/D. According to the definition of X_s, the downstream-facing wall is located between $0 < X_s/D < 0.5$, the floor of the cavity is located between $0.5 < X_s/D < 2.07$, and the upstream-facing wall is located between $2.07 < X_s/D < 2.57$.

Consistent with open cavity flows [12, 30, 45], the heat load ratios within the damage region are generally less than 1.0 except for the portion near the upstream-facing lip of the damage, where the reattachment of the flow occurs. High heat loads are also evident in a region located a small distance downstream of the damaged region.

6.1.3 Thermal Loads from Published Data

In References 12 and 34, both computational and experimental aerothermodynamic results were generated for hypersonic flows past rectangular cavities. In Reference 34, CFD was used to predict the hypersonic aerothermodynamic environment for a Shuttle Orbiter with windside tile damage. Furthermore, the computations were performed at the peak heating trajectory point, using the Langley Aerothermodynamic Upwind Relaxation Algo-

rithm (LAURA) code. Note that this code is intended for simulating hypersonic re-entry physics including chemistry [34]. In Reference 12, results from wind tunnel experiments were generated for cavities and flow conditions similar to those studied in Reference 34. The experiments were conducted in the Langley 31-inch Mach 10 tunnel. In both cases the cavity length-to-depth ratio was 7.5 [12, 34].

Figure 6.4 depicts heat load ratio profile along the cross section where the maximum heat load ratio is observed within the 3D rectangular cavity based on CFD simulation of the flight conditions [34]. Due to the presence of corners in the cavity geometry, sharp dips in heat load ratios are present in the profile.

6.1.4 Applied Thermal Loads for Finite Element Analysis

Figure 6.6 shows the heat load ratio profiles obtained using the two approaches described above. The "uniform" profile shown in the figure corresponds to the approximate upper bound heat load used in earlier chapters. These profiles were used in the current study as scaling factors to multiply the applied surface heat load in order to determine the heat load in the damaged region.

The maximum heat load ratio from the CFL3D results due to flow reattachment at the lip of the upstream-facing wall of the damage, was found to be very large ($q/q_0 = 21.5$). Such high peak heat load ratios were not observed in experiments [12, 30]. The maximum heat load ratio for an open cavity observed in the experiments described in Reference 12 was approximately 4.5; therefore it was decided that the maximum heat load ratio for the profiles used in this study was limited to 4.5.

The heat load ratio profile based on published data by Everhart et. al. [12] and Pul-

sonetti et. al. [34] is denoted here as the EP profile. The heat load ratio results along the vertical walls of the cavity were not presented in References 12 and 34. The variation of the profile between $0 < X_s/D < 0.5$ and $2.07 < X_s/D < 2.57$ was obtained by assuming that the results along the vertical walls are similar to those in the CFL3D profile. Thus, the sharp dips in heat load ratios in Figure 6.4 are not present in the EP profile. The maximum heat load ratio was limited again to 4.5 based on the experiments in Reference 12.

The EP profile is generally more severe than the CFL3D profile; this is probably due to the fact that the cavity length-to-depth ratio for EP profile is much larger than that for the CFL3D profile (7.5 vs. 1.0) and it had been noted that heating data in cavities increases with their length-to-depth ratio [45]. The difference may also be due to the use of local flow conditions in the EP profile, compared to freestream conditions used in the CFL3D result. For the EP profile, the flow pass a cavity located on an actual vehicle is used. Before the flow reaches the cavity, it passes through a strong bow shock, thus resulting in a lower Mach number and higher temperatures and pressures when compared to freestream conditions.

6.2 Finite Element Mesh and Method

Figure 6.7 shows the FE mesh used for the analysis. A half-model is required in order to capture the effects of the flow. In the analysis, heat flux boundary conditions are applied on the top surface of the mesh. The boundary conditions are based on the transient aerodynamic surface heat load re-entry profile of the ATS reference vehicle as shown in Figure 6.5. The sides and the inner surface of the TPS are assumed to be perfectly insulated, which corresponds to a worst-case scenario. While this profile is appropriate for the

undamaged portions of the tile, special consideration is required in the damaged region.

To apply the flow dependent heat loads, the tile surface is divided into several sections as shown in Figure 6.8. On the undamaged surface, colored in green, a small region right after the damage is separated to allow elevated heat loads to be applied. Within the damage, the surface was divided into two sections: the downstream-facing section, colored light blue, and the upstream-facing section, colored blue. These two sections are further divided into sub-sections so that reasonable linear or polynomial curve fits can be obtained for the heat load ratio profiles shown in Figure 6.6.

The curve fits for the heat load ratio profiles are obtained as functions of y only, i.e. the heat load ratio varies only with the depth of the damage. In order to have a three-dimensional variation of the heat load ratio, the curve fits for each subsection are multiplied by a bilinear function of y and z of the form:

$$F(y,z) = A_1 y + A_2 yz + A_3 z + A_4 \tag{6.1}$$

To determine the coefficients, A_1 – A_4, for each subsection, the following assumptions are made:

1. Along the centerline of the damage (thick bold line in Figure 6.8), the heat load ratio profile is the same as that in Figure 6.6.

2. At the outer edge of the damage, the heat load ratio is equal to 1.0, since the tangent of the edge is parallel to the flow.

3. Along the dotted bold line in Figure 6.8, the heat load ratio at the corners of each subsection is the average of the centerline heat load ratios from the upstream and

downstream-facing sections.

Figure 6.9(a) shows the heat load ratios from the EP profile at the corners of each subsection within the damage. The exact values from the EP profile are in bold type, while the values based on the assumptions above are in regular type.

Figure 6.9(b) shows the values that Equation 6.1 has to satisfy in order to obtain the required heat load ratios at each corner of the subsections from the curve fits. Using these values, the coefficients, A1 - A4, for each subsection can be calculated. Essentially, Equation 6.1 preserves the EP profile along the centerline of the damage while allowing it to vary linearly with respect to z to the required values at the corners of each subsection.

The FE procedures and boundary conditions used in this chapter are similar to those in Chapter III.

6.3 Results and Discussion

The flow dependent heat loads (CFL3D and EP) are generally of lower magnitude than the surface heat load except for two regions: a very small region at the upper lip of the downstream-facing section and a larger region on the upper lip of the upstream-facing section. In these regions, the peak heat load for both flow dependent heat profiles are larger than the surface heat load by a factor of 4.5. In previous chapters, it was determined that when subjected to the "uniform" heat load, cavity radiation and the reduction in emissivity due to the loss of the RCG coating resulted in very high temperatures within the damage. Thus, it is not unreasonable to assume that the large spike in heat load due to flow reattachment would generate much higher maximum temperatures in the tile. However, the maximum temperatures in the tile due to flow dependent heat loads are similar

in magnitudes to those obtained from the "uniform" heat load with the CFL3D heat load producing results that are less than 7% lower and the EP heat load producing results less than 9% higher. There are several explanations for this behavior. First, at such high temperatures, heat loss by radiation is so efficient ($\propto T^4$) that even with a large increase in heat load, the increase in temperatures are relatively modest. Second, the "uniform" heat profile, where all surfaces within the damaged region are subjected to the same heat load as the surface, is actually quite severe. Third, for the flow dependent heat profiles, other than the two small areas which experience higher heat loads, much of the surfaces within the damaged region are subjected to substantially lower heat loads when compared to the "uniform" profile.

Figure 6.10 illustrates the temperature contour plot of the damaged configuration, with $D = 1.0$", subjected to EP heat load when the maximum temperature in the tile is attained. The non-uniformity of the heat load, coupled with cavity radiation, results in a complex distribution of temperatures within the damaged region. Even though much of the heat load within the damaged region is lower than the surface heat load, the effects of cavity radiation retained substantial heat to elevate the temperatures to above surface temperatures. It is also interesting to note that similar elevated heat load on the undamaged surface downstream of the damaged region, where there is neither cavity radiation nor reduction in emissivity, produces maximum temperatures that are significantly lower than those within the damaged region. Considering the experimental results that were obtained, it can also be concluded that this complex temperature boundary conditions due to flow effects cannot be achieved using radiant heaters. Thus, meaningful experiments for damaged TPS can only be conducted in arc-jet hypersonic facilities where interactions between damage and flow can be replicated.

For the tile, the smallest damage considered with the CFL3D heat load increases the maximum temperature by 73.6% to $1,703\,^{\circ}\mathrm{C}$ which is slightly lower than the melting point of the tile ($1,704\,^{\circ}\mathrm{C}$). In all other cases, the melting temperature of the tile was exceeded. For the largest damage size, the EP heat load increases the maximum temperature to $2313\,^{\circ}\mathrm{C}$, which represents a massive increase of 135.8%. However, it should be noted that the EP profile was for a cavity that has a much larger length-to-depth ratio than the CFL3D results. Temperatures in the SIP and underlying structure are also increased significantly, by up to 101%. However, the results indicate that the imposed limit temperature of the underlying structure ($150\,^{\circ}\mathrm{C}$) is exceeded while the vehicle is still in flight ($< 3,000$ seconds) only for the $D = 1.5$" cases. However, it should be noted that no heat loss through the inner surface and sides of the system was assumed, which is a very conservative assumption.

The thermal stress results are obtained disregarding the melting temperature of the tile. The presence of damage increases the maximum von Mises stresses in the tile substantially. The smallest damage size considered increases the maximum stresses by more than 30%. The large increase in stresses is a result of the stress concentration due to damage as well as the severe thermal gradients generated by the flow dependent heat loads. For the cases based on CFL3D, maximum stresses in the tile decrease with damage size. With the EP heat load, no discernible trends were observed. The failure strength of the tile was not exceeded in all cases.

The maximum stresses for both the SIP and structure increase with increasing damage size. For both SIP and underlying structure, the maximum stresses were found to be above the failure strength of the material when $D = 1.5$" with both heat loads. However, this should be viewed in light of the fact that conservative boundary conditions had been used.

Damage changes the surface geometry of the TPS. This causes the flow to separate and reattach, and elevate the thermal loads on the TPS. The damage also reduces the heat rejection capability of the TPS by removing the RCG coating and allowing cavity radiation to take place. These effects raises the temperatures within the damaged TPS significantly and can cause the melting point of the tile to be exceeded. While the damage sizes considered are unlikely to adversely affect the underlying structure and SIP during flight, the exceeded melting point of the tile is a concern. The tile is not a load-bearing structure, thus damage growth need not necessarily lead to catastrophic failure. As the maximum temperature occurs at the upper lip of the damaged region, damage progression will likely open up the cavity and alleviate the effects of cavity radiation. However, the nature of the flow and heat load will also be changed.

Mach Number (M)	8.1
Reynold's Number (Re)	1.0×10^6
Stagnation Temperature (T_0)	1050 K

Table 6.1: Maximum temperature results for all TPS components subjected to flow dependent heat loads

TPS component	*D* (inch)	Temperature (°C)		% change		Time (s)	
Tile	0	981		NA		850	
	0.5	**1703**	*1940*	**73.6**	*97.8*	**850**	*850*
	1.0	**1898**	*2171*	**93.5**	*121.3*	**850**	*850*
	1.5	**2080**	*2313*	**112.0**	*135.8*	**850**	*850*
SIP	0	150		NA		5000	
	0.5	**153**	*160*	**2.0**	*6.7*	**4950**	*4950*
	1.0	**173**	*206*	**15.3**	*37.3*	**4850**	*4700*
	1.5	**215**	*302*	**43.3**	*101.3*	**4450**	*4150*
Underlying structure	0	150		NA		5450	
	0.5	**153**	*159*	**2.0**	*6.0*	**5400**	*5450*
	1.0	**172**	*205*	**14.7**	*36.7*	**5250**	*5100*
	1.5	**213**	*300*	**42.0**	*100.0*	**4900**	*4500*

CFL3D – **bold,** EP - *italics*

Table 6.2: Maximum temperature results for all TPS components subjected to flow dependent heat loads

TPS component	*D* (inch)	Max. von Mises stress (kPa)		% change		Time (s)	
Tile	0	65.0		NA		200	
	0.5	**99.8**	*87.9*	**53.5**	*35.2*	**150**	*150*
	1.0	**88.2**	*84.4*	**35.7**	*29.8*	**150**	*400*
	1.5	**79.9**	*100.4*	**22.9**	*54.5*	**250**	*500*
SIP	0	172		NA		5450	
	0.5	**178**	*185*	**3.5**	*7.6*	**5400**	*5350*
	1.0	**197**	*228*	**14.5**	*32.6*	**5250**	*5050*
	1.5	**232**	*284*	**34.9**	*65.1*	**4900**	*4500*
Underlying structure	0	470,000		NA		5450	
	0.5	**493,000**	*514,000*	**4.9**	*9.4*	**5400**	*5400*
	1.0	**556,000**	*649,000*	**18.3**	*38.1*	**5250**	*5100*
	1.5	**665,000**	*834,000*	**41.5**	*77.4*	**4900**	*4500*

CFL3D – **bold,** EP - *italics*

Table 6.3: Maximum von Mises stress results for all TPS components subjected to flow dependent heat loads

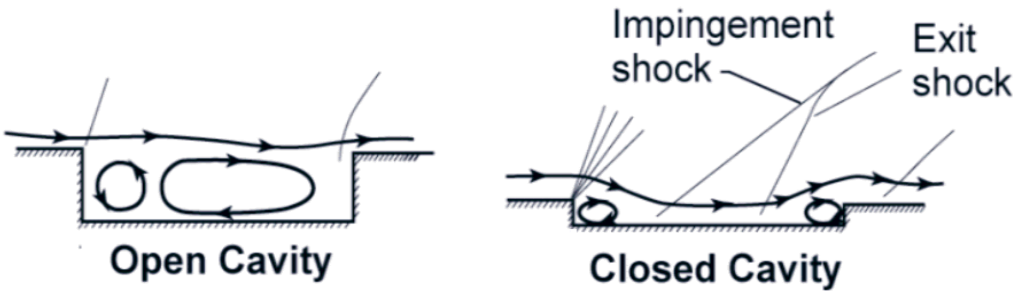

Figure 6.1: Different types of supersonic/hypersonic cavity flows

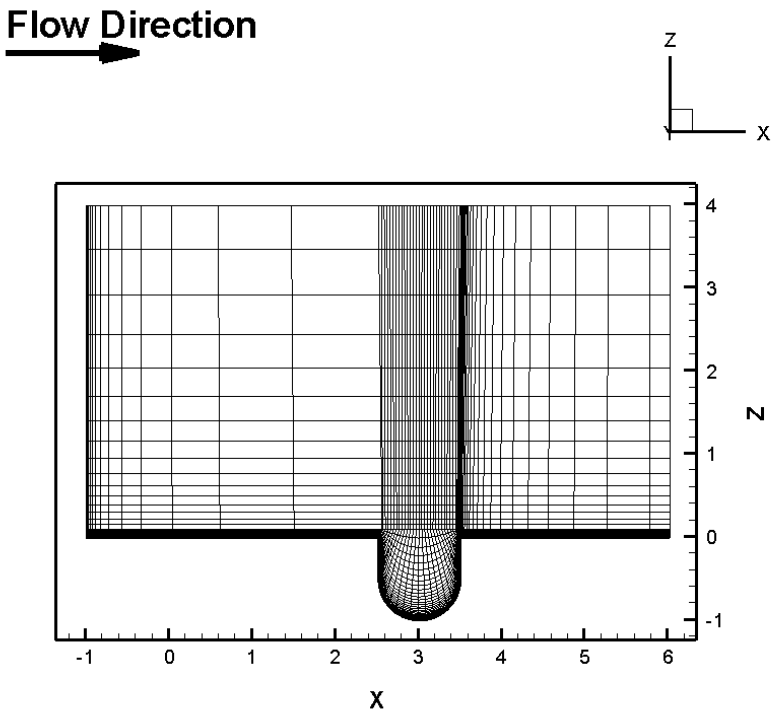

Figure 6.2: Coarsened view of CFL3D computational domain for damaged tile

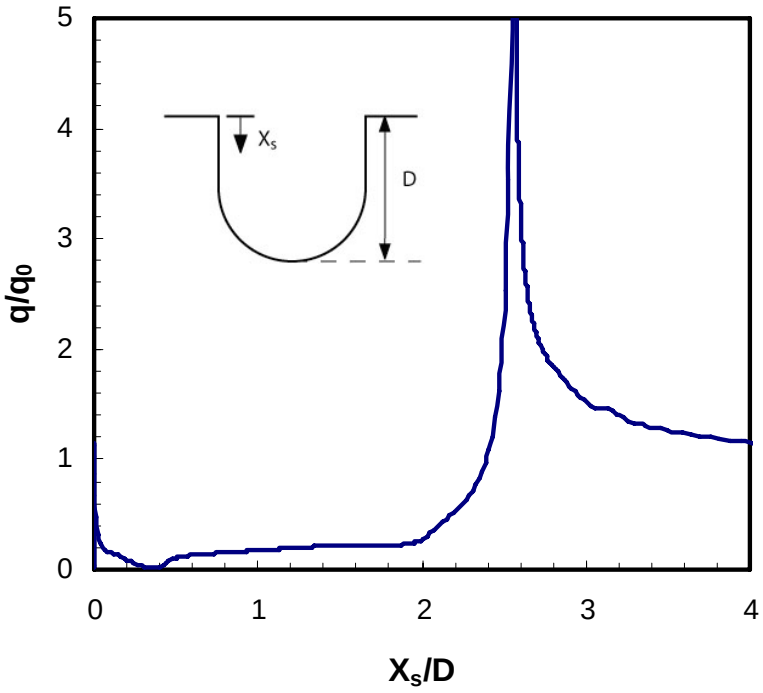

Figure 6.3: Heat load ratio along damaged surface from CFL3D analysis

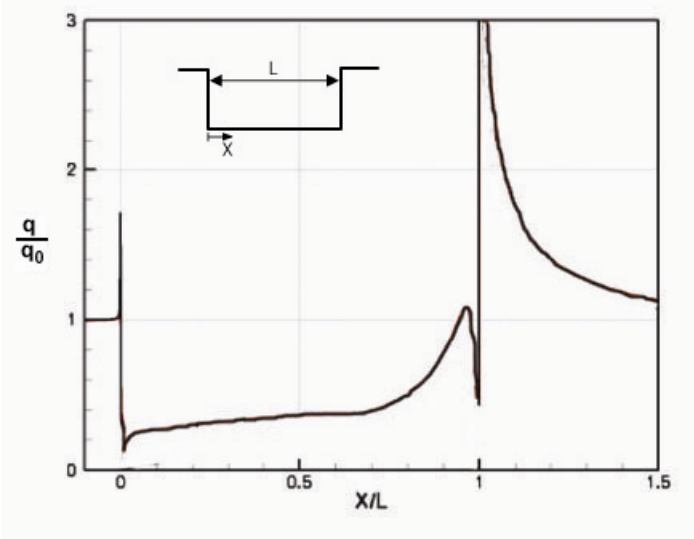

Figure 6.4: Heat load ratio profile from Reference 34

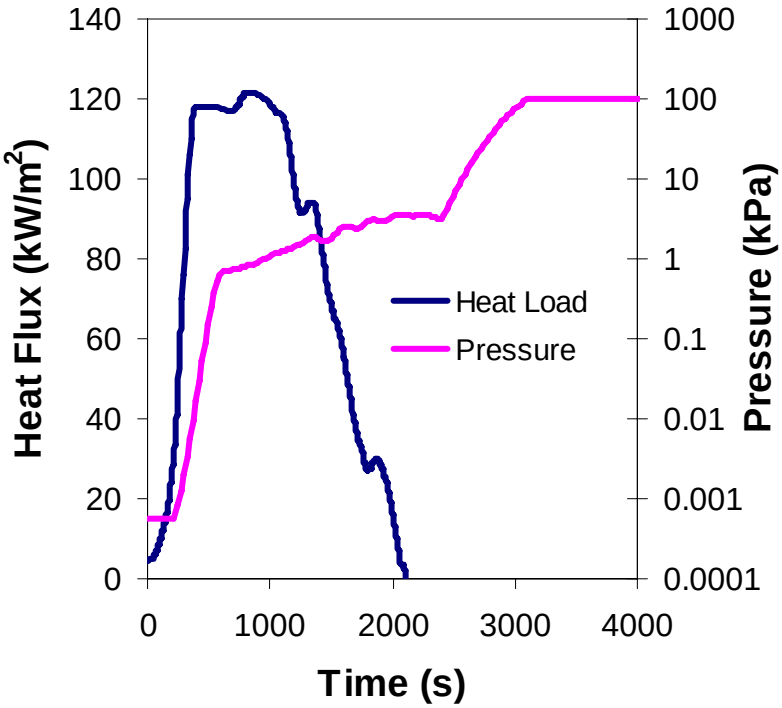

Figure 6.5: Re-entry surface heat load and pressure of ATS vehicle

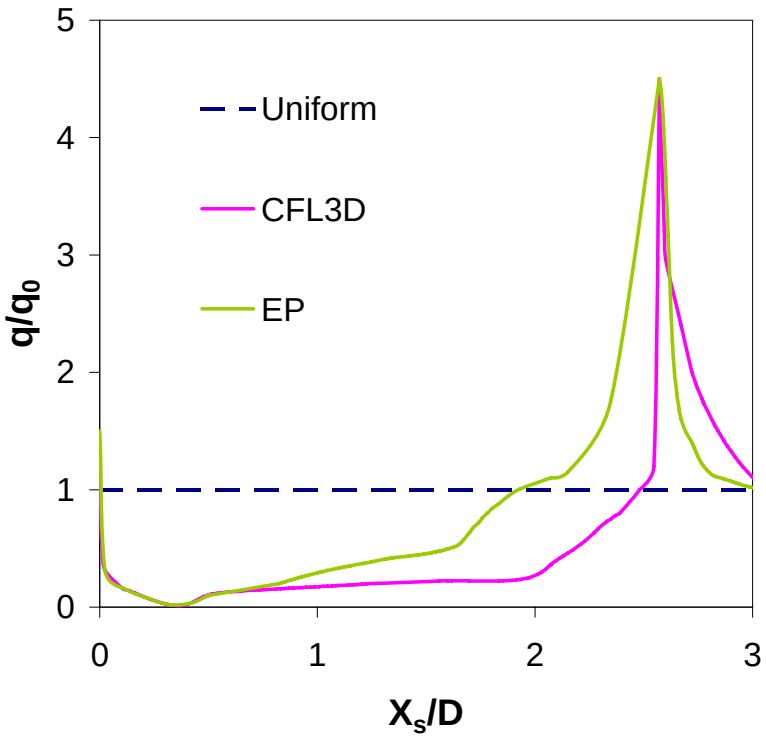

Figure 6.6: Heat load ratio profiles based on CFL3D and published data (EP)

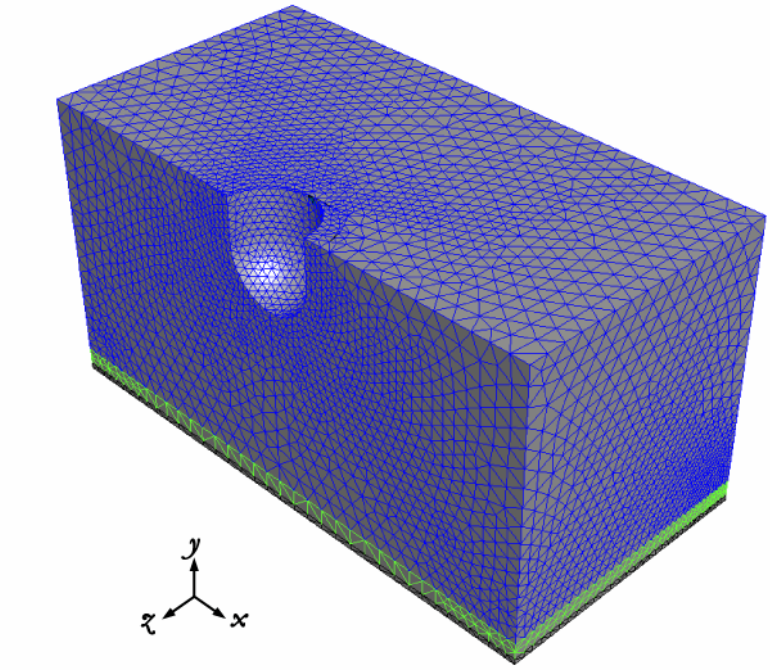

Figure 6.7: FE mesh used in analysis

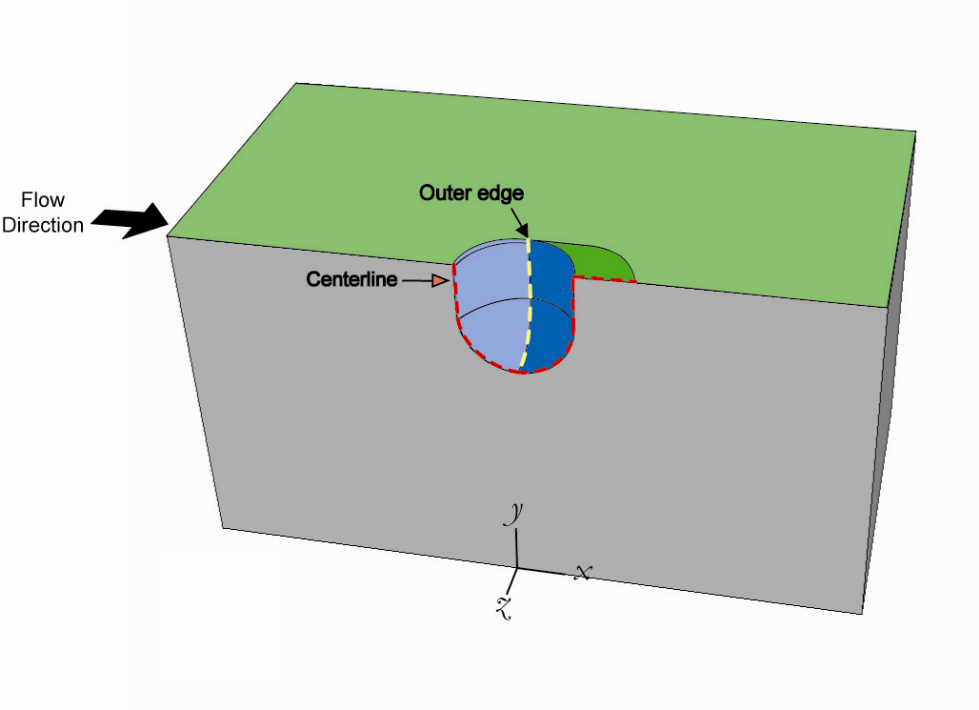

Figure 6.8: Half model of TPS showing the different sections required for application of flow dependent heat load

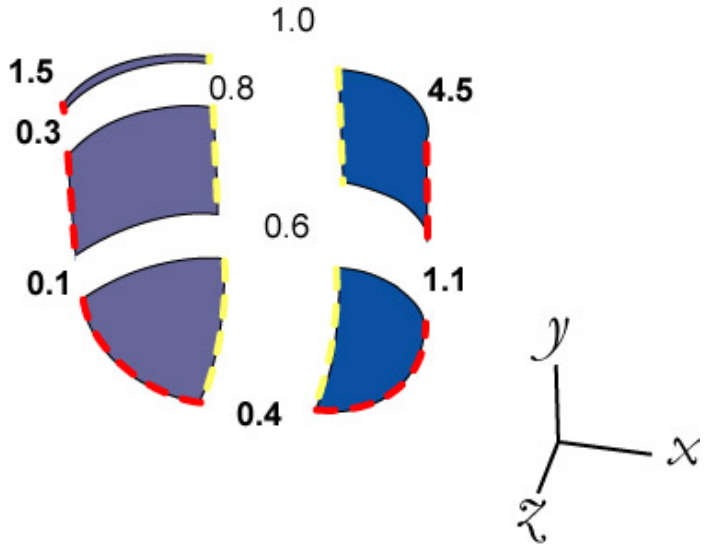

(a) Heat load ratios at corners of subsections

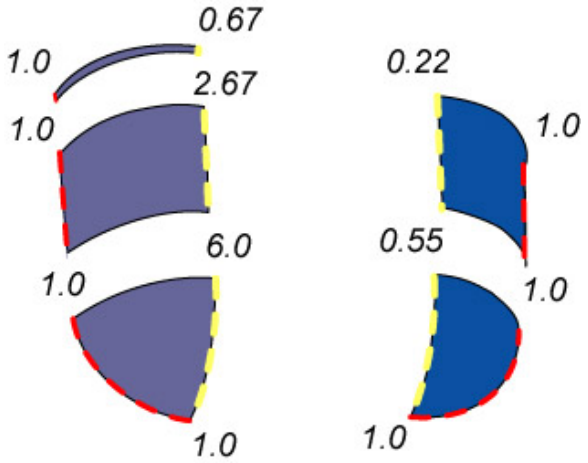

(b) Values for calculating coefficients of Equation 6.1

Figure 6.9: Schematic of subsections of damaged surface

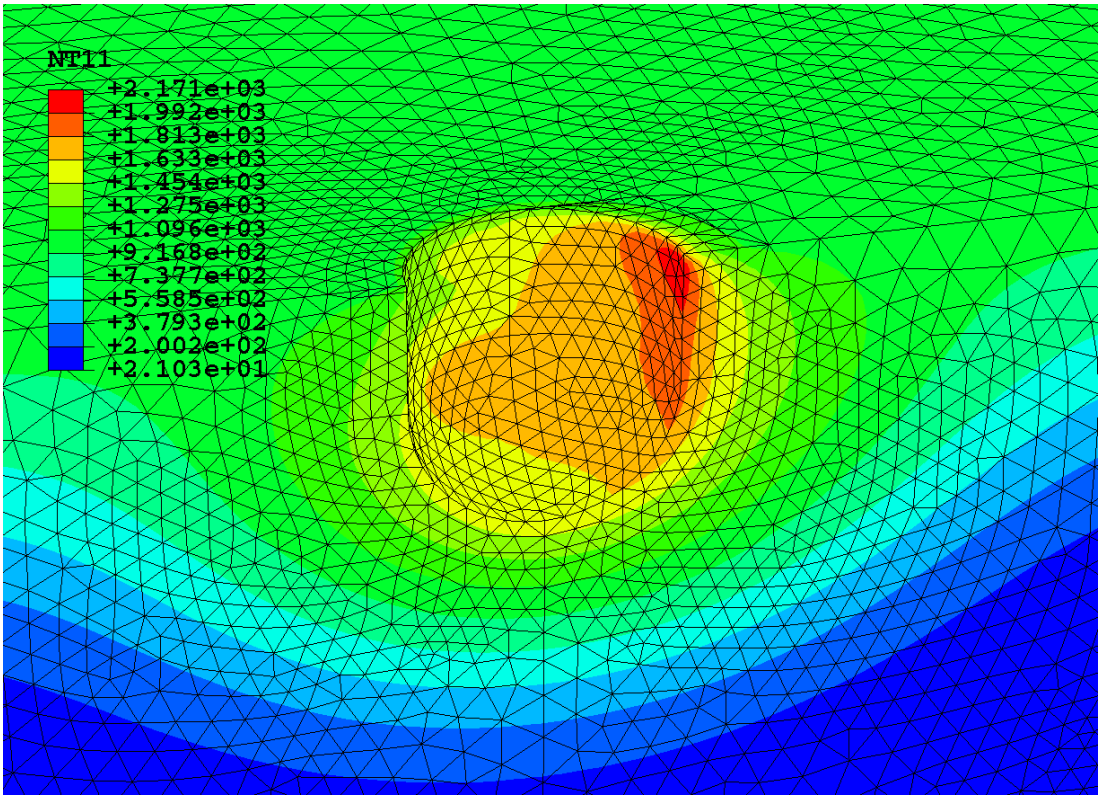

Figure 6.10: Temperature($^\circ$C) contour plot of $D = 1.0$ configuration subjected to EP heat load when maximum temperature is reached

CHAPTER VII

CONCLUSIONS AND RECOMMENDATIONS FOR FUTURE RESEARCH

Research on the response of damaged TPS had been very limited and the recent accident of the Space Shuttle *Columbia* emphasized the need for research in this important area. This study aims to fill in the gap by conducting experiments and FE analysis on a TPS used on the NASA Space Shuttle by examining the HRSI tiles used extensively on the underside of the space shuttle orbiter, where some of the severest aerodynamic heating occurs.

Preliminary FE analysis using an approximate axisymmetric model, subjected to several simplifying assumptions, was conducted on the TPS, which is modeled as a discrete three-layered structure, consisting of the tile, SIP and underlying structure. The TPS was subjected to the re-entry heat load and pressure of the ATS vehicle, and the temperature and thermal stress distribution was obtained. The preliminary results were compared to those obtained from a more accurate 3D model to determine the relative accuracy of the axisymmetric model. Further analysis was then conducted to determine the validity of the simplifying assumptions used in the preliminary analysis and improvements to the

models were made. The influence of damage location on the temperature distribution and thermal stresses results were also examined.

High-temperature experiments were conducted on damaged and undamaged HRSI tiles using quartz radiant lamps. The effects of damage on the thermomechanical behavior of the TPS under experimental conditions were determined. The limitations of the experimental setup do not allow realistic boundary conditions to be applied. However, the results obtained allow the validation of FE models developed.

The validated FE models was used to incorporate more realistic aerodynamic heat loads obtained from considering hypersonic flow past a cavity that models in an approximate manner, the interaction between external flow and the damage on the tile.

7.1 Conclusions

The principal conclusions obtained in the course of this research are summarized below:

1. For heat transfer FE analysis, the axisymmetric model can predict temperatures adequately, when compared to the more accurate 3D model. However, significant differences between thermal stress results exist that indicate the approximate results are not conservative. Thus, the axisymmetric model, which has significantly reduced computational requirements, could be useful for trend-type studies in preliminary design calculations where accuracy is less important than computational turn around time.

2. For the TPS considered, which consists of three very dissimilar materials operating under a wide range of temperature and pressure, the use of simplifying assumptions

can affect results in a complicated manner, and provides results that are not reliable. Thus, results should be based on realistic material properties and loading conditions.

3. Damage location was found to have very modest effects on temperature and thermal stress results.

4. High-temperature experiments on damaged TPS using radiant heaters have limited value, because the non-uniform and elevated temperatures that is expected to occur in the damaged regions due to cavity radiation cannot be replicated. Furthermore, TPS behavior under heat load/temperature profile that results from the complex interactions between flow and damage under realistic flight conditions cannot be studied in a thermal chamber. To obtain meaningful results, such tests have to be carried out in a hypersonic arc-jet tunnel.

5. Presence of damage in TPS changes the flow field and elevates the heat load on the TPS. The increase in heat load, coupled with the reduction in heat rejection capability of the TPS due to the removal of coating, and cavity radiation, can raise the temperatures within the tile to above its melting point. However, material failure due to thermal stresses alone is unlikely.

7.2 Recommendations for Future Research

This dissertation has examined the effects of damage on the transient temperature distributions and thermal stresses in a candidate TPS via experiments as well as FE studies. While this work has made substantial contributions to our understanding on the thermal protection capabilities and structural integrity of damaged TPS, a substantial amount of research still need to be done:

1. Consider damage progression associated with exceeding melting point of tile and determine the outcome of such an event.

2. Determine complete three-dimentional flow-dependent thermal loads to replace the approximate two-dimensional thermal loads used in FE analysis. These loads should incorporate real gas effects as well as chemistry.

3. Consider other structural failure mechanisms such as cracks formation and bond-line delamination.

4. Conduct experiments in arc-jet hypersonic tunnels, where interactions between flow and damaged TPS could be replicated.

5. Incorporate structural loading into experiments to determine interactions between thermal and mechanical loads.

6. Consider other forms of TPS, e.g. superalloy honeycomb and ARMOR TPS

APPENDIX

Appendix A

Determination of Actual Strains of Specimen in Experiments

For resistance strain gages, which were used in the experiments, strain measurements are obtained by measuring the change in gage resistance due to the elongation or contraction of the material to which they are attached. For experiments under constant temperature, the raw measurements are sufficient to determine the actual strains in the material. However, for the experiments with large changes in temperatures, as was the case in the experiments in this study, errors are introduced into the strain readings via two sources: 1) temperature dependence of gage factor (GF) and coefficient of resistivity (γ) of the strain gage material and 2) thermal expansion of of the strain gage itself. Thus, the raw or apparent strain reading from the gage is a function of the thermal expansion of the gage, the strain in the material to which it is attached, and the change in resistivity of the gage due to change in temperature. This is illustrated in Figure A.1.

Figure A.1(a) shows the original position of a strain gage attached to a specimen. In the final position shown in Figure A.1(b), the specimen is subjected to loads and a temperature change of ΔT, which result in a mechanical strain of $\varepsilon_{\text{S-Mech}}$ and a thermal strain of $\alpha_g\ \Delta T$. However, due to the thermal expansion and the change in γ and GF of the strain gage, the apparent strain registered is actually

$$\varepsilon_{\text{app}} = \varepsilon_{\text{s}} - \alpha_{\text{g}}\Delta T + \frac{\gamma}{\text{GF}}(\Delta T) \tag{A.1}$$

The last two terms, which is referred as the apparent strain error, can be quantified by

conducting free thermal expansion experiments on specimen of a material with known coefficient of thermal expansion (α_s). Since the specimen is allowed to expand freely, $\varepsilon_{\text{S-Mech}}$ = 0 and thus $\varepsilon_s = \alpha_g \Delta T$. With the apparent strain readings from the experiment and the calculated thermal strains in the specimen, the apparent strain error can be calculated from Equation A.1. Once the apparent strain error is quantified for the required range of temperatures, actual strains of the test specimen from subsequent experiments can be backed out from the apparent strain measurements, assuming that the strain gages from the same manufacturer's lot are used.

Figure A.2 shows the apparent strains obtained in experiments described in Chapter V for the undamaged specimen. The actual strains of the specimen after correcting the apparent strain errors is shown in Figure 5.9. Note the large differences between the apparent and actual strains.

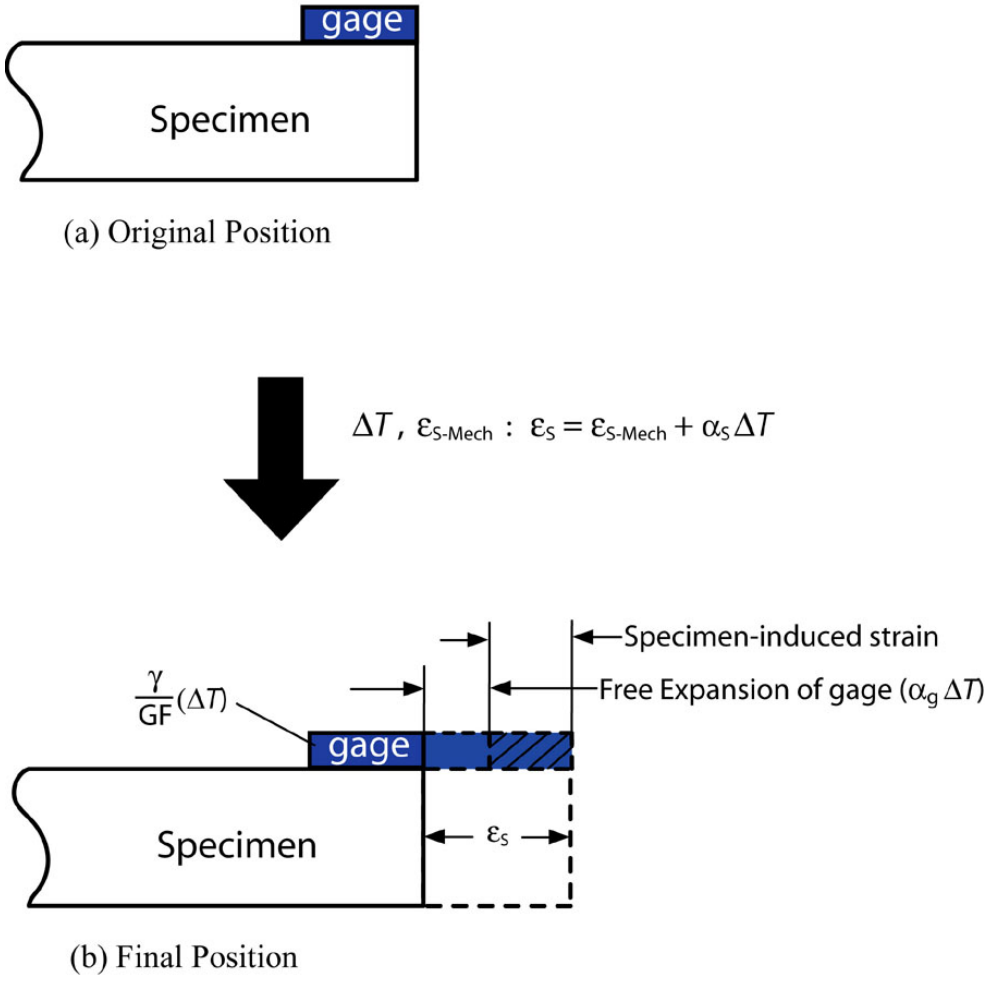

Figure A.1: Conceptual illustration of apparent strain

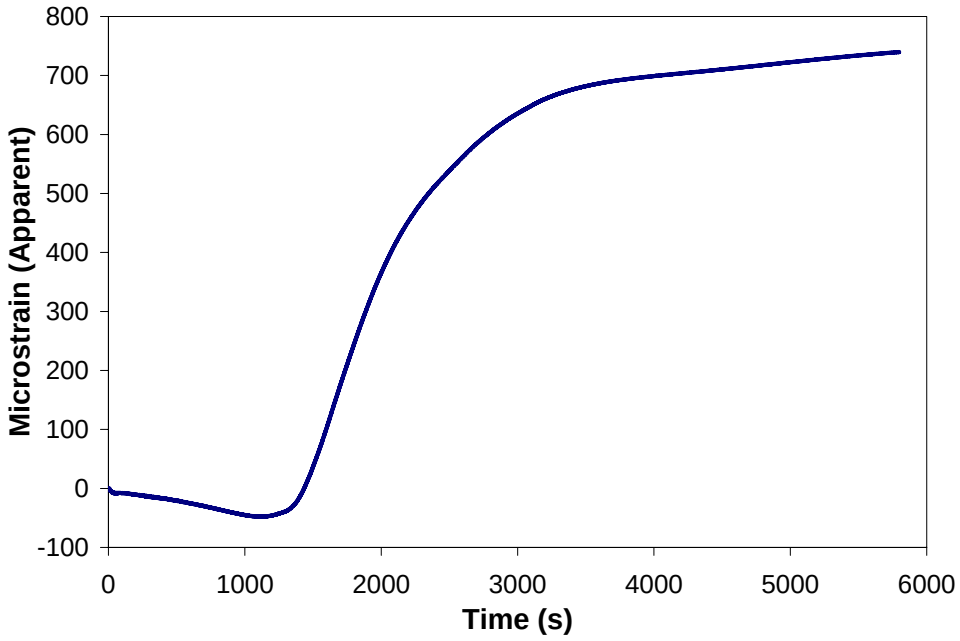

Figure A.2: Apparent strain results for undamaged specimen in experiments described in Chapter V

BIBLIOGRAPHY

BIBLIOGRAPHY

[1] *Report of the Columbia Accident Investigation Board, Vol. 1*, Government Printing Office, Washington, D.C., 2003.

[2] *Thermal Protection Systems Expert (TPSX) Material Properties Database V4*, NASA. [http://tpsx.arc.nasa.gov].

[3] J.R. Barber. *Elasticity*, Kluwer Academic Publishers, 2002.

[4] M.L. Blosser, R.R. Chen, I.H. Schmidt, J.T. Dorsey, C.C. Poteet, and R.K. Bird. "Advanced Metallic Thermal Protection System Development,". In *Proceedings of the AIAA 40th Aerospace Sciences Meeting & Exhibit*, Reno, NV, January 2002. AIAA Paper No. 2002-0504.

[5] W.D. Callister. *Materials Science and Engineering: An Introduction*, John Riley and Sons Inc., 2003.

[6] E.L. Christiansen and L.. Friesen. "Penetration Equations for Thermal Protection Material,". *International Journal Impact Engineering*, 20:153–164, 1997.

[7] P.A. Cooper, R. Miserentino, J.W. Sawyer, and J.D. Leatherwood. "Effect of Simulated Mission Loads on Orbiter Thermal Protection System Undensified Tiles,". *Journal of Spacecraft and Rockets*, 21(5):441–447, Sep-Oct 1984.

[8] K. Daryabeigi, M.L. Blosser, and K.E. Wurster. "Displacements of Metallic Thermal Protection System Panels During Reentry,". In *Proceedings of the 9th AIAA/ASME Joint Thermophysics and Heat Transfer Conference*, San Francisco, CA, June 2006. AIAA Paper No. 2006-2948.

[9] K. Daryabeigi, J.R. Knutson, and J.G. Sikora. "Thermal Vacuum Facility for Testing Thermal Protection Systems,". Techinical Memorandum 211734, NASA, 2002.

[10] R.L. Dotts, J.A. Smith, and D.J. Tillian. "Space Shuttle Orbiter Reusable Surface Insulation Flight Results,". *NASA Conference Publication 2283, Part 2*, pages 949–966, 1983.

[11] S. Evans and J. Williamsen. "Orbital Debris Shape and Orientation Effects on Impact Damage to Shuttle Tiles,". In *Proceedings of the 47th AIAA/ASME/ASCE/AHS/ASC Structures, Structural Dynamics and Materials Converence*, Newport, RI, May 2006. AIAA Paper No. 2006-2221.

[12] J.L. Everhart, S.J. Alter, N.R. Merski, W.A. Wood, and R.K. Prabhu. "Pressure Gradient Effects on Hypersonic Cavity Flow Heating,". In *Proceedings of the 44th AIAA Aerospace Sciences Meeting and Exhibit*, Reno, NV, January 2006. AIAA Paper No. 2006-185.

[13] E.P. Fahrenthold and Y.K. Park. "Simulation of Foam-Impact Effects on the Space Shuttle Thermal Protection System,". *Journal of Spacecraft and Rockets*, 42(2):201–207, Mar-Apr 2005.

[14] R.P. Hallion. *Supersonic Flight, The Story of the Bell X-1 and Douglas D-558*, Macmillan, New York, 1972.

[15] Hibbitt, Karlsson & Sorensen, Inc., Pawtucket, RI, *ABAQUS/Standard User's Manual Version 6.4*.

[16] R. Hill. "Advanced Metallic Thermal Protection System Development,". *Proceedings of the Royal Society of London, Series A, Mathematical and Physical Sciences*, 193(1033):281–297, May 1948.

[17] J.M. Housner, H.H. Edighoffer, and K.C. Park. "Nonlinear Dynamic Response of a Unidirectional Model for the Tile/Pad Shuttle Thermal Protection System,". Techinical Memorandum 81901, NASA, 1980.

[18] J.H. Kerr, D.J. Grousch, and E. Christiansen. "Impact Testing of Large Foam Projectiles,". In *Proceedings of the 42nd AIAA Aerospace Sciences Meeting and Exhibit*, Reno, NV, January 2004. AIAA Paper No. 2004-939.

[19] W.L. Ko and J.M. Jenkins. "Thermal Stress Analysis of Space Shuttle Orbiter Wing Skin Panel and Thermal Protection System,". Techinical Memorandum 88276, NASA, 1987.

[20] A. Komine and A.S. Kobayashi. "Interfacial Fracture of Space-shuttle Thermal-protection System,". *Experimental Mechanics*, 22(12):454–461, December 1981.

[21] D.A. Kontinos and G. Palmer. "Numerical Simulation of Metallic Thermal Protection System Panel Bowing,". *Journal of Spacecraft and Rockets*, 36(6):842–849, Nov-Dec 1999.

[22] S.L. Krist, R.T. Biedron, and C.L. Runsey, *CFL3D User's Manual Version 5.0*. NASA, Pawtucket, RI, 1997.

[23] J.D. Leatherwood and J.C. Gowdey. "Mission Load Dynamic Tests of Two Undensified Space Shuttle Thermal Protection System Tiles,". Techinical Memorandum 83148, NASA, 1981.

[24] F.S. Milos and T.S. Squire. "Thermostructural Analysis of X-34 Wing Leading-Edge Tile Thermal Protection System,". *Journal of Spacecraft and Rockets*, 36(2):189–198, Mar-Apr 1999.

[25] R. Miserentino, L.D. Pinson, and S.A. Leadbetter. "Some Space Shuttle Tile/Strain-Isolator Pad Sinusoidal Vibration Tests,". Techinical Memorandum 81853, NASA, 1980.

[26] H. Miura, M. Chargin, J. Bowles, T. Tam, D. Chu, and M. Chainyk. "Transient Analysis of Thermal Protection System for X-33 Vehicle using MSC/NASTRAN,". Document 20020054508, NASA, 1997.

[27] T.L. Moser and W.C. Schneider. "Strength Integrity of the Space Shuttle Orbiter Tiles,". In *Proceedings of the 1st Flight Testing Conference*, Las Vegas, NV, November 1981. AIAA Paper No. 81-2469.

[28] D.E. Myers, C.J. Martin, and M.L. Blosser. "Parametric Weight Comparison of Advanced Metallic, Ceramic Tile and Ceramic Blanket Thermal Protection Systems,". Technical Memorandum 210289, NASA, 2000.

[29] National Instruments, Austin, TX, *LabVIEW User Manual*.

[30] D.E. Nestler, A.R. Saydah, and W.L. Auxer. "Heat Transfer to Steps and Cavities in Hypersonic Turbulent Flow,". In *Proceedings of the AIAA Fluid and Plasma Dynamics Conference*, Los Angeles, CA, June 1968. AIAA Paper No. 68-673.

[31] W.E. Neuenschwander, D.U. McBride, and G.A. Armour. "Shuttle TPS Thermal Performance and Analysis Methodology,". *NASA Conference Publication 2283, Part 2*, pages 1025–1064, 1983.

[32] W.C. Pitts and M.S. Murback. "Flight Measurements of Tile Gap Heating on the Space Shuttle,". In *Proceedings of the AIAA/ASME 3rd Joint Thermophysics, Fluids, Plasma and Heat Transfer Conference*, St. Louis, MO, June 1982. AIAA Paper No. 82-0840.

[33] R. Prabhakaran and P.A. Cooper. "Photoelastic Tests on Models of Thermal Protection System for the Space Shuttle Orbiter,". Techinical Memorandum 81866, NASA, 1980.

[34] M.V. Pulsonetti and W. Wood. "Computational Aerothermodynamic Assessment of Space Shuttle Orbiter Tile Damage - Open Cavities,". In *Proceedings of the 38th AIAA Thermophysics Conference*, Toronto, Ontario, Canada, January 2005. AIAA Paper No. 2005-4679.

[35] J.F. Rakow. *Thermomechanical Response of Metal Foam Sandwich Panels for Structural Thermal Protection Systems in Hypersonic Vehicles*. PhD Dissertation, University of Michigan, Ann Arbor, 2005.

[36] R.C. Reid, W.D. Goodrich, C.P. Li, C.D. Scott, S.M. Derry, and R.J. Maraja. "Space Shuttle Orbiter Entry Heating and TPS Response: STS-1 Predictions and Flight Data,". *NASA Conference Publication 2216*, pages 327–347, 1982.

[37] Hallion R.P. "The Path to the Space Shuttle: The Evolution of Lifting Reentry Technology,". *Journal of British Interplanetary Society*, 36(12):523–541, 1983.

[38] J.W. Sawyer. "Effect of Load Eccentricity and Substructure Deformations on Ultimate Strength of Shuttle Orbiter Thermal Protection System,". Techinical Memorandum 83182, NASA, 1981.

[39] J.W. Sawyer. "Effect of Strain Isolator Pad Modulus on Inplane Strain in Shuttle Orbiter Thermal Protection System Tiles,". Techinical Paper 2141, NASA, 1983.

[40] J.W. Sawyer. "Mechanical Properties of the Shuttle Orbiter Thermal Protection System Strain Isolator Pad,". *Journal of Spacecraft and Rockets*, 21(3):253–260, May-Jun 1984.

[41] J.W. Sawyer and P.A. Coooper. "Fatigue Properties of Shuttle Thermal Protection System,". Techinical Memorandum 81899, NASA, 1980.

[42] S.J. Scotti, C. Clay, and M. Rezin. "Structures and Materials Technologies for Extreme Environments Applied to Reusuable Launch Vehicles,". In *Proceedings of the AIAA/ICAS International Symposium and Exposition*, Dayton, OH, July 2003. AIAA Paper No. 2003-2697.

[43] J.L. Shideler, H.N. Kelly, D.E. Avery, M.L. Blosser, and H.M. Adelman. "Multiwall TPS An Emerging Concept,". *Journal of Spacecraft and Rockets*, 19(4):358–365, Jul-Aug 1982.

[44] J.L. Shideler, G.L. Webb, and C.M. Pittman. "Verification Tests of Durable Thermal Protection System Concepts,". *Journal of Spacecraft and Rockets*, 22(6):598–604, Nov-Dec 1985.

[45] S. Soltani and Hillier R. "An Experimental and Computational Study of Hypersonic Flows,". In *Proceedings of the AIAA Aerospace Sciences Meeting and Exhibit*, Reno, NV, January 1994. AIAA Paper No. 94-0766.

[46] R.F. Stellingwerf, J.H. Robinson, S. Richardson, S.W. Evans, R. Stallworth, and M. Hovater. "Foam-on-Tile Impact Modeling for the STS-107 Investigation,". In *Proceedings of the 42nd AIAA Aerospace Sciences Meeting and Exhibit*, Reno, NV, January 2004. AIAA Paper No. 2004-938.

[47] K.K. Tamma and E.A. Thornton. "Re-Entry Thermal/Structural Finite-Element Modeling/Analysis of Shuttle Wing Configurations,". *Journal of Spacecraft and Rockets*, 24(2):101–108, Mar-Apr 1987.

[48] E.A. Thornton. *Thermal Structures for Aerospace Applications*, AIAA, 1996.

[49] P. Tong and T.H.H. Pian. "On Convergence of the Finite Element Methods for Problems with Singularity,". *International Journal of Solids and Structures*, 9:313–321, 1973.

[50] S.S. Wang and F.K. Yuan. "A Singular Hybrid Finite Element Analysis of Boundary-Layer Stresses in Composite Laminates,". *International Journal of Solids and Structures*, 19(9):825–837, 1985.